University of Alberta

Bi-metallic Catalyst for Hydrogen Sorption of Magnesium Hydride

by

Beniamin Zahiri-Sabzevar

A thesis submitted to the Faculty of Graduate Studies and Research
in partial fulfillment of the requirements for the degree of

Doctor of Philosophy
in
Materials Engineering

Department of Chemical and Materials Engineering

Fall 2012
Edmonton, Alberta

Dedication

To my Mom, Dad, my sister Maryam and my brother Ramin,

And to my lovely wife, Marjan.

Abstract

This thesis is focused on the design of a series of bi-metallic catalyst for enhancing the hydrogen sorption kinetics of magnesium hydride. We have utilized thin films deposited by magnetron sputtering technique as model systems to study various alloys and compositions. It has been known that the transition metals additions can catalyze the sorption reaction. We hypothesized that the addition of bi-metallic catalysts has superior effect over the single metal additions. In order to obtain baselines, we have examined the effect of single transition elements on the kinetics of the transformation. In our first attempt, we showed that the sorption behavior of the ternary Mg-Fe-Ti alloy is significantly improved compared to its binary alloy counterparts. Using this ternary system, we were able to perform absorption/desorption tests up to 100 cycles at a low temperature of 200˚C. We further investigated the validity of our hypothesis by performing the similar cycling measurements on two more ternary systems, being Mg-Fe-V and Mg-Cr-Ti. We showed that both systems exhibit remarkably enhanced sorption characteristics over the binary alloys.

In our last attempt, we examined the effect of Cr-V bi-metallic catalyst on the hydrogen sorption behavior of MgH_2. The catalyst was so potent that we were able to absorb the activated samples at room temperature and a low hydrogen pressure of 2 bar. We also performed cycling tests on this systems at 300˚C with the desorption pressure of 1 bar. In order to explore the microstructural origins of such performance, we utilized transmission electron microscopy (TEM) and X-ray diffraction techniques. Through a systematic grain size measurement, we found that the MgH_2 in ternary systems is more resistant to grain coarsening compared to binary alloys. The cryo-stage TEM analysis of

the partially absorbed sample shed light on the transformation mechanism of Mg to MgH_2. It revealed the absence of a core-shell structure which is mostly assumed as the absorption mechanism for MgH_2. The cryo-stage TEM results also showed the presence of twins in the hydride microstructure which is most likely due to the fast rate of the absorption transformation. We also performed a detailed kinetics analysis in the framework of Johnson-Mehl-Avrami (JMA) model. We found that the activation energy value has a strong dependency on the driving force for the reaction. Using the value of activation energy and the calculated Avrami exponent, the possible rate limiting step for the absorption and desorption reactions was proposed. By combining the microstructural observations and the kinetics analysis we proposed a mechanism for the Mg to MgH_2 transformation.

Acknowledgments

It would not have been possible to accomplish this thesis without the help and support of many people. First and foremost I offer my utmost gratitude to my supervisor, David Mitlin, who has supported me throughout this research with his knowledge and patience, and also for giving me the freedom and resources I required. I am also indebted to every member of Mitlin Group for their invaluable and unconditional help; Thank you Chris Harrower, Babak Shalchi-Amirkhiz, Mohsen Danaie, Julian Haagsma, Peter Kalisvaart, Colin Ophus, Erik Luber, Brian Olsen, Chris Holt and Ramin Zahiri. In particular I would like to thank XueHai Tan with whom I spend hours on discussion on various research ideas that helped me through my PhD thesis. My acknowledgment also goes to all the technicians and staff members of the Chemical and Materials Engineering Department, National Institute for Nanotechnology and Cross-Cancer Institute at University of Alberta.

I also thank to all my other fiends for their unequivocal supports. Lastly, I would like to thank my family for their endless and understanding love through all years of my studies.

Contents

List of Figures

List of Tables

1 Introduction

1.1 Hydrogen and Hydrogen Economy

The limited natural resources of hydrocarbon fuels in combination with their harmful influence on global environment have made researchers seek for a renewable, environmentally friendly and safe energy carrier alternative. Hydrogen has been the best alternative since it is a pollution-free and abundant energy carrier with an efficient energy conversion.

Hydrogen can be produced from various resources of both renewable (wind, solar, biomass) and non-renewable (fossil fuels) types. A large quantity of today's hydrogen is produced by steam reforming of methane. Although this method is accompanied by the CO_2 by-product, the emission is still lower than that of burning the same amount of methane [1]. The emission of carbon dioxide is considered as the main cause of the global climate change [1,2]. Other alternative methods of hydrogen production are involved with splitting of water. This process can be done through various approaches such as electrolysis, photo catalysis, high-temperature decomposition and photo-biological splitting. However, none of these methods are commercially efficient when compared with the production of hydrogen from fossil fuels [1,3]. Recent studies showed that the use of solar energy is most likely the only viable method toward mass production of hydrogen in the hydrogen-based economy [4].

Within the framework of hydrogen economy, hydrogen can be considered as an energy career rather than a primary energy source (such as oil, gas, coal). As mentioned

above, it can be produced from another energy source and then transported and stored for its future use. Hydrogen can be utilised as a fuel in power generating systems such as fuel cells. Fuel cells as the main constituents of the hydrogen-based economy can convert hydrogen and hydrogen-rich fuels to electricity with low carbon dioxide emission.

Apart from the hydrogen production step, storing the hydrogen is one of the critical technological barriers toward hydrogen-based economy. For a system to be hydrogen storage medium, there are some critical requirements to be met. Depending on the nature of the application, different criteria must be satisfied. For example, for mobile application, lower total weight and volume are more important than those of stationary application. In general, high capacity of storage, moderate temperatures and reversibility of hydrogen uptake and release, moderate operating pressures as low as atmospheric pressure and low storage cost are needed for a suitable storage system.

1.2 Hydrogen storage

Hydrogen storage methods can be categorized into two groups: Compressed gas and cryogenic liquid storage and materials-based hydrogen storage [5]. The two currently options for the first category are high-pressure (500 and 700 bar) vessels and cryogenically liquefied hydrogen. The former requires up to 20% of the hydrogen energy content to compress the gas while the latter requires up to 40% to liquefy it [1]. Achieving a reasonable gravimetric density with this pressurised vessel is still costly being generally an order of magnitude more expensive than an equivalent gasoline tank [6]. Another deficiency of compressed and liquid hydrogen tanks is their low volumetric density which is a major barrier toward transportation application. Even with the use of recently

developed cryo-compressed (276 bar) tanks with high gravimetric and volumetric densities, the cost is still debatable [7].

On the other side, in materials-based methods, storage mechanisms lie on three main groups: adsorption, absorption and chemical reaction. Adsorption includes the two main processes of physisoprtion and chemisorption and usually involves the use of carbon-based materials. Absorption occurs though the incorporation of hydrogen atoms into interstitial sites of a crystal lattice. This category is best known as the hydrogen storage in metal hydride. The last mechanism involves a chemical reaction for hydrogen storage and generation [5]. The main focus of the current research lies in the second category, i.e. metal hydrides. Metal hydride possess higher volumetric density (110 kg H_2 m^{-3} for MgH_2) than hydrogen gas (<40 kg H_2 m^{-3}) or liquid hydrogen (71 kg H_2 m^{-3}). However the properties of the current known metal hydrides are still far from the on-board application criteria set by US department of energy (DOE). The main reasons for this are the excess heat produced during the refilling process and low capacities in terms of system rather than material [7]. On the other hand, the use of metal hydrides for stationary and even portable application is still the subject of many researches.

1.3 Metal hydrides

Hydrogen interacts with most of metals, solid solution alloys, amorphous metal alloys and intermetallic compounds. Hydrogen molecules dissociate at the surface of host metal and hydrogen atoms diffuse through the crystal lattice. These dissociated hydrogen atoms occupy interstitial sites of the lattice to form either a solid solution or a distinct metal hydride phase. The process of hydride formation occurs according to one of the below equations depending on the environment of the reaction:

$$M\ (s) + x/2H_2\ (g) \rightarrow MH_x\ (s) \quad (1\text{-}1)$$

$$M\ (s) + xH_2O(l) + e^- \rightarrow MHx\ (s) + OH^-\ (l) \quad (1\text{-}2)$$

Both reactions could be reversible depending on the temperature and pressure variations [8]. Based on the nature of the bonding between hydrogen and metal atoms, the hydrides can be categorized into three groups: Ionic or saline hydrides which is the case when alkali or alkaline earth atoms form bonds with hydrogen. Some examples from this group are MgH_2, NaH or CaH_2. Stable hydrides of this group can be desorbed at elevated temperatures. This means that reaction (1-1) is reversible only at high temperatures. Generally the metal/hydride sorption reaction has poor kinetics properties in this group. Second group is the covalent hydrides which form between non-metallic atoms such as S, Si, B or B and hydrogen. The third group is the metallic hydrides. Metallic bonds between transition or rare earth metals and hydrogen result in formation of these type of hydrides [8,9].

There are also some hydrides of intermetallic compounds (IMCs) in a common form of $A_mB_nH_x$. These hydrides can also be counted as metallic hydrides. These IMCs contain two or more metals that at least one of them possesses high bonding affinity towards hydrogen. There are some well-known groups of these compounds based on the ratio of A to B atoms. A summary of most important intermetallic compounds along with their structure, their hydrides and storage properties has been listed in Table 1.1 [8]. Generally, A is an elements tending to form stable hydride like rare earth or alkaline earth metal and B usually does not form a stable hydride at ambient condition such as some of the transition metals [1,9]. Intermetallic hydrides have shown promising sorption properties in terms of kinetics and thermodynamics [10-12].

Table 1.1: Important hydride forming metals and intermetallic (adapted from [10]).

Family	Model system	Crystal structure type	Hydride/Deuteride	Negative storage properties
A	Mg	Mg, hP2	MgH_2	Stable hydride, mod. kinetics
AB_5	$LaNi_5$	$CaCu_5$, $D2_d$ (hP6)	$LaNi_5H_{6.5}$	Heavy, expensive
AB_2	$ZrMn_2$, $TiMn_2$	$MgZn_2$, C14 (hP12) Laves phase	$ZrMn_2D_3$, $TiMn_2D_3$	Stable hydride, mod. kinetics
	$ZrCr_2$, ZrV_2	$MgCu_2$, C15 (cF24) Laves phase	$ZrCr_2H_{3.8}$, $ZrV_2H_{4.9}$	Stable hydride, mod. kinetics
AB	TiFe	CsCl, B2 (cP2)	TiFeH, $TiFeH_{1.9}$	Difficult activation
A_2B	Mg_2Ni	Mg_2Ni, C_4 (hP18)	Mg_2NiH_4	Stable hydride, mod. kinetics
	Ti_2Ni	Ti_2Ni, (cF96)	Ti_2NiH	Stable hydride
A_2B-AB	Ti_2Ni-TiNi	Multiphase alloy, (cF96 and mP4)	Ti_2NiH-TiNiH	Stable hydride

1.3.1 Thermodynamics of metal-hydrogen reaction

The thermodynamics of the formation of a metal hydride is generally described by the pressure-composition-temperature (PCT) (Figure 1.1). The isotherm plots can be divided into three regions. The first region in Fig. 1.1 is corresponding to the low concentration of hydrogen (x<<1 in Eq. 1-1).

In this range on concentration hydrogen is dissolved in the metal lattice and forms a solid solution phase known as α-phase with similar crystal structure of the metal. From the thermodynamics point of view, the chemical potential of the gaseous hydrogen and dissolved hydrogen are in the equilibrium state at this stage:

$$\frac{1}{2}\,\mu_{H_2}(\mathrm{P},\mathrm{T}) = \mu_H\,(\mathrm{P},\mathrm{T},\mathrm{x}) \qquad 1\text{-}3$$

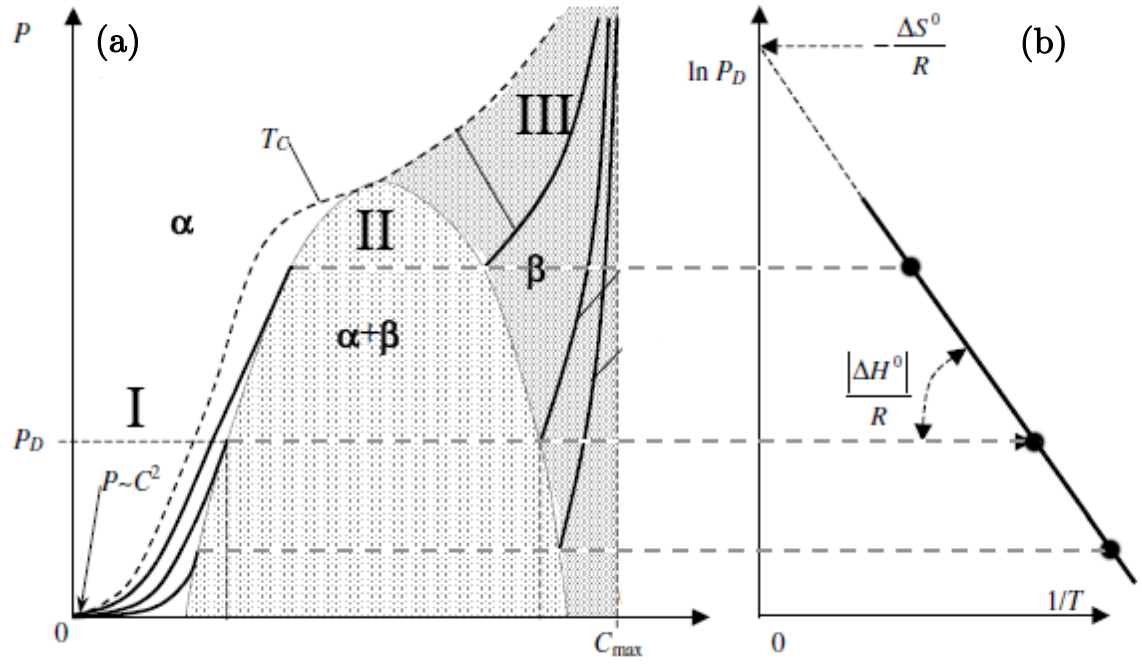

Figure 1.1: Schematic of PCT digram for metal-hydrogen system, with α as the solid solution of hydrogen in metal and β as the hdyride. (b) van't Hoff plot for calculation the enthalpy of hydride formation. (adapted from [8]).

where μ_{H2} and μ_H are the chemical potentials of the molecular hydrogen and the atomic hydrogen in the α-phase. Hydrogen can be treated as an ideal gas at pressure below 100 bar. Hence we can write the flowing:

$$\mu_{H_2}(\mathrm{P,T}) = H^0_{H_2} - TS^0_{H_2} + RTlnP_{H_2} \qquad 1\text{-}4$$

Here H^0_{H2} and S^0_{H2} are the standard enthalpy and entropy of hydrogen gas. The following equation can also be written for the chemical potential of the atomic hydrogen in the α-phase:

$$\mu_H(\mathrm{P,T,x}) = H_H - TS_H^{nc} + RTln(\frac{x}{r-x}) \quad \text{1-5}$$

where H_H and S^{nc}_H are the enthalpy and non-configurational entropy of the atomic hydrogen in the solid solution phase. The last term in Eq. 1-5 denotes the configurational entropy term. The number of interstitial sire per metal atoms is also denotes as r. We can also assume that x<<r this region. Having known this fact, inserting the equations 2-4 and 2-5 in equation 2-3 results in the following:

$$x = K.P_{H_2}^{1/2} \quad \text{1-6}$$

where

$$K = \exp(\frac{\Delta H_s - T\Delta S_s + RTlnr}{RT}) \quad \text{1-7}$$

and the ΔH_s and ΔS_s are the enthalpy and entropy of the solution and defined as $\Delta H_s = H_H - 1/2H^0_{H2}$ and $\Delta S_s = S^{nc}_H - 1/2S^0_{H2}$. Equation 2-6 is best known by Sievert's law and K is the Sivert's constant.

As hydrogen pressure increases, the hydrogen concentration increases up to the solubility limit of the solid solution and the hydride phase (β) nucleates. The new formed phase has a different crystal structure form the parent metal phase. At this stage, two phases exist together and isotherms show a flat line in pressure, so called plateau pressure, with a length proportional to the reversible hydrogen capacity of the metal. The transition of α→β takes place at this equilibrium pressure. The dependence of this pressure on temperature is described by the well-known Van't Hoff equation:

$$\ln\left(\frac{P_{eq}}{P_0}\right) = -\frac{\Delta H_{\alpha\to\beta}}{RT} + \frac{\Delta S_{\alpha\to\beta}}{R} \qquad 1\text{-}8$$

In the pure β-phase region (region III in Figure 1.1), hydrogen enters in the β-phase solid solution and concentration increases with the pressure. The two-phase region disappears at the critical point and the transition becomes continuous. The entropy change in Van't Hoff equation usually refers to the entropy variation when hydrogen molecule enters into the metal lattice. So, one can assume that it is independent of the metal and hydride phases. In all metal-hydrogen systems, a ΔS values of 130 J/K.mole H_2 is applicable for calculating plateau pressure or equilibrium temperatures [11 ,12]. In the real cases, PCT curves are different from what is shown in Fig. 1.1. The plateau region is sloped in most of hydride systems. The absence of a true equilibrium during the experimental conditions could usually cause such slope. Apart from the experimental conditions, the presence of inhomogeneities in the metal lattice is usually reported as the main cause for the plateau sloping [10]. Another feature observed in the real PCT curves is the appearance of a hysteresis effect which basically means that the absorption plateau is higher than the desorption plateau. Generally, hysteresis is attributed to the occurrence of an asymmetry between the transformation strains involved in hydride formation and decomposition [9,13,14]. This is the difference between the ability to accommodate the strain in the metallic and hydride phases.

1.3.2 Kinetics of metal-hydrogen reaction

The reaction between hydrogen and metal is usually considered as a heterogeneous solid-gas reaction in the literature [15]. Such a reaction consists of several elementary

steps though which the hydrogen gas molecules transform to a bound hydrogen atoms in lattice of the solid material. The reaction is generally divided into the following five major steps: physisorption (adsorption), chemisorption, surface migration, diffusion and hydride nucleation and growth [15,16,17]. The slowest step form the above mentioned steps controls the overall rate of the reaction. The main objective of kinetics analysis is to identify this step, also known as the rate limiting step. It is worth mentioning that a single rate limiting step does not necessarily exist. This is due the interdependence of different steps in some cases [18]. One also should not expect a similar rate limiting step for absorption and desorption reactions. The parameter that is generally used in the kinetics analysis is the amount of transformed phase which is formulated versus time. Each step possesses its own characteristics kinetics curve which is expressed in terms of this parameter. Hence, if a good fit for the experimental data and the analytical model is obtained, the rate limiting step can be deduced. The possible way to speed up the reaction kinetics then can be applied.

The process through which the hydrogen molecules approach the metal surface and the subsequent steps can be easily described by the one dimensional potential energy curve shown in Figure 1.2. As it can be seen in this plot, far from the metal surface there is a potential energy difference of 218 kJ/mole.H between hydrogen molecule and two hydrogen atoms ($H_2 \rightarrow 2H$, E_{diss}=218 kJ/mole.H). The first interaction between hydrogen molecules approaching the metal surface is called physisorption. Such interaction is in the form of van der Waals forces within the range of 3.5-10 kJ/mole at the distance of z_p from the metal surface. The distance is approximately one hydrogen molecule radius (˜0.2nm) form the surface [19].

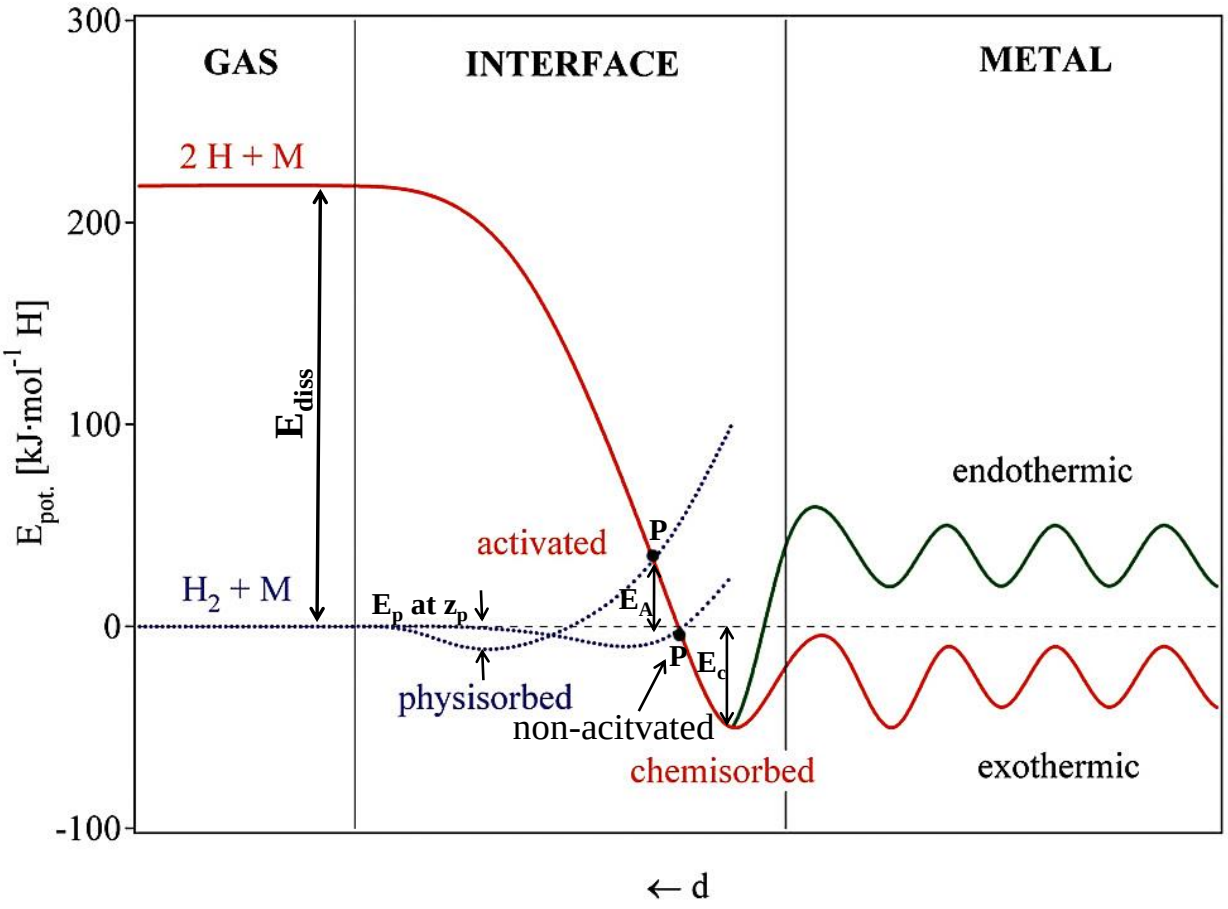

Figure 1.2: Schematics for the potential energy curves of the activated or non-activated dissociation and chemisorption of hydrogen on metal surface and the following endothermic or exothermic solution of atomic hydrogen into the bulk (adapted from [19] and [20]).

When hydrogen molecule is dissociated prior to the interaction, a different pathway can be observed. This is also shown as a superimposed curve in Fig. 1.2. Here, the potential energy curve starts with higher values of 218 kJ/mole.H above the zero level.

The hydrogen atoms show strong attractive forces towards the metals atoms which cause the potential curve to reach lower values as they are brought to the surface. The depth of the potential well is within the range of 500-600 kJ/mole which basically represents the bonding energy of single hydrogen atom and metal atom. This value is gained twice since a hydrogen molecule dissociates into two hydrogen atoms. As the superposition of the physisorptive and the atomic hydrogen interaction potential energy shows, a cross over point P can occur. The location of this point may either lie above or below the energy zero level. In the situation where P is below the E=0, the chemisorption reaction occurs without the need for any additional energy. A small amount of energy, E_{ad} or the heat of chemisorption (E_c) is released at this stage that can be experimentally measured. Examples of metal surfaces which show such non-activated hydrogen adsorption are Ni, Pd or Pt surfaces [20]. The bonding energy of the hydrogen-metal surface can then be determined through the following equation:

$$E_{M\text{-}H} = 1/2(E_{diss} + E_{ad}) \qquad 1\text{-}9$$

The calculated values of H-M biding energy from numerous systems show a similar value of 250 kJ/mole (2.6 ev) despite the presence of large difference in the adsorption energies. This proposes the similarity of binding mechanism between hydrogen and many metals [20]. The chemisorbed hydrogen atom can then jump to the subsurface layer and finally diffuse through the metal lattice in an endothermic or exothermic pathway [19].

As Fig. 1.2 shows, a different situation occurs when the point P is above the energy zero level. In this case, an extra amount of energy known as activation energy E_A is required in order to dissociate hydrogen molecules. This case is usually called activated adsorption. The hydrogen dissociation /recombination is fairly slow and could the rate limiting step of the reaction.

The above mentioned steps correspond to the interactions between hydrogen and the metal surface. However, most of real cases are encountered by some other factors that make the analysis more complicated. The presence of a native oxide layer, surface contamination and a multiphase surface layer are among these factors. The additions of a catalyst phase may also transfer the rate limiting step toward the later stages of the hydride formation/decomposition reaction. As mentioned above, the main parameter employed in most of kinetics analysis is the reacted fraction f which is expressed as a function of time, t. The first step in the kinetics analysis is to find the function that best describes the reacted fraction versus time. The next step concerns with identifying the pressure dependence of the reaction rate. Such dependence is usually described by a function so-called the driving force function. To find the temperature dependence of the reaction rate thought an Arrhenius plot and obtaining the activation energy is the last step of thorough kinetics analysis.

Several models have been developed to describe the kinetics of the hydrogen-metal reaction. These models are developed based on the assumption of a certain rate limiting step being hydrogen dissociation/recombination (chemisorption) or the nucleation and growth of the product phase. Barkhordarian et al. [17] categorized the models for describing the sorption reaction into three groups: surface reaction, Johnson-Mehl-Avrami (JMA) model and the contracting volume (CV) model.

The main assumption in the surface reaction model is that the rate limiting step is the chemisorption process. The reacted fraction has a linear dependence on time in this model as shown in the following equation:

$$f = kt \qquad \text{1-10}$$

where k is the rate constant of the reaction and t is time. In general, the reaction of hydride formation and decomposition involve a transformation from α to β phase that occurs though a nucleation and growth (NG) process. A detailed review by Mintz and Zeiri [21] reported the models based on this process for hydrogen storage materials. The most two applicable models based on a nucleation and growth process are CV and JMA. In the CV model the assumption is that the nucleation of the hydride phase starts at the surface and the consequent growth occurs into the bulk. The initial nucleation rate is usually fast compared to the overall growth rate and the surface layer is thin compared to the particle diameter. This model is expressed as follows:

$$f = 1-(1-kt)^n \qquad 1\text{-}11$$

where f is the reacted fraction, k is the rate constant, t is time and n is a constant related to the dimensionality of the growth being n=2 for two dimensional and n=3 for three dimensional growth.

JMA model assumes the nucleation and growth occurs randomly in the bulk and at the surface. It also assumes that the sample volume is infinite and takes the impingement of growing grains into account. It has been shown that homogeneous and heterogeneous nucleation conditions could be well described by JMA model [22]. This model is also applied to transformations in which the growth rate is diffusion limited and interface controlled. This model is also valid in the cases of nucleation site saturation and constant nucleation rate with constant growth rates. The equation used in JMA model is as follows:

$$f = 1-\exp[-(kt)^n] \qquad 1\text{-}12$$

where k is the rate constant and n is a constant so-called Avrami exponent. The Avrami exponent is related to the dimensionality of the growth process and gives information

about the rate-limiting step of the reaction. The Avrami exponent n can be expressed in the general form of $d/m + a$. Here d is the dimensionality of the growth ($d = 1$, 2 and 3) and m indicates interface-controlled ($m = 1$) or diffusion-limited ($m = 2$) growth. The constant a is related to nucleation rate where $a = 0$ for site saturation (constant number of nuclei), $0 < a < 1$ for decreasing nucleation rate, $a = 1$ for constant nucleation rate and a > 1 for increasing nucleation rate. Christian [22] in his classis textbook reported a detailed correlation between different Avrami exponents and nucleation and growth states as can be seen in Table 2.2. As can be seen in this table, the information from the Avrami exponent is not conclusive especially when n values are small, i.e. n <1.5. For example, n = 1 describes both a diffusion-limited reaction where particles grow along 1-D defects and also an interface controlled growth with grain boundary nucleation after saturation. Therefore, identifying the driving force function and the activation energy along with direct observation from various stages of the reaction are essential to determine the proper rate limiting step.

Generally, the rate constant k is a function of temperature and pressure. Thus, it can be written in the following form [23].

$$k = k(P).k(T) = k(P).k_0 \exp(-Q/RT) \qquad 1\text{-}13$$

where $k(P)$ is the pressure-dependent term. This term is also referred to as the driving force function. In the pressure-independent term $k(T)$, k_0 is the pre-exponential factor, Q is the overall activation energy and R is the gas constant. Therefore, to obtain the activation energy of the reaction, one should account for the influence of the pressure during the measurements. The selection of the driving force function is mostly depending

on the rate-limiting step of the reaction. For the metal/hydride transformation, a thermodynamic driving force can be used [36].

Table 1.2: The correlation between the Avrami exponent, n and the nucleation and growth modes (adapted from [22]).

(a) Polymorphic changes, discontinuous precipitation, eutectoid reactions, interface controlled growth, etc.	
Condition	n
Increasing nucleation rate	>4
Constant nucleation rate	4
Decreasing nucleation rate	3-4
Zero nucleation rate (saturation of point sites)	3
Grain edge nucleation after saturation	2
Grain boundary nucleation after saturation	1
(b) Diffusion controlled growth	
Condition	n
All shapes growing from small dimensions, increasing nucleation rate	>2.5
All shapes growing from small dimensions, constant nucleation rate	2.5
All shapes growing from small dimensions, decreasing nucleation rate	1.5-2.5
All shapes growing from small dimensions, zero nucleation rate	1.5
Growth of particles of appreciable initial volume	1-1.5
Needles and plates of finite long dimensions, small in comparison with their separation	1
Thickening of long cylinders (needles) (e.g. after complete end impingement)	1
Thickening of very large plates (e.g. after complete edge impingement)	0.5
Precipitation on dislocations (very early stages)	~0.67

This function is obtained directly from the chemical potential for a reaction at non-standard conditions ($\mu = \mu_0 + RT\ln Q$, where Q is the reaction quotient). At a constant temperature, this function has the following form for the case of absorption:

$$k(P) = \ln(P/P_{eq}) \quad \text{1-14}$$

where, P_{eq} is the equilibrium hydrogen partial pressure for a given temperature.

Rudman showed that in a process where the diffusion is the rate-limiting step, another type of driving force expression could be employed [24]. In the derivation the thermodynamic terms and the diffusivity of the hydrogen atoms were taken into account. The following equation was introduced for the driving force of a diffusion-limited absorption reaction:

$$k(P) = 1 - (P_{eq}/P)^{0.5} \quad \text{1-15}$$

In order to obtain the proper diving force expression, a systematic analysis of a range of rate constant values at different pressures and constant temperature is required. Once the equation that best fits the relationship between the rate constant and pressure is found, the activation energy measurements can be performed at a constant driving force and various temperatures.

1.4 Mg and its alloys as hydrogen storage materials

MgH_2 contains 7.6wt% hydrogen which is the highest capacity amongst all the reversible metal hydrides. High capacity of hydrogen storage along with the low cost of pure magnesium makes magnesium as an excellent choice for hydrogen storage applications. However, there are some disadvantages related to this hydride which restrict its use in practical applications. These problems can be described in terms of kinetics and thermodynamics. The following sections provide a detailed report on the recent progress toward improving the sorption behavior of magnesium.

1.4.1 Thermodynamics of hydrogenation

High thermodynamic stability of magnesium hydride is an important factor which hinders its application in practice. Magnesium hydride has a low enthalpy of formation of -74 kJ/mole H_2 which results in the equilibrium pressures in the order of 10^{-7} bar at room temperature [25]. A minimum operating pressure of 1 bar is usually required for practical applications which means the operating temperature of about 300˚C for a Mg-based alloy. Another issue arising from such high thermodynamics stability is related to thermal management. As the reaction proceeds, the problem with the conductivity of the hydride phase and also the heat transfer must be managed properly [26]. In order to lower the operating temperature of MgH_2, the enthalpy and entropy of hydride formation/decomposition must be altered. In other words, the hydride should be destabilized. The research on destabilization of MgH_2 generally focuses on two approaches, being alloying and nanostructuring.

Addition of an alloying element that interacts with magnesium and creates an intermediate state can reduce the heat of formation (the absolute value). This approach has been pursued for few decades. In general, alloying can affect the thermodynamics in two distinct ways. As Figure 1.3 demonstrates, the alloying element could form an intermetallic compound with Mg which is stable after dehydrogenation. In this case, the intermetallic phase disproportionates to form the MgH_2 and upon the dehydrogenation, Mg does not return to its original crystal structure. The ΔH_1 of this reaction is different from that of the MgH_2. The first attempt of such reaction was reported by Reilly and Wiswall on the magnesium-copper alloy [27]. Magnesium forms the Mg_2Cu upon alloying and the reaction of hydrogen with this intermetallic is as follows:

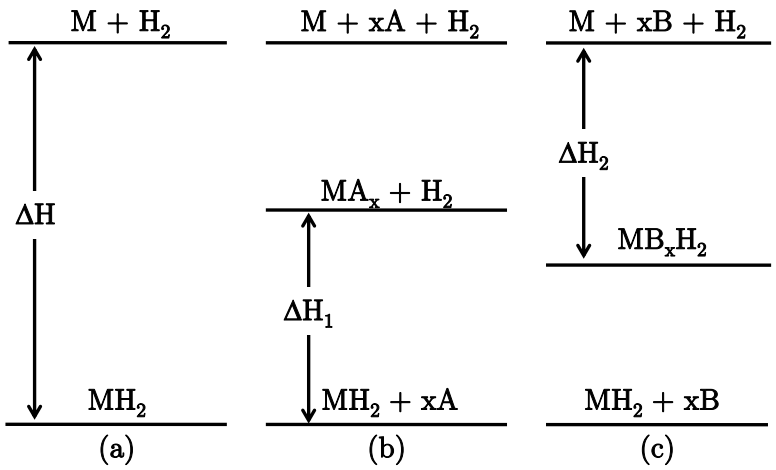

Figure 1.3: (a) The enthalpy of hydride formation given by the energy difference (ΔH) between the two states. (b) The element A forms a stable compound with M and reduces the energy difference to ΔH_2. (c) The elelement B creates a new destabilezd ternary hyride with the enthalpy of formation ΔH_2. (adapted from [28]).

The enthalpy of hydride formation is approximately 5 kJ/mole H_2 higher than that of pure Mg (-70 kJ/mole H_2). Similar scenarios have also been observed in the Mg-Si, Mg-Al and Mg-Sn systems [29-32]. In all these cases, the main drawback is the capacity loss caused by the addition of the alloying element. The gradual phase segregation of the system upon extended cycling is also another important issue in these alloys. A different scenario that may happen upon adding the alloying element is also illustrated in Fig. 1.3. In this case a ternary hydride will form that has different thermodynamics (ΔH_2) from the

original MgH_2. The Mg-Ni binary system is the well-known example of this case. Magnesium forms a stable Mg_2Ni intermetallic that forms the ternary hydride in according to the following reaction:

$$Mg_2Ni + 2H_2 \leftrightarrow Mg_2NiH_4 \quad \text{1-17}$$

The enthalpy of hydride formation is approximately -62 kJ/mole.H_2 in this case [33,34]. Magnesium does not form any intermetallic compound with most of transition metals (TMs). However, several ternary Mg-based hydrides have been produced using high energy mechanical alloying under hydrogen pressure. The Mg-Co, Mg-Fe and Mg-Mn are among these systems [34,35 and the references therein]. The slow sorption kinetics of these hydrides is usually the main drawback towards their practical use. Another system which has attracted a high level of research attention is the Mg-Ti system. The thin films of Mg-Ti system show the presence of a single hexagonal phase over a wide range of composition (55-95 at.% Ti). A reversible ternary hydride phase form upon hydrogenation. The structure of this ternary hydride has a strong dependence on the Ti content. The binary alloys with up to 10 at.% Ti addition show a rutile hydride phase. However, the alloys with higher content of Ti (Ti>13 at. %) form a fluorite ternary hydride. The enthalpy of formation of this hydride is obtained through the hydrogenography method and is in the range of -65 to -60 kJ/mole H_2 [36,37] which is still far from the practical goal (-40 kJ/mole H_2). Combining the allying effect of both Ni and Ti exhibited a significant enhancement in ternary Mg-Ni-Ti ternary thin film. The alloy with the composition of $Mg_{0.69}Ni_{0.26}Ti_{0.05}$ displayed the heat of formation of -40 kJ/mole H_2 [37]. However, as pointed out in a recent work by Zheng et al. [38] the entropy of the hydrogenation reaction is reduced in such a way that the plateau pressure is hardly affected in this system. Several works have also been dedicated to alter the formation enthalpy of MgH_2

by changing the structure of the original metal alloy. Zhang et al were able to successfully produce a bcc Mg-Co alloy [39]. Although the alloys showed improved absorption plateau pressure, the system was found to be irreversible. A recent study by Tan et. al also reported the formation of a meta-stable bcc alloy by addition of 25 at. % Nb to Mg [40]. The hydride structure remained bcc with slight volume difference due to the presence of interstitial hydrogen atoms. The enthalpy of formation was -52 kJ/mole H_2, however, the hydride phase did not desorb at temperatures below 175˚C and a gradual segregation of the Mg and Nb was observed after extended cycling.

Apart from the alloying, nanostructuring is another way of enhancing the thermodynamics properties of hydrides. Reducing the crystallite size of the metal/hydride phase to nanscale increases the interface to volume ratio. Hence, the interface contribution becomes more important and can alter the bulk properties of the materials. Several attempts have been made to reduce the grain/particle size of MgH_2 in order to achieve the desired thermodynamics [41 and reference therein]. It has been predicted that a 10% reduction in the heat of formation can be reached when the particle size falls to below 4 nm [28]. The results from density functional theory (DFT) also predicted a value below 2 nm for MgH_2 with destabilized thermodynamics [42]. For thin magnesium layer, a decrease in desorption temperature has been predicted for thicknesses of less than 10 unit cells [43]. The colloidal magnesium nanoparticles were successfully synthesized with dimensions as low as 5 nm [44]. Although a low desorption temperature of 85˚C has been achieved, slow kinetics and low reversible capacity were observed. Similar effect on the desorption temperature was observed in magnesium nanoparticle synthesized by digestive ripening at room temperature [45]. In a recent study the influence of the interface energy on the enthalpy of Mg/MgH_2 transformation was reported in detail [46]. Using a thin film

system with three layers of Ti/Mg/Ti, authors presented the methodology to obtain the interface energy from the thickness of the Mg layer and the plateau pressure. The thermodynamics of the reaction can then be tailored by means of this interface energy. Nanoconfinement of magnesium particles is also another method toward altering the enthalpy of metal-hydride transformation [47, 48]. It was realized by the early work done by Griessen et al. where they found a simple relationship between the heat of formation and the volume expansion [49]. Generally, by confining the volume expansion of the hydrding phase, the heat of formation can be altered. Through sandwiching the magnesium film between two layers of the elements which form stable alloy with Mg (Pd in this case), Baldi et.al showed that the equilibrium pressure can be increased [50,]. This behavior which is a result of elastic clamping effect was not observed when an immiscible element was used. However, a recent study attributed the above-mentioned effect solely to the allying of the Mg and Pd at the interface which subsequently affects the thermodynamics of MgH_2 formation [51]. Overall, to alter the thermodynamics of the magnesium hydride formation/decomposition is still the subject of ongoing research till the desired properties can be achieved.

1.4.2 Kinetics of hydrogenation

The slow kinetics of absorption and desorption reactions is another important hindrance for practical application of MgH_2 as a hydrogen storage system. The origin of this slow kinetics stems from the surface properties of magnesium, the mechanism of hydride formation and the structure of hydride. The surface oxidation of magnesium and/or formation of a magnesium hydroxide at the surface are the two important factors causing the slow kinetics. MgO acts as a barrier layer that hinders the diffusion of

hydrogen atoms toward the subsurface layers. In this case, a process so called activation is performed to break the oxide layer or dissolve the hydroxide [52,53]. Annealing at high temperatures and under vacuum or hydrogen pressure is usually considered as the activation process. The difference between the thermal expansion coefficients of pure Mg and MgO causes the surface oxide to crack and subsequently introduces new surfaces for further hydrogenation. Another type of activation process occurs upon successive absorption/desorption (cycling) of magnesium hydride. The reduction on the particle size and further cracking toward the interior of the particles are the origins of such activation [53]. Another important limiting factor for the hydrogenation rate of magnesium is the difficulty of the dissociation of hydrogen molecules at Mg surface [54]. It has been shown that high hydrogen dissociation energy barrier exists on the surface of clean Mg [55]. The occurrence of a chemisorption rate limiting step at the early stages of hydrogenation of the pure Mg is attributed to this energy barrier. To overcome this barrier, a key solution is to add transition metal (TM) elements as catalysts toward the dissociation/recombination of hydrogen molecules. It has been shown both experimentally and theoretically that TMs enhance the hydrogen sorption kinetics of pure magnesium [56,57,58]. The energy barrier on the surface of TMs for hydrogen dissociation is almost negligible compared to that for pure magnesium. The next barrier for the sorption kinetics is the diffusion of hydrogen atoms from the surface towards the subsurface layer and eventually into the bulk. For relatively large magnesium particle size, further hydrogenation results in the formation of a hydride layer at the surface [59]. The surface hydride layer significantly lowers the absorption rate due to the markedly lower diffusivity of magnesium hydride (in the order of 10^{-16}-10^{-25} m^2/s [60,61,62]) compared to that of pure magnesium (in the order of 10^{-8}-10^{-9} m^2/s [62,63]). The overall rate of the reaction is the

diffusion of hydrogen atom through this hydride shell. Such a structure is usually referred to as the core-shell microstructure. In order to prevent the formation of such structure and to reduce the diffusion distances in the system, nanostructuring is the key solution. Nanocrystalline Mg-based structures have been produced with the use of high-energy ball milling [52]. In fact, it is the combined effect of the nanostructuring and the presence of TMs catalyst which has resulted in Mg-based alloys with remarkably enhanced kinetics [56,57]. A detailed study by Pasturel et al. showed the role of different TM elements towards the absorption and desorption kinetics [64]. Authors concluded that the elements that form stable hydrides enhance the desorption kinetics of Mg while the elements forming dilute hydrides improve the absorption kinetics. The presence of catalysts elements would also enhance the rate of nucleation of Mg/MgH_2. It was shown that the nucleation sites move from the surface of the particles to the bulk material in Fe-catalyzed nanostructured Mg [65]. Many research efforts have also been dedicated to achieve the best kinetics in Mg-based systems in the form of thin films. The use of thin films provides an efficient structure to study the sorption kinetics of Mg in a very precise and controlled way to achieve the optimized composition and structure. Pure Mg think film with Pd capping layers showed very low absorption/desorption temperatures [66]. However, the consecutive expansion/contraction of the Mg layers would cause the Pd layer to peel off and lose its catalytic activity [67]. Various binary Mg-X thin films (X=Pd, Al, Ni, Sc, Cr, Nb, V, Ti) showed remarkably enhanced sorption kinetics compared to pure Mg thin film [68-71,40]. Apart from being model systems, other application potentials for Mg-based alloy thin films are switchable mirrors, hydrogen sensing and solar collector systems [70,72,73,74]. Thin films of Mg-Ni alloy capped with Pd layer have shown promising switchable mirror properties [70], however the degradation in the catalytic efficiency of Pd

layer upon extended cycling affects the performance of the films [75]. Adding a polymeric protecting layer could improve the properties of Mg-Ni thin film over 1000 cycles [76]. The Mg-Ti thin films also exhibited remarkable properties for smart solar collector and hydrogen detecting system applications with stable and fast kinetics over a large number of cycles [72,77,78]. The Mg-Ti systems showed superior optical and switching properties when compared to Mg-Ni [73]. For many Mg-X alloys where X is an immiscible element, the system suffers from strong phase segregation upon repeated hydrogenation. Interestingly, the Mg-Ti thin film are structurally reversible due to the accidentally equality in the molar volume of Mg and TiH_2 [79]. While the use of thin films has led to the structures with superior kinetics properties, the production of bulk samples with similar characteristics for practical hydrogen storage systems is still a challenge [80,81,82].

The intermetallic compounds of many transition metals can also can as catalysts toward the sorption kinetics of MgH_2. Compounds such as $LaNi_5$, FeTi, FeTiMn and some bcc alloys have been successfully added to MgH_2 and enhanced kinetics properties were observed [83,84,85]. The effect of addition carbon nanotubes (CNTs) on the sorption kinetics of MgH_2 is also investigated by numerous researchers [86,87]. The combined effect of the CNTs and transition metal nanoparticles on desorption rate and activation energy of the MgH_2 decomposition is thoroughly studies by Shalchi Amirkhiz et al. [88,89]. Authors found a synergy between of the two adding components in catalysing the sorption of MgH_2. Similar effect was also observed in the Mg-Fe-Ti co-milled samples where the ternary systems showed enhanced cycling stability and kinetics over binary Mg-Fe and Mg-Ti systems [90].

1.5 The motivation and scope of this thesis

The present thesis is mainly focused on the superior advantage of the use of bi-metallic catalyst over single metal TMs on the sorption kinetics of MgH_2. Generally, for a material to act as a catalyst several criteria must be met. The catalyst must have a negligible or very low dissociation energy barrier for hydrogen molecules and also must have high diffusivity for hydrogen atoms through its lattice (high diffusivity pathway). The positive heat of intermixing between the catalyst and Mg is also an important factor. This is due to the fact that the catalyst might lose its efficiency when forming a stable intermetallic compound with Mg. The formation of such intermetallic can consequently reduce the reversible capacity of the system. Most of the transition metals could satisfy these requirements. Moreover, in order to act as heterogeneous nucleation sites for Mg/MgH_2 nucleation and pinning point for the growth of Mg/MgH_2, the catalyst phase must be uniformly dispersed on magnesium (hydride) particles. It must also maintain such distribution throughout the course of cycling. This is an important factor in the case of Mg sorption cycling since temperature as high as 300˚C is usually required. We started our research based on the hypothesis that a bi-metallic catalyst possesses higher coarsening resistance over single metal addition, which accordingly leads to an enhanced distribution of catalyst particles over extended cycling. The selection of the elements for bi-metallic catalyst must be made based on the criterion of the negative enthalpy of mixing between the two elements. This is an essential requirement in the situations where a hydride forming element such as Ti is used. The segregation of the catalyst and the formation a stable hydride phase would cause the efficiency loss, further growth of the segregated phases and most likely the continuous growth of the Mg/MgH_2 over prolonged

cycling. We put our hypothesis to the test using thin film Mg-based ternary alloys produced by sputtering technique. The use of this technique allows for easy fabricating a variety of compositions in a controlled environment to achieve the optimized properties. The 1.5 μm-thick films of Mg-based alloys are usually capped by a Pd/Ta bi-layer. Palladium is used as a protective layer for the oxidation of the Mg and also to catalyse the first few sorption cycles. To prevent the interdiffusion of the Pd and underlying Mg, a thin layer of Ta was found to be an efficient solution [91,92]. The Mg-based alloy with the capping layer is deposited onto the Si substrate with a thin phororesist film as an interlayer. The use of photoresist allows for obtaining a free standing thin film when dissolving this layer in the acetone. Further information regarding the experimental details is provided in Chapter 2. Transmission and scanning electron microscopy and X-ray diffraction were employed to track the microstructural evolutions prior to and during the cycling tests. The volumetric Siverts apparatus was used for our sorption measurements and kinetics parameters were successfully obtained.

As shown in Chapter 3, we initially test our hypothesis by sputtering thin films of ternary Mg-Fe-Ti alloys. The hydrogen sorption kinetics of the ternary alloy is compared to those for binary Mg-Fe and Mg-Ti baselines. The optimum composition for ternary system is then proposed. Our materials show significant performance at 200˚C which is substantially lower than the commonly used temperature (>300˚C) for Mg-based alloys.

Chapters 4 and 5 present the further proof for our hypothesis using two ternary systems Mg-Fe-V and Mg-Cr-Ti. Again, the performances of these alloys over a large number of cycles are compared to their binary counterparts. The distribution of the catalyst is also shown using transmission electron microscopy.

In Chapter 6, we present the sorption cycling behavior of Mg-Cr-V system. The remarkable properties of this system enable us to fully absorb the alloy at room temperature and under low hydrogen pressure of 2 bar. We use electron microscopy techniques along with X-ray diffraction to explain the microstructural origin of this performance. We also perform a detailed kinetics analysis by incorporating the known nucleation and growth models. A correlation between the microstructural and kinetics analysis is then found and a new hydride growth is proposed.

1.6 References

1 P.P.Edwards, V.L.Kuznetsov, W.I.F.David, N.P.Brandon, Energy Policy 36, 4356-6432, (2008).

2 D.A. King, Science 303, 176-177, (2004).

3 A.G.Dutton, Tyndall Working Paper TWP17, http://www.tyndall.ac.uk/.

4 US Department of Energy, Report of the Basic Energy Sciences Workshop on Hydrogen Production, Storage and Use, Office of Science, Washington, DC, (2003), link.

5 US-DOE Hydrogen Storage Program Web-page: link.

6 J. Yang, A. Sudik, C. Wolverton, D. J. Siegel, Chem. Soc. Rev., 39, 656-675, (2010).

7 US-DOE. Annual Merit Review and Peer Evaluation Meeting, (2012), link.

8 V.A.Yartys and M.V.Lotoosky, Springer Netherlands, 75-104, (2005).

9 K. H. J. Buschow, P. C. P. Bouten and A. R. Miedema, Rep. Prog. Phys. 45, 937-1039, (1982).

10 K.J. Gross, , PhD thesis "Intermetallic Materials for Hydrogen Storage", University of Fribourg, Fribourg, (1998).

11 L. Schlapbach, In Hydrogen in Intermetallics I; Schlapbach, L. Ed.; Springer-Verlag: (1988).

12 L. Schlapbach and A. Züttel, Nature 414, p.p. 353-358, (2001).

13 R. Balasubramaniam, J. Alloy. Compd. 253-254, 203-206, (1997).

14 T. B. Flanagan, C.-N. Park and W. A. Oates, Prog. Solid St. Chem. 23, 291-363, (1995).

15 N. Gerard and S. Ono, In Hydrogen in Intermetallics II; L. Schlapbach, Ed.; Springer-Verlag: 1992.

16 T. Klassen, In Nanostructure Control of Materials, R. Hannink, AJ. Hill Ed ; Woodhead Publishing Limited, 266-302, (2006).

17 G. Barkhordarian, T. Klassen, R. Bormann, J. Alloy. Compd., 364, 242-246, (2004).

18 A.Borgschulte, R. Gremaud and R. Griessen, Phys. Rev. B., 78, 094106, (2008).

19 A. Züttel, Mater. Today, 6, 24-33, (2003).

20 K. Christmann, Surf. Sci. Rep., 1-3, 1-163, (1988).

21 M. Mintz, Y. Zeiri, J. Alloy. Compd., 216, 159-175, (1995).

22 W. Christian, "The Theory of Transformations in Metals and Alloys", Pergamon, Oxford, (1975).

23 T. Forde, J.P. Maehlen, V.A. Yartys, M.V. Lototsky, H. Uchida, Int. J. Hydrogen Energy 32, 1041-1049, (2007).

24 P. S. Rudman, J. Appl. Phys. 50, 7195, (1979).

25 JF. Stampfer, CE. Holley, JF. Suttle, J. Am. Chem. Soc. 82, 3504-3508, (1960).

26 F.S. Yang, G.X. Wang, Z.X. Zhang, X.Y. Meng, V. Rudolph, Int. J. Hydrogen Energy, 35, 3832-3840, (2010).

27 J. Reilly, R.Wiswall, Inorg. Chem. 6, 2220-2223, (1967).

28 V. Berube, G. Radtke, M. Dresselhaus and G. Chen, Int. J. Energy Res. 31, 637-663, (2007).

29 J. J. Vajo, F. Mertens, C. C. Ahn, R. C. Bowman and B. Fultz, J. Phys. Chem. B 108, 13977-13983, (2004).

30 R. Domenech-Ferrer, M.G. Sridharan, G. Garcia, F. Pi, J. Rodriguez-Viejo, J. Power Sources, 169, 117-122, (2007).

31 H. Fritzsche, M. Saoudi, J. Haagsma, C. Ophus, E. Luber, C. T. Harrower and D. Mitlin, Appl. Phys. Lett. 92, 121917, (2008).

32 H. Imamuraa, K. Yoshihara, M Yoo, I. Kitazawa, Y Sakataa, S. Ooshim, Int. J. Hydrogen Energy, 32, 4191-4194, (2007).

33 J. Reilly Jr, R.H Wiswall Jr, Inorg. Chem. 7, 2254-2256, (1968).

34 A. Reiser, B. Bogdanovic, K. Schlichte, Int. J. Hydrogen Energy, 25, 425-430, (2005).

35 A. Andreasen, Predicting formation enthalpies of metal hydrides. Ris National Laboratory Report, Ris-R-1484(EN) (2004).

36 D. M. Borsa, R. Gremaud, A. Baldi, H. Schreuders, J. H. Rector, B. Kooi, P. Vermeulen, P. H. L. Notten, B. Dam and R. Griessen, Phys. Rev. B, 75 205408, (2007).

37 R. Gremaud, C. P. Broedersz, D. M. Borsa, A. Borgschulte, P. Mauron, H. Schreuders, J. H. Rector, B. Dam, R. Griessen, Adv. Mater., 19, 2813–2817, (2007).

38 Q. Zheng, Y. Pivak, L.P.A. Mooij, A.M.J. van der Eerden, H. Schreuders, P.E. de Jongh, J.H. Bitter, B. Dam, Int. J. Hydrogen Energy, 37, 4161-4169, (2012).

39 Y. Zhang, Y Tsushio, H. Enoki and Etsuo Akiba, J. Alloy. Comp., 393, 147-153, (2005).

40 X. Tan , L. Wang , C.M.B. Holt , B. Zahiri , M. Eikerling and D. Mitlin, Phys. Chem. Chem. Phys., accepted manuscripts, (2012).

41 Ki Chul Kim, Bing Dai, J.K. Johnson, D.S. Sholl, Nanotechnology, 20, 204001, (2009).

42 R.W.P. Wagemans, J.H.V. Lenth, P.E. de. Jongh, A.J.V. Dillen, K.P. de. Jong, J. Am. Chem. Soc., 127, 16675–16680, (2005).

43 J.J. Liang, Appl. Phys. A 80, 173–178 (2005).

44 K.-F. Aguey-Zinsou, J.-R. Ares-Fernández, Chem. Mater., 20, 376–378, (2008).

45 S.B. Kalidindi, B.R. Jagirdar, Inorg. Chem., 48, 4524–4529(2009).

46 L.P.A. Mooij, A. Baldi, C. Boelsma, K. Shen, M. Wagemaker, Y. Pivak, H. Schreuders, R. Griessen, B. Dam, Adv Energy Mater, 1 (5), 754–758, (2011).

47 T.K. Nielsen, F. Besenbacher and T.R. Jensen, Nanoscale, 3, 2086-2098, (2011).

48 R. Bardhan, A.M. Ruminski, A. Brand, J.J. Urban, Energy Environ. Sci., 4(12), 4882-4895, (2011).

49 R. Griessen, R. Feenstra, J. Phys. F: Met. Phys., 15(4), 1013-1019, (1985).

50 A. Baldi, M. Gonzalez-Silveira, V. Palmisano, B. Dam, R. Griessen, Phys. Rev. Lett. 102(22), 226102, (2009).

51 C.-J. Chung, S. Lee, J.R. Groves, E.N. Brower, R. Sinclair, B.M. Clemens, Phys. Rev. Lett. 108(10), 106102, (2012).

52 A. Zaluska, L. Zaluski, J.O. Ström–Olsen, J. Alloy. Compd., 288(1-2), 217-225, (1999).

53 P.S. Rudman, J. Less Common. Met., 89(1), 93-110, (1983).

54 L. Schlapbach, In Hydrogen in Intermetallics II; L. Schlapbach, Ed.; Springer-Verlag: 1992.

55 J.K. Norskov, A. Houmoller, P. Johansson and B.I. Lundquist, Phys. Rev. Lett. 46, 257-260, (1981).

56 N. Hanada, T. Ichikawa, H. Fuji, J. Phys. Chem. B, 109, 7188-7194, (2005).

57 G. Liang, J. Huot, S. Boily, A.V. Nestea, R. Schulz, J. Alloy. Comp., 292(1-2), 247-252, (1999).

58 M. Pozzo, D. Alfe, Int. J. Hydrogen Energy, 34, 1922–1930, (2009).

59 H.Y. Tien, M. Tanniru, C.Y. Wu, F. Ebrahimi, Int. J. Hydrogen Energy, 34, 6343, (2009).

60 S. Hao and D.S. Sholl, Appl. Phys. Lett., 93, 251901, (2008).

61 X. Yao, Z.H. Zhu, H.M. Cheng, G.Q. Lu, J. Mater. Res., 23(2), 336-340, (2008).

62 J. Cermak and L. Kral, Acta Mater., 56, 2677-2686, (2008).

63 H.G. Schimmel, G.J. Kearley, J. Huot, F.M. Mulder., J. Alloy. Compd., 404, 235-237, (2005).

64 M. Pasturel, R.J. Wijngaarden, W. Lohstroh, H. Schreuders, M. Slaman, B. Dam, and R. Griessen, Chem. Mater. 19, 624 (2007).

65 M. Vittori Antisari, A. Aurora, D.M. Gattia, A. Montone A., Scr. Mater., 61, 1064-1067, (2009).

66 K. Higuchi, K. Yamamoto, H. Kajioka, K. Toiyama, M. Honda, S. Orimo and H. Fujii, J. Alloy. Compd., 330-332, 526-530, (2002).

67 A. Remhof and A. Borgschulte, ChemPhysChem, 9, 2440-2455, (2008).

68 M. Pasturel, M. Slaman, H. Schreuders, J. H. Rector, D. M. Borsa, B. Dam, and R. Griessen, J. Appl. Phys., 100, 023515 (2006).

69 R. Gremaud, A. Borgschulte, C. Chacon, J.L.M. van Mechelen, H. Schreuders, A. Züttel, B. Hjörvarsson, B. Dam and R. Griessen, Appl. Phys. A, 84, 77-85, (2006).

70 T.J. Richardson, J.L. Slack, R.D. Armitage, R. Kostecki, B. Farangis, and M.D. Rubin, Appl. Phys. Lett., 78, 3047, (2001).

71 R.A.H. Niessen and P.H.L. Notten, Electrochem. Solid-State Lett., 8(10), 534-538, (2005).

72 A. Baldi, D.M. Borsa, H. Schreuders, J.H. Rector, T. Atmakidis, M. Bakker, H.A. Zondag, W.G.J. van Helden, B. Dam, and R. Griessen, Int. J. Hydrogen Energy, 33(12), 3188-3192, (2008).

73 M. Slaman, B. Dam, M. Pasturel, D.M. Borsa, H. Schreuders, J.H. Rector, R. Griessen, Sens. Actuators, B, 123(1), 538-545, (2007).

74 M. Slaman, , B. Dam, H. Schreuders, and R. Griessen, Int. J. Hydrogen Energy, 33(3), 1084-1089, (2008).

75 K. Yoshimura, Y. Yamada, S. Bao, K. Tajima, M. Okada, Jpn. J. Appl. Phys., 46, 4260-4264, (2007).

76 S. Bao, Y. Yamada, M. Okada, K. Yoshimura, Appl. Surf. Sci., 253, 6268-6272, (2007).

77 S. Bao, K. Tajima, Y. Yamada, M. Okada and K. Yoshimura, Appl. Phys. A, 87, 621–624, (2007).

78 K. Tajima, Y. Yamada, S. Bao, M. Okada, and K. Yoshimura, Appl. Phys. Express 1, 067007, (2008).

79 A. Baldi, R. Gremaud, D.M. Borsa, C.P. Balde, A.M.J. van der Eerden, G.L. Kruijtzer, P.E. de Jongh, B. Dam, R. Griessen, Int. J. Hydrogen Energy, 34, 1450-1457, (2009).

80 W. P. Kalisvaart and P. H. L. Notten, J. Mater. Res., 23, 2179-2187, (2008).

81 K. Asano, H. Enoki and E. Akiba, J. Alloys Compd., 478, 117-120, (2009).

82 Y. J. Choi, J. Lu, H. Y. Sohn, Z. Z. Fang and E. Ronnebro, J. Phys. Chem. C, 113, 19344-19350, (2009).

83 P. Mandal and O.N. Srivastava, , Journal of Alloys and Compounds 205, 111-118, (1994).

84 G. Liang, J. Huot, S. Boily, A. Van Neste and R. Schulzb, J. Alloy. Compd., 297, 261-265, (2000).

85 T. Kondo, K. Shindo and Y. Sakurai, . Alloy. Compd., 404-406, 511-514, (2005).

86 Z.G. Huang, Z.P. Guo, A. Calka, D. Wexler, H.K. Liu, J. Alloy. Compd. 427(1-2), 94-100, (2007).

87 C.Z. Wu, P. Wang, X. Yao, C. Liu, D.M. Chen, G.Q. Lu, H.M. Cheng, J. Alloy. Compd. 420(1-2), 278-282, (2006).

88 B.S. Amirkhiz, M. Danaie, and D. Mitlin ,Nanotechnology, 20, 204016, (2009).

89 B.S. Amirkhiz, M. Danaie, M. Barnes, B. Simard, and D. Mitlin, J. Phys. Chem. C, 114(7), 3265-32-75, (2010).

90 B.S. Amirkhiz, B. Zahiri, P. Kalisvaart, and D. Mitlin, Int. J. Hydrogen Energy, 36(11), 6711-6722, (2011).

91 H. Fritzsche, C. Ophus, C. T. Harrower, E. Luber, and D. Mitlin, App. Phys. Lett., 94, 241901 (2009).

92 X. Tan, C.T. Harrower, B.S. Amirkhiz and D. Mitlin, Int. J. Hydrogen Energy, 34, 7741 (2009).

2 Experimental

2.1 Thin film Deposition

All the materials tested in this thesis were fabricated by magnetron sputtering technique in the form of thin films. Similar to other thin film deposition methods, sputtering involves condensing a gas phase of a material onto a substrate of another material. In sputtering, the ions of a noble gas are utilized to eject atoms from the target surface in a vacuum chamber. Some of the ejected atoms travel through the chamber to deposit the desired thin film on the substrate. Detailed information regarding different stages of sputtering process and the proper conditions can be found in numerous texts, e.g. Ref [1]. The schematic representation of deposited material on the substrate is shown in Figure 2.1(a). The Si substrate of 4-inch in diameter is used for all materials. Prior to the deposition, a thin layer photoresist is applied on the substrate using spin coating. The photoresist layer enables separation of the sample from the substrate to obtain a free-standing film. The hydrogen storing materials which is a Mg-based alloy (1.5 μm-thick) is then deposited using magnetron sputtering. We use Ar gas with a purity of grade 5 at a sputtering pressure of $5x10^{-3}$ mbar, with a maximum base pressure of $5x10^{-8}$ mbar.

Depositions are done in a sputter-up configuration with continuous substrate rotation. Film thickness and deposition rates were obtained through the use of crystal deposition rate monitor held at the substrate plane. As can be seen in Fig. 2.1, a Pd surface cap was coated onto both sides of the as-synthesized film so as to prevent the oxidation of the magnesium surfaces. This layer would also act as catalyst for hydrogen

dissociation/recombination during the initial stages of hydrogen sorption cycling. A nano-scale layer of Ta is also utilized as an intermediate between the Mg-based alloy and the Pd. This was done because Ta was demonstrated to be effective in reducing the rate of elevated temperature Mg-Pd intermetallic formation during the initial hydrogen absorption step [2,3]. The deposition rates of Mg, Pd and Ta are normally set to the following: Mg 0.3; Pd 0.17; Ta 0.03 nm/sec; the rates for the adding catalyst elements are then varied to adjust for different film stoichiometries. Depositions of the catalysts and of the bulk Mg are performed sequentially without any interruption. After deposition the photoresist is washed away using acetone allowing the films to be fully released from the Si wafer. Release from the substrate allowed the films to be treated as free flakes several tens to about one hundred micrometers in diameter each (Figure 2.1 (b)).

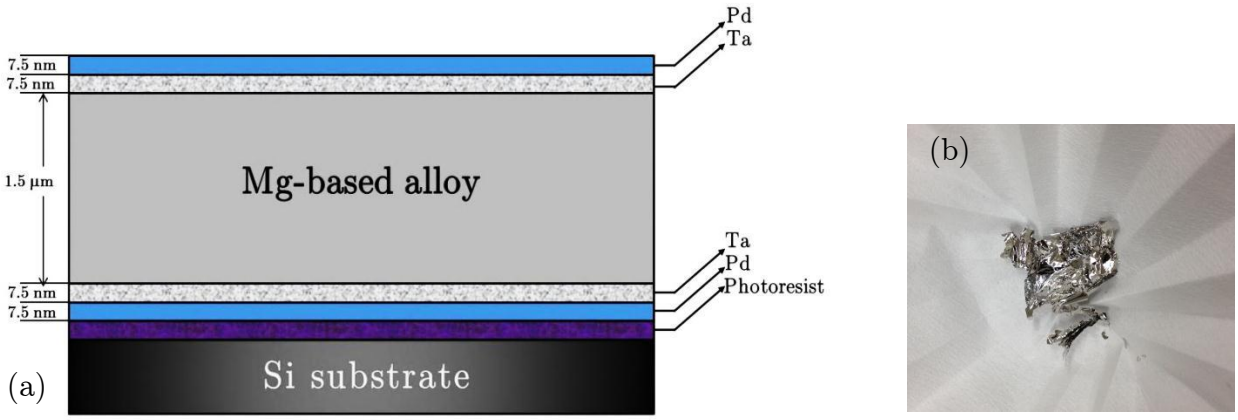

Figure 2.1: (a) The schematics of the Mg-based alloys with catalyst bilayer on the substrate. (b) Free-standing thin film.

2.2 Kinetics and thermodynamics measurements

Absorption and desorption tests are performed at different temperatures in a Siverts type instrument (Hy-Energy LLC. PCTPro 2000). Generally, in Sieverts method the hydrogen sorption is measured by monitoring the hydrogen pressure variation in a system with fixed and known volume. Details of such method can be found in Ref [4].

Typical sample mass for these measurements are 10-20 mg. For cycling tests at 200˚C, the absorption is usually starts with the pressure of 3 bar in the reservoir volume of 11.89 ml. The pressure drops to around 1.5 bar towards the end of absorption. The starting and final pressure values for cycling at 300˚C are 4.5 and 3 bar. For desorption, the reservoir of volume 1025 is first put under rough vacuum. Upon the expansion of the remaining hydrogen in the sample holder, the initial pressure of 5 mbar is the result. This value raise to 15-20 mbar toward the end of desorption. The system automatically switches from absorption to desorption, and vice versa, once the sorption rate fall below 0.004 wt. %/min. After each desorption, the sample is evacuated before the next absorption starts.

2.3 Microstructural characterization

In this thesis, three main methods are used to investigate the microstructure of samples at different stages of cycling. X-ray diffractometry (XRD) is utilized to obtain the information form the structure of as-deposited and cycled sample (absorbed and desorbed). In the case of as-deposited samples, a single flake of the free-sanding film is placed on XRD glass slides and held using a thin layer of glue. The cycled samples

normally resemble a mixture of small flakes. Mortar a pestle is used in order to achieve a uniform powder mixture. The sample is then placed in a glass holder and pressed in order to ensure it remains steady during the measurement. A Rigaku Ultima III X-ray diffractometer with Cu-K_α radiation source (λ=1.5406 Å) is employed for these measurements. The XRD pattern is then used to identify the present phases and also to obtain the grain size and strain information.

After prolonged hydrogen cycling, the samples still resembled small flakes of thin films combined with agglomerated particles. Thus, additional thinning process was required to achieve electron transparency. This was performed via mortar and pestle grinding.

Scanning electron microscopy (SEM) is utilized to track the morphological changes of samples during sorption cycling. Transmission electron microscopy (TEM) is also used to obtain cite-specific information form the samples. Conventional TEM analysis is performed using the JEOL-JEM 2100 microscope, operating at 200 kV accelerating voltage. High resolution TEM (HRTEM) analysis is performed on an FEI Titan 80-300 microscope equipped with an aberration corrector for the image-forming lens. The accelerating voltage is set at 300 kV and the spherical aberration coefficient is close to 1 μm during HRTEM experiments. As mentioned above, the samples consist of small flakes after prolonged cycling. Hence, additional thinning required for TEM analysis is obtained via mortar and pestle grinding. The samples then are spread onto a copper grid that is supported by a thin layer amorphous carbon. TEM analysis of the MgH_2 is performed using a liquid nitrogen cooled cryo-stage so as to minimize beam damage and in-situ desorption during analysis [5]. During the cryo-stage TEM, the temperature at the tip of sample holder is usually recorded and kept at liquid nitrogen temperature. It is arguable

that the actual sample particles on the grid might have a different temperature. However, we can argue that the sample temperature is so low that it allows for performing conventional TEM analysis before decomposition. More accurate temperature measurements are required to indicate the actual temperature of the sample.

2.4 References

[1] Ohring M. (Ed.), "Materials Sciences of Thin Film: Deposition and Structure", Academic Press Ltd., USA, 1992.

[2] Fritzsche, H.; Ophus, C.; Harrower, C.T.; Luber, E.; Mitlin, D.; Appl. Phys. Lett., 2009, 94, 241901.

[3] Fritzsche, H.; Saoudi, M.; Haagsma, J.; Ophus, C.; Luber, E.; Harrower, C.T.; Mitlin, D. Appl. Phys. Lett. 2008, 92, 121917.

[4] Gross, K.J.; Carrington, K.R. "DOE: Recommended Best Practices for the Characterization of Storage Properties of Hydrogen Storage Materials", V 31, 2008.

[5] Danaie M.; Mitlin, D. J. Alloys Compd. 2009, 476, 590.

3 Rapid and Reversible Hydrogen Sorption in Mg-Fe-Ti Thin Films

Material in this chapter has been published in:
Beniamin Zahiri, Chris. T Harrower, Babak Shalchi Amirkhiz, and David Mitlin, Appl. Phys. Lett. 95, 103114, (2009)

3.1 Introduction

Magnesium-based thin films and nanostructures are a subject of extensive research as they are becoming increasingly more utilized for optical hydrogen sensing, switchable mirrors and solar absorbers, and as model alloys for designing and understanding bulk hydrogen storage materials [e.g., Refs. 1-7]. Binary Mg-Fe and Mg-Ti alloys are a subject extensive research since they possess significantly accelerated kinetics relative to other Mg-based systems [8-16]. The ternary Mg-Fe-Ti system has not received the same level of attention for hydrogen-related applications. Work on Mg-Fe-Ti and Mg-Fe-Ti-Mn bulk alloy powders was performed by several groups [17-20], with the authors generally reporting favorable hydrogenation kinetics and good capacity (~3wt.%). As will be shown in this manuscript, the ternary Mg-Fe-Ti system in thin film form holds promise for substantially improved performance in many of the applications where pure Mg, Mg-Fe and Mg-Ti films are utilized.

3.2 Experimental

The geometry of the samples was a 1.5μm Mg-Fe-Ti films with a 7.5nm Pd /7.5nm Ta bi-layer catalyst on both top and the bottom surfaces. The films had compositions Mg-

10at.%Fe-10Ti, Mg-15at.%Fe-15Ti and Mg-20at.%Fe-20Ti. This intermediate layer serves the critical role of reducing the highly deleterious interdiffusion between the Pd and the underlying hydrogen storing material [21]. In this study tantalum is chosen as the intermediate layer because it has been demonstrated to be effective in preventing elevated temperature interdiffusion of Pd and the underlying Mg during hydrogen sorption [22,23]. The deposition rates were the following: Mg 3; Pd 1.7; Ta 0.3 Å/sec; Fe and Ti varied to adjust for stoichiometry. Volumetric absorption and desorption measurements were performed on a Sieverts hydrogen sorption analysis system (Hy-Energy LLC. PCTPro 2000). All the measurements were carried out at 200˚C. Mg was absorbed at a pressure near 3 bar and desorbed at a pressure near 0.001 bar. Additional details regarding the synthesis and the materials characterization are provided in Ref. 23.

3.3 Results and Discussion

Figures 3.1(a) and (b) shows the absorption and desorption behavior for the Mg-15at.%Fe-15Ti alloys, tested at 200˚C. The roughness of the desorption curves (Fig. 3.1(b)) is due to instrumental noise. There is an activation period where the absorption kinetics are significantly slower (order of magnitude) than at steady-state. On the desorption side an activation period also exists but represents only a moderate slowdown (factor of 2) relative to the long-term cycling kinetics. However by cycle 5 both the absorption and the desorption kinetics are stabilized with the system essentially behaving identically from then on. The 10^{th}, 50^{th} and 100^{th} cycles are all identical, with no apparent degradation in either the capacity or the sorption times.

The initial activation period may be due to a variety of microstructural factors. The as-synthesized films were composed of supersaturated solid solutions of Fe and Ti in Mg, with the Mg having a strong [0001] fibre texture. Ultimately the film will decompose into an equilibrium two-phase mixture of magnesium (α-MgH_2 in sorbed state) and FeTi. At 200˚C neither the Fe nor the Ti have any appreciable solubility in magnesium. However

such microstructure may not be rapidly achievable from a solid solution. Most likely it rather evolves during several initial cycles. One hypothesis is that until the minority FeTi phase fully precipitates the kinetics remain sluggish. Another scenario is related to the structure of the bi-layer Pd/Ta surface catalyst used in this work. The activation period may be attributed to the interdiffusion of the two elements to make a catalytic Ta-Pd alloy, or to the ultimate formation of a tantalum hydride phase. We plan to investigate the microstructural origins of this activation period in follow-up research. Interestingly, the slow kinetics period lasting up to 5 cycles along with the subsequent steady-state behavior was a prominent feature of every composition tested in this study.

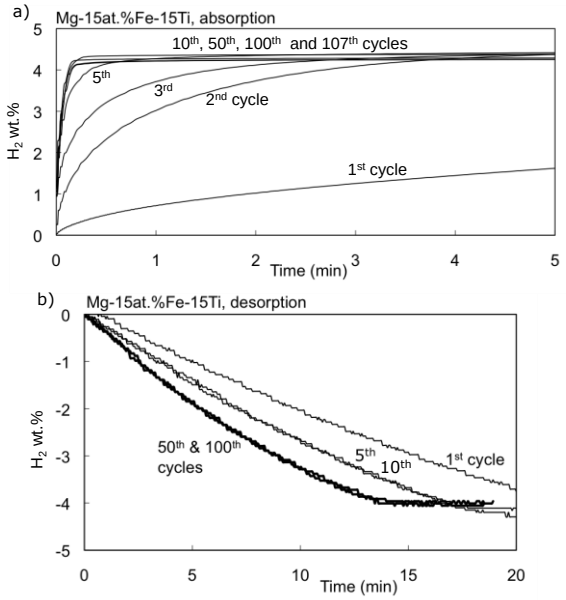

Figure 3.1: a) Absorption and b) desorption behavior over cycles 1-107 for Mg-15at.%Fe-15at.%Ti alloy at 200˚C.

Figure 3.2 shows the indexed XRD pattern of the post-cycling, steady-state sorbed microstructure of the Mg-10at.%Fe-10Ti alloy. The broad peak centered at $2\theta \sim 18.5^{\circ}$ is due to the quartz mounting slide used to support the powders. The most prominent peaks may be unambiguously indexed to belong to α-MgH_2 phase, with no detectable variation

of the lattice parameter from the literature-reported values. The α-MgH_2 phase is tetragonal with the space group $P4_2/mnm$ (136), the lattice parameters a=0.45176 and c=0.30206 Å, and Wyckoff Positions Mg (2a): 0, 0, 0, and H (4f): 0.304, 0.304, 0. Mg_6Pd peaks are also present, indicating that the catalyst did react with the base material. The Mg_6Pd phase is cubic with the space group F-43m (216) and a lattice parameter of 20.108Å. Three of the most intense Mg_6Pd peaks, (224), (066) and (446) are labeled in the figure. In addition there appears to be a broad "x-ray amorphous" peak (which could be due to an amorphous phase, a nanocrystalline phase or a mixture of both) that overlaps with the (446) and (066) Mg_6Pd peaks. This broad peak is centered around 2θ = 37.5˚ and is likely due to an amorphous/nanocrystalline FeTi phase since no characteristic FeTi peaks were detected.

The fact that Mg_6Pd forms despite the presence of a Ta underlayer is an interesting result. When using a single layer Pd catalyst thermal effects drive the interdiffusion of Mg and Pd, and the subsequent formation of Mg_6Pd and MgO [24]. However even when a refractory underlayer is present, similar interediffusion may occur. Since Pd and Ta have appreciable mutual solubility at 200˚C (~9at.%Pd in Ta, and ~15at.%Ta in Pd) the formation of Mg_6Pd after multiple cycles is feasible. It is not possible to conclusively identify or negate the presence of β-$TaH_{0.5}$ since its XRD peaks overlap those of Mg_6Pd. For example the most intense peak of β-$TaH_{0.5}$, (111) at 2θ = 37.5˚, would experimentally overlap with the second most intense peak of Mg_6Pd, (066) at 2θ = 38˚. The (020), (200), (002) and (220) peaks of β-$TaH_{0.5}$ would similarly do that.

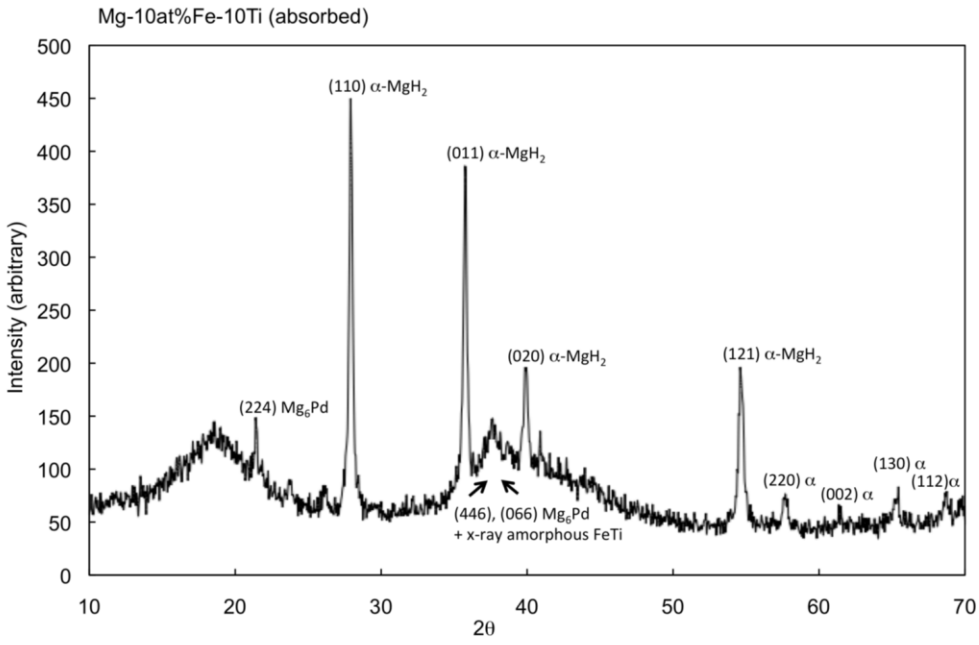

Figure 3.2: Indexed X-ray diffraction pattern of the sorbed Mg-10at.%Fe-10Ti alloy. The broad unlabeled peak centered at $2\theta \sim 18.5^{\circ}$ is due to the quartz mounting support.

Figure 3.3 compares the steady-state (sixth cycle) absorption and the desorption behavior of the films as a function of Fe/Ti content. The alloys display quite similar kinetics. A comparison of the absorption and desorption curves implies analogous microstructures and sorption enhancement mechanisms for the three alloys. However the three alloys possess different hydrogen capacities. Assuming that α-MgH_2 is the only hydrogen storing phase present in the microstructure and neglecting the catalyst layers, the theoretical hydrogen capacities of the Mg-10at.%Fe-10Ti, Mg-15at.%Fe-15Ti, Mg-20at.%Fe-20Ti alloys are 5.1, 4.1 and 3.2 wt.%. Comparing these values to Figure 3.4 and

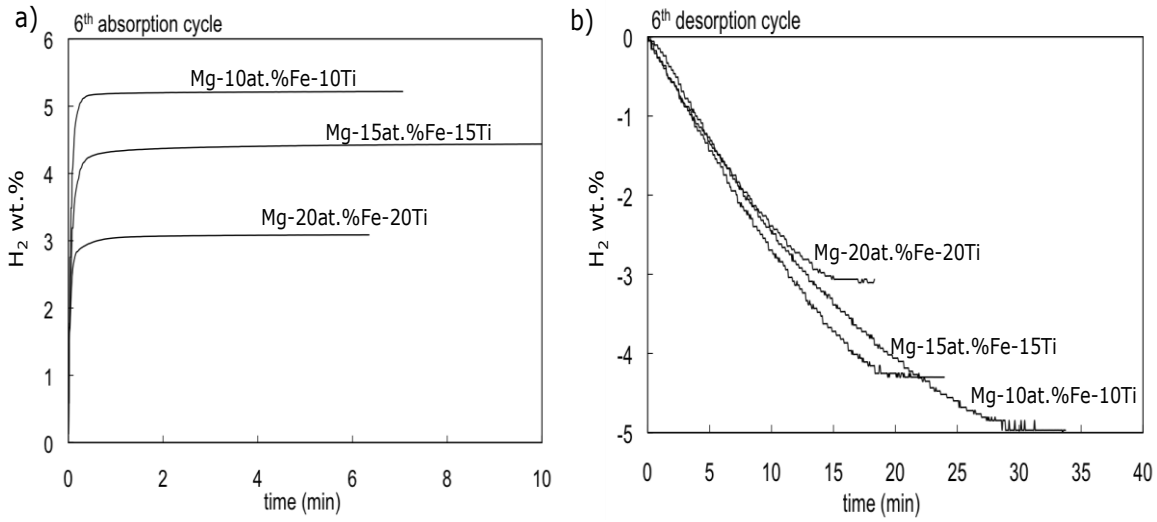

Figure 3.3: Absorption a) and desorption b) behavior at sorption cycle #6 for the three alloys examined.

allowing for some (less than 10%) capacity reduction due to the presence of the catalysts layers we can conclude that the system is quite close to being fully sorbed.

Figure 3.4 compares the time to absorption (a) and time to desorption (b) as a function of cycle number and alloy content. There is a noticeable induction period during the first several cycles of absorption. Interestingly at steady-state the higher FeTi content alloy (Mg-20at.%Fe-20Ti) actually absorbs hydrogen at a slower rate than the lower content alloys. The absorption times observed for Mg-15at.%Fe-15Ti alloys are the fastest ever reported for a relatively thick (1.5 micrometer) Mg-based film. Figure 3.4 (b) indicates that the optimum desorption performance, both in terms of the rates and in terms of the stabilities, is achieved in the Mg-15at.%Fe-15Ti alloy. The lower Fe/Ti content film has slower kinetics, while the higher alloy content film begins to display some kinetic degradation after about 20 cycles.

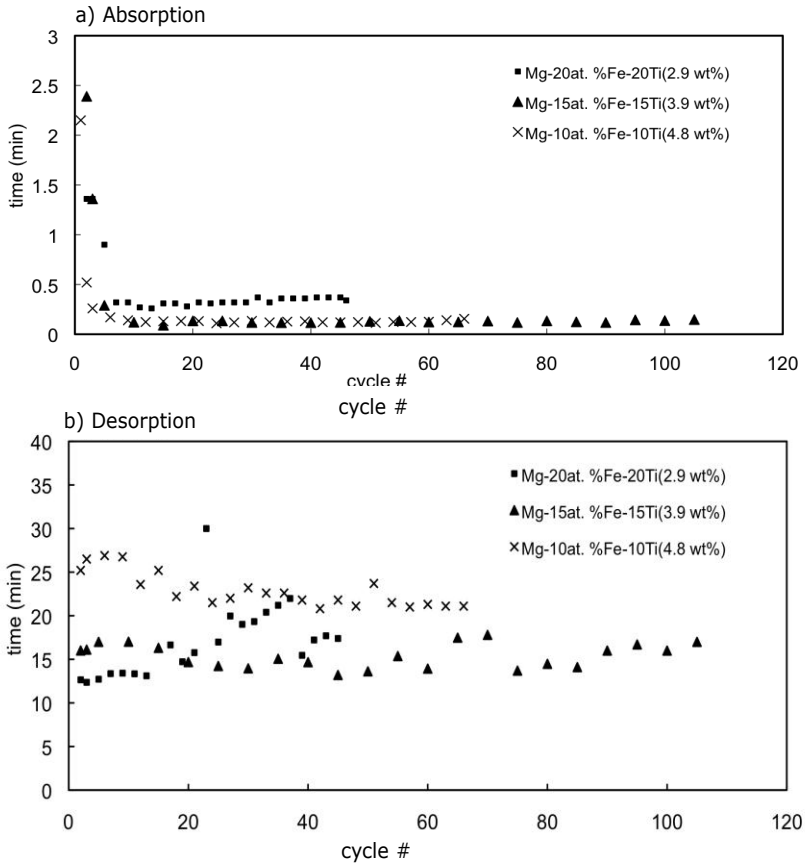

Figure 3.4: A comparison of a) time to absorb, and b) time to desorb as a function of sorption cycle number.

Whether the sorption enhancement is due to improved kinetics or fundamentally different thermodynamics depends on the hydride phases that are formed. For the system to be significantly destabilized the well-known rule of reversed stability should be operative [25]. When the main hydrogen-storing phase is α-MgH_2, no net reduction of its heat of formation is possible by the formation of TiFe or $TiFe_2$ upon desorption. Since there is no evidence of ternary hydride Mg_2FeH_6, and no evidence that the α-MgH_2 possesses a fundamentally different structure (i.e. destablized due to alloying), we have to conclude that rapid sorption behavior of the films is due to better kinetics. This conclusion, at least for the Mg-10at.%Fe-10Ti alloy, is supported by the pressure –

composition isotherm absorption and desorption data shown in Figure 3.5. The calculated enthalpies agree with the -72 to -79 kJ/mol H_2 ΔH values for α-MgH_2.

For FeTi, the heat of hydride formation varies with the hydrogen content (multiple plateaus) but is in the -28 to -35 kJ/mol H_2 range[26]. At 200˚C and 3 bar none of the FeTi-hydride phases will be stable, although hydrogen will remain in the intermetallic as an interstitial solid solution. From a kinetic point of view, Ti and Fe are known to be individually catalytic for hydrogen dissociation/re-association in the magnesium system. Combining these elements may be synergistic. Moreover hydrogen diffusivity of FeTi solid solution is rapid. If this phase continuously dispersed throughout the MgH_2 grains, it may act as an effective pathway for hydrogen diffusion in and out of the system. We intent to explore the FeTi phase distribution within MgH_2 using transmission electron microscopy analysis similarly to what was done in Refs. 27 and 28.

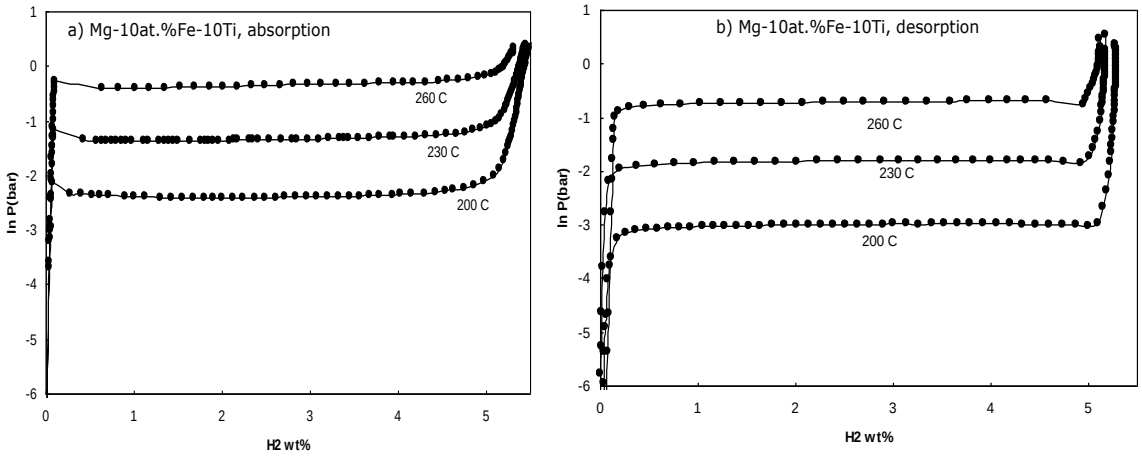

Figure 3.5: Pressure – composition isotherm absorption and desorption data for Mg-10at.%Fe-10Ti.

Acknowledgement: This work was supported by NINT NRC and NSERC Discovery.

3.4 References

[1] Baldi A., Gremaud R., Borsa D.M., Baldeȷ C.P., van der Eerden A.M.J., Kruijtzer G.L., de Jongh P.E., Dam B., Griessen R., Int. J. Hyd. Energy 34, 1450 (2009).

[2] L. Pasquini, E. Callini, E. Piscopiello, A. Montone, M.V. Antisari, E. Bonetti, Appl. Phys. Lett., 94, 041918 (2009).

[3] Y.P. He, Y.P. Zhao, L.W. Huang, H. Wang and R.J. Composto, Appl. Phys. Lett., 93, 163114 (2008).

[4] P. Vermeulen, P.C.J. Graat, H.J. Wondergem and P.H.L. Notten, Int. J. Hyd. Energy 33, 5646 (2008).

[5] H. Fritzsche, M. Saoudi, J. Haagsma, C. Ophus, E. Luber, C.T. Harrower and D. Mitlin, Appl. Phys. Lett. 92, 121917 (2008).

[6] Y.P. He, Y.P. Zhao and J.S. Wu, Appl. Phys. Lett. 92, 063107 (2008).

[7] N. Bazzanella, R. Checchetto and A. Miotello, Appl. Phys. Lett., 92, 051910 (2008).

[8] J.-M. Welter and P.S. Rudman, Script. Metall. 16, 285 (1982).

[9] P. Selven, K. Yvon, Int. J. Hydrogen Energy 16, 615 (1991).

[10] B. Bogdanovic, A. Reiser, K. Schlichte, B. Spliethoff, B J. Tesche, Alloys Comp. 345, 77 (2007).

[11] J. Huot, H. Hayakawa and E. Akiba, J. Alloy. Comp. 248, 164 (1997).

[12] D.M. Borsa, R. Gremaud, A. Baldi, H. Schreuders, J.H. Rector, B. Kooi B, P. Vermeulen P.H.L. Notten, B. Dam and R. Griessen, Phys. Rev. B. 75, 205408 (2007).

[13] G. Liang, J. Huot, S. Boily, A. Van Neste and R. Schulz, J. Alloy and Comp. 292, 247 (1999).

[14] T.J. Richardson, J.L. Slack, B. Farangis and M.D. Rubin, Appl. Phys. Lett. 80 1349 (2002).

[15] R.A.H. Niessen and P.H.L. Notten, Electrochem. and Solid State Letters 8, A534-A538 (2005).

[16] J.J. Didisheim, P. Zolliker, K. Yvon, P. Fischer, J. Schefer, M. Bubelmann, A.F. Williams, Inorg. Chem. 23, 1953 (1984).

[17]P. Mandal and O.N. Srivastava, J. Alloys and Comp. 205, 111 (1994).

[18]P. Mandal, K. Dutta, K. Ramakrishna, K. Sapru and O.N. Srivastava, J. Alloys and Comp. 184, 1 (1992).

[19] G.X. Liang, E.D. Wang, and S.S. Fang, J. Alloys and Comp. 223, 111 (1995).

[20] P. Wang, A. M. Wang, B.Z. Ding BZ, and Z.Q. Hu, J. Alloys Compd. 334, 243 (2002).

[21] J. L. Slack, J. C. W. Locke, S. W. Song, J. Ona, and T. J. Richardson, Sol. Energy Mater. Sol. Cells 90, 485 (2006).

[22] H. Fritzsche, C. Ophus, C. T. Harrower, E. Luber, and D. Mitlin, App. Phys. Lett., 94, 241901 (2009).

[23] X. Tan, C.T. Harrower, B.S. Amirkhiz and D. Mitlin, Int. J. Hydrogen Energy, 34, 7741 (2009).

[24] E. Johansson, C. Chacon, C. Zlotea, Y. Andersson, and Bjorgvin Hjorvarsson, J. Phys.: Condens. Matter 16 7649 (2004).

[25] A.R. Miedema, K.H.J. Buschow and H.H. van Mal, J. Less. Com. Metal., 49, 463 (1976).

[26] Hydrogen in Metals I (Topics in Applied Physics), edited by G. Alefeld and J. Volkl, Springer-Verlag, Berlin, 1978, pp. 65 and 266-273.

[27] M. Danaie and D. Mitlin, J. Alloys and Compounds, 476, 590 (2009).

[28] B. S. Amirkhiz, M. Danaie, and D. Mitlin, Nanotechnology 20, 204016 (2009).

4 Bimetallic Fe-V Catalyzed Magnesium Films Exhibiting Rapid and Cycleable Hydrogenation at 200˚C

Material in this chapter has been published in:

Beniamin Zahiri, Babak Shalchi Amirkhiz, Mohsen Danaie, and David Mitlin, Appl. Phys. Lett. 96, 013108 (2010)

4.1 Introduction

Numerous approaches are being utilized to both promote enhanced hydrogen sorption kinetics in magnesium and to understand their fundamental origins, e.g. [1-7]. Researchers have reported significantly accelerated kinetics in binary Mg-Fe [8-10] and Mg-V [11-13] systems relative to other Mg-based alloys. Mg-V powder composites display some of the fastest hydrogen sorption kinetics of any magnesium-based system [14], the ternary Mg-Fe-V system, be it in bulk or thin film form, has received little attention.

4.2 Experimental

The geometry of the samples was a 1.5 μm Mg-Fe-V films with a 7.5 nm Pd /7.5 nm Ta bilayer catalyst on both top and the bottom surfaces. When using a single layer Pd catalyst thermal effects drive the interdiffusion of Mg and Pd, and the subsequent formation of Mg6Pd and MgO[15,16]. In this study tantalum is chosen as the intermediate layer because it has been demonstrated to be effective in preventing elevated temperature interdiffusion of Pd and the underlying Mg during hydrogen sorption [17,18]. The deposition rates were the following: Mg 3; Pd 1.7; Ta 0.3 Å/sec; Fe and V varied to adjust

for stoichiometry. Volumetric absorption and desorption measurements were done at 200 ˚C. Absorption was performed at a hydrogen pressure of 2.7-2.5 bar, while de-sorption was done in the 0.01-0.02 bar range. Samples received over 105 absorption/desorption cycles. The system automatically switched from absorption to desorption (and vice versa) once the rate fell below 0.004 wt %/min. Additional experimental information is provided in Ref. 3.

4.3 Results and Discussion

At 200 ˚C the cycling sorption behavior of Mg-20 at. % Fe is quite poor (data not shown). During the first hydrogenation the alloy is able to sorb over 4 wt % hydrogen in less than 10 min. The first desorption is however fairly slow, requiring over an hour to release 2.5 wt % hydrogen. After cycle 2 the capacity of the system degraded. Testing was concluded after hydrogenation cycle 4. Figures 4.1(a) and 1(b) indicate that in the binary Mg-V and in all ternary Mg-Fe-V alloys the situation is quite different: First there is an activation period where the absorption kinetics are significantly slower (order of magnitude) than at steady state. During desorption an activation period also exists but represents only a moderate slowdown (factor of 2) relative to the long-term cycling kinetics. This activation period may be due to a variety of microstructural factors such as the time-dependent decomposition of the initially Fe and (or) V supersaturated Mg into the equilibrium nearly pure Mg phase and Fe-V (or V). It may also be due to cycling-induced microcracking of the films and the creation of new surfaces.

By cycle 5 both the absorption and the desorption kinetics are stabilized. For these alloys the absorption kinetics are extremely rapid being on the order of 10 s to reach full hydrogen capacity. The desorption kinetics are also relatively fast; ranging from 15 min for the Mg-10 at. % Fe-10 V alloy to 25 min for Mg-15 at. % Fe-15 V. Interestingly, these absorption curves do not have the sigmoidal shape characteristic of slow nucleation (nucleation-limited) reactions [19]. Such sigmoidal shapes are normally observed for

hydrogentation of magnesium. Rather the slope consistently decreases with increasing time. This has been attributed to a hydride formation process that proceeds evenly on the entire surface of the reactant phase [19]. The hydrogen desorption curves similarly possess decreasing slopes with increasing amount of transformed phase (time). The kinetics of Mg-Fe-V and Mg-V alloys may be qualitatively compared to what was measured in pure Mg films [20]. The pure Mg samples had identical preparation, identical dimensions and identical bilayer Pd-Ta catalysts. They were tested at 250 ˚C with absorption (desorption) pressures of 2.5 and 0.05 bar, respectively. The postactivation period times to absorb (desorb) were on the order of 40 min and 2 h.

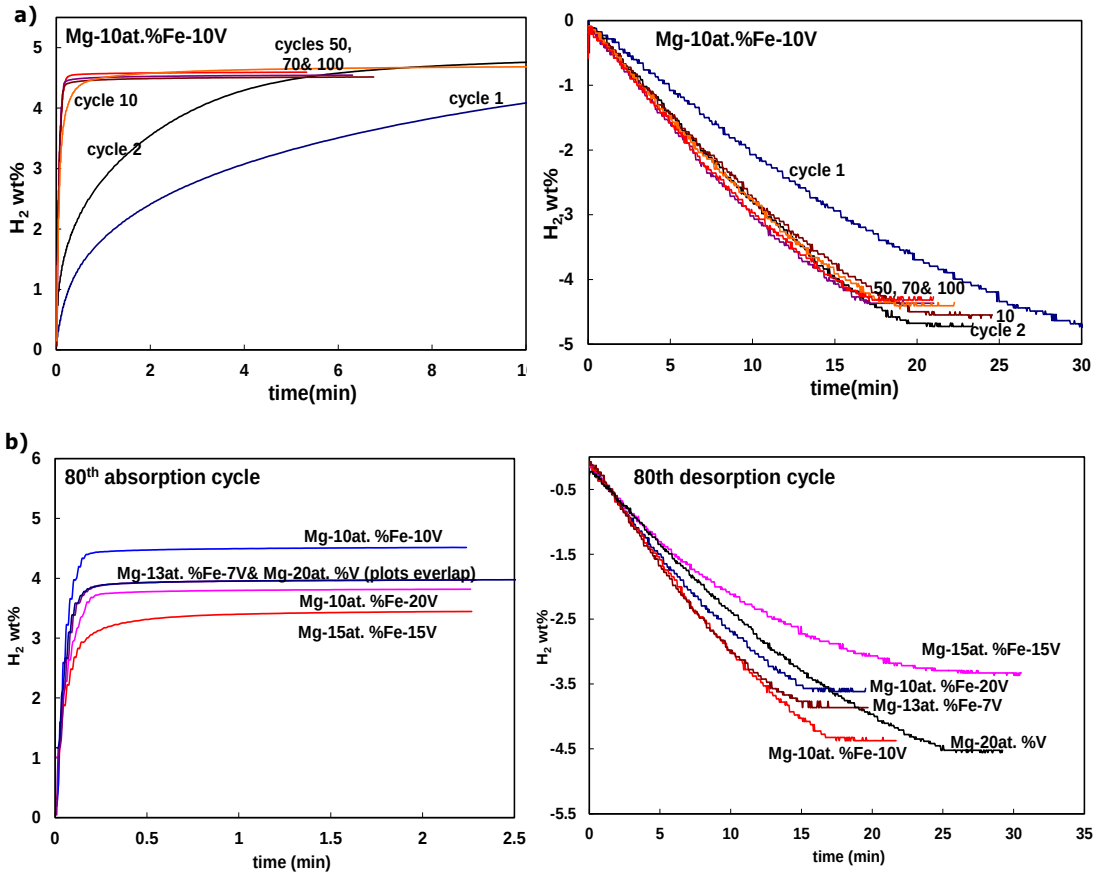

Figure 4.1: (a) Sorption curves for Mg-10 at. % Fe-10 at. % V, over cycles 1-100 (left is absorption, right is desorption). (b) Absorption and desorption cycle 80 for the ternary alloys and for Mg-V.

Another key characteristic of these alloys is that after the initial activation period the samples did not display any capacity degradation during subsequent testing. The capacities shown at cycle 80 were identical to the capacities at cycle 6 and at cycle 100. The measured hydrogen capacities of the alloys are somewhat lower than what would be expected with complete conversion of magnesium to a-MgH_2 and no other hydride phase being present. Assuming only a-MgH_2, alloys Mg-20 at. % V, Mg-10 at. % Fe-10 V, Mg-13 at. % Fe-7 V, Mg-10 at. % Fe-20 V, and Mg-15 at. % Fe-15 V can hold 5.12, 5.04, 5.02, 4.09, and 4.07 wt %, respectively. The bilayer catalysts coating both sides of the films add negligible hydrogen storage capacity but have a non-negligible weight. This would lower the above capacities by approximately 10%.

Figure 4.2 compares the Mg-Fe-V and the Mg-V alloys, showing the time to absorb (left) and the time to desorb (right) 80 wt % of the measured hydrogen capacity. The absorption data highlights the activation period present for all alloys during the initial cycles. More importantly it highlights a key difference in the hydrogenation behavior between the binary Mg-V alloy and the ternary Mg-Fe-V: Starting at about 40 sorption cycles the kinetics of Mg-20 at. % V begin to display some degradation. Conversely the absorption kinetics of the Mg-Fe-V alloys remain constant over the 100 cycles of testing. The desorption data in general shows more experimental scatter making a clear interpretation of the trends more diffricult. The kinetics are also markedly slower than for absorption, though still very fast relative to other Mg-based systems [14]. In Mg-20 at. % V there does seem to be a trend of prolonged (80+) cycling leading to some degradation of the desorption kinetics. The Mg-10 at. % Fe-20 V may degrade analogously to the Mg-20 at. % V alloy. In the remaining Mg-Fe-V alloys the data points to either very minor kinetic degradation or to none at all.

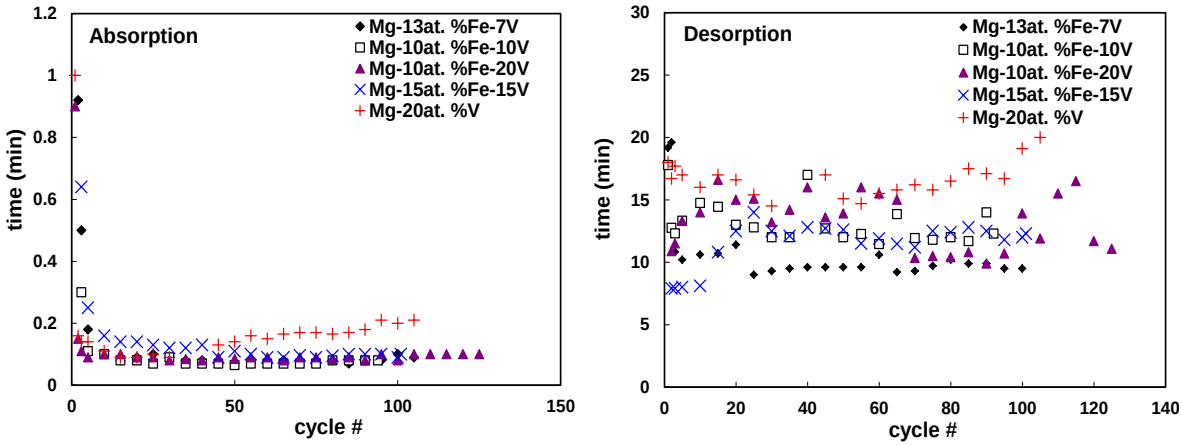

Figure 4.2: A comparison of the time to sorb 80 wt % of the maximum measured capacity, as a function of sorption cycle number.

Pressure-composition isotherm absorption and desorption data for Mg-15 at. % Fe-15 V was obtained at 200, 230, and 260 ˚C (not shown due to space constraints). As expected there is a quantifiable hysteresis between the hydride formation plateau and the hydride decomposition plateau. The calculated enthalpy for hydride formation is -71 kJ/mol H_2 while the enthalpy for hydride decomposition is 73 kJ/ mol H_2. The calculated entropy is in the 130 J/Kmol H_2 range. From these results we can conclude that Fe-V does not alter the system thermodynamics and the sorption enhancement is purely kinetic. While the enthalpy of hydride formation for any Fe-V phases are unknown, it can be safely assumed that the value will be somewhere between that of pure V and of pure Fe. $VH_{0.5}$ has an enthalpy of formation in the range of -35 to -42 kJ/mol H, while iron hydrides are unstable (ΔH $FeH_{0.5}$ is +10 kJ/mol H) [19]. At 200 ˚C and 2.7 bar a stable Fe-V hydride is not expected. Another possibility is the formation of the Mg_2FeH_6 phase, which has a similar enthalpy of formation to α-MgH_2. As the next figure will demonstrate, there is little evidence for Mg_2FeH_6 formation.

Figure 4.3 shows the indexed XRD pattern of the hydrogentated and desorbed Mg-10 at. % Fe-10 V films. The samples, which were in loose flake form, were analyzed after

undergoing over 100 sorption cycles. Hence the microstructure may be considered as "steady-state." The most prominent peaks are unambiguously indexed to belong to a-MgH_2 phase, with no detectable variation of the lattice parameter from the literature-reported values. A simulation was run to predict the peaks belonging to Mg_2FeH_6, with the results clearly showing it not being present. We also simulated the equilibrium tetragonal σ-FeV phase, which was unambiguously absent.

The hump may be caused by an amorphous phase (being peaked at the average near-neighbor distance), a nanocrystalline phase or a mixture of both. The peak is more prominent in the desorbed sample, being centered at roughly $2\theta = 42.7^\circ$. The most intense peak for pure α-Fe would be (011) centered at $2\theta = 44.7^\circ$. The most intense peak for pure V is (011) centered at $2\theta = 42.3^\circ$. The metastable CsCl-type Fe-V phase has its most intense (011) peak centered at $2\theta = 43.8^\circ$, though the lattice spacing and hence position is expected to vary with the relative composition. The (001) CsCl-type Fe-V peak centered at $2\theta = 30.5^\circ$ is much weaker and is not expected to show up in the pattern. Thus there is a good possibility that the Fe and V atoms, which possessing a negative enthalpy of mixing but are negligibly soluble in Mg, are clustered into a nanocrystalline CsCl-type phase. We plan to use cryo-stage TEM analysis [21,22] to explore the Fe-V phase distribution within the films in order to confirm or negate this hypothesis.

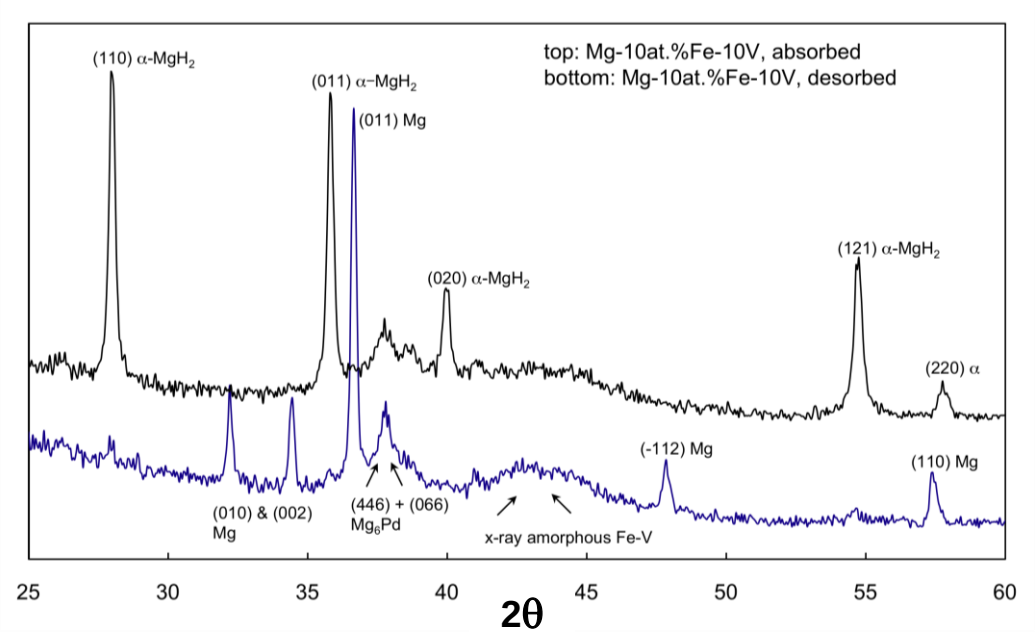

Figure 4.3: (Color online) Indexed x-ray diffraction pattern of Mg-10 at. %Fe-10 V alloy after cycling, sorbed and desorbed.

From a kinetic point of view, V and Fe are known to be individually catalytic for hydrogen dissociation/reassociation. Combining these elements in a nanocrystalline structure may be synergistic. Moreover if this Fe-V phase is densely and continuously dispersed throughout the Mg(MgH_2) grains, it may act as an effective pathway for hydrogen diffusion in and out of the microstructure. It should also act as a heterogeneous nucleation site for both magnesium hydride and for metallic magnesium. That would explain the observed non-sigmoidal shape of the absorption and desorption curves, since copious nucleation events would occur. One can also argue that since elemental Fe and V have a negative heat of mixing with correspondingly reduced diffusivities, a phase consisting of both elements should be more resistant to microstructural coarsening relative to pure V or Fe phases. This may explain the unique prolonged cyclic stability of the ternary system.

Acknowledgement: This work was supported by NINT NRC and NSERC Discovery.

4.4 References

[1] M. Rogers, S. Barcelo, X.B. Chen, T.J. Richardson, V. Berube, G. Chen, M.S. Dresselhaus, C.P. Grigoropoulos, S.S. Mao, Appl. Phys. A., 96, 349 (2009).

[2] A. Baldi, V. Palmisano, M. Gonzalez-Silveira, Y. Pivak, M. Slaman, H. Schreuders, B. Dam, and R. Griessen, Appl. Phys. Lett. 95, 071903 (2009).

[3] B. Zahiri, C.T. Harrower, B.S. Amirkhiz, and D. Mitlin, Appl. Phys. Lett. 95, 103114 (2009).

[4] M. Ramzan, T. Hussain, and R. Ahuja, Appl. Phys. Lett. 94, 221910 (2009).

[5] A. Kale, N. Bazzanella, R. Checchetto, and A. Miotello, Appl. Phys. Lett. 94, 204103 (2009).

[6] S.Q. Hao and D.S. Sholl, Appl. Phys. Lett. 94, 171909 (2009).

[7] A. Borgschulte, J.H. Rector, H. Schreuders, B. Dam and R. Griessen, Appl. Phys. Lett. 90, 071912 (2007).

[8] P. Selvam and K. Yvon K., Int. J. Hydrogen Energy, 16, 615 (1991).

[9] B. Bogdanovic, A. Reiser, K. Schlichte, B. Spliethoff and B. Tesche, J. Alloys Compd., 345, 77 (2002).

[10] J. Huot, H. Hayakawa and E. Akiba, J. Alloy. Compd. 248, 164 (1997).

[11] G. Liang, J. Huot, S. Boily, A. Van Neste and R. Schulz, J. Alloy Compd. 291, 295 (1999).

[12] Z. Dehouche, J. Goyette, T.K. Bose, J. Huot, R. Schulz, Nano Letters, 1, 175 (2001).

[13] J. Huot, J.F. Pelletier, G. Liang, M. Sutton, R. Schulz, J. Alloy Compd. 330, 727 (2002).

[14] B. Sakintuna, F. Lamari-Darkrim and M. Hirscher, Int. J. Hyd. Energy, 32, 1121 (2007).

[15] E. Johansson, C. Chacon, C. Zlotea, Y. Andersson, and Bjorgvin Hjorvarsson, J. Phys.: Condens. Matter 16 7649 (2004).

[16] J.L.Slack, J.C.W. Locke, S.W. Song, J. Ona and T.J. Richardson, Solar Energy Materials and Solar Cells 90, 485 (2006).

[17] H. Fritzsche, C. Ophus, C. T. Harrower, E. Luber, and D. Mitlin, App. Phys. Lett., 94, 241901 (2009).

[18] H. Fritzsche, M. Saoudi, J. Haagsma, C. Ophus, E. Luber, C.T. Harrower and D. Mitlin, Appl. Phys. Lett. 92, 121917 (2008).

[19] N. Gerard and S. Ono, Hydrogen in Intermetallics II (Topics in Applied Physics), edited by L. Schlapbach, Springer-Verlag, Berlin, 1988, pp. 165-193.

[20] X. Tan, C.T. Harrower, B.S. Amirkhiz and D. Mitlin, Int. J. Hydrogen Energy, 34, 7741 (2009).

[21] M. Danaie and D. Mitlin, J. Alloys Compd. 476, 590 (2009).

[22] B. S. Amirkhiz, M. Danaie, and D. Mitlin, Nanotechnology 20, 204016 (2009).

5 Hydrogen storage cycling of MgH_2 thin film nanocomposites catalyzed by bimetallic Cr Ti

Material in this chapter has been published in:

Beniamin Zahiri, Babak Shalchi Amirkhiz, and David Mitlin, Appl. Phys. Lett. 97, 083106 (2010)

5.1 Intorduction

Mg-based thin films can be employed as model system for designing and understanding bulk hydrogen storage materials [1-11]. Binary Mg-Ti and Mg-Cr films have been reported to possess fast sorption kinetics when tested electrochemically [8]. However little is known regarding the synergy of Cr-Ti catalyst additions.

5.2 Experimental

The geometry of the samples was a 1.5 μm thick Mg-Ti-Cr film, capped with a 7.5 nm Pd /7.5 nm Ta bilayer on both the top and the bottom surface[12,13]. Hydrogen was absorbed at a starting pressure of 3 bar (finishing at 1.5 bar) and desorbed at a starting pressure of 5 mbar (finishing at 15-20 mbar). The system automatically switched from absorption to desorption, and vice versa, once the sorption rate fell below 0.004 wt %/min. Transmission electron microscopy (TEM) analysis was performed using the JEOL 2200FS microscope, operating at 200 kV accelerating voltage. After prolonged hydrogen cycling the samples resembled loose powder that could be analyzed directly without additional thinning. More detail on the synthesis, testing and analysis methodology is presented in Ref. 5.

5.3 Results and Discussion

Figures 5.1(a)-(c) show the absorption and desorption behavior for the Mg-Cr and Mg-Cr-Ti, tested at 200 ˚C. The initial absorption behavior of the binary Mg-Cr film is relatively fast, being on the order of seconds. However the hydrogen gravimetric capacity does show signifcant degradation, dropping from approximately 5.5 wt % at cycle 1 to below 4 wt % by cycle 91. Desorption kinetics are both much slower and show more degradation with increasing cycling. At cycle 1, it took 10 min to desorb, while by cycle 100 desorption took an hour. Sorption results for binary Mg-Ti, previously tested at analogous geometries and sorption conditions, show that the hydrogen capacity of this alloy rapidly degrades due to the irreversible formation of TiH_2.

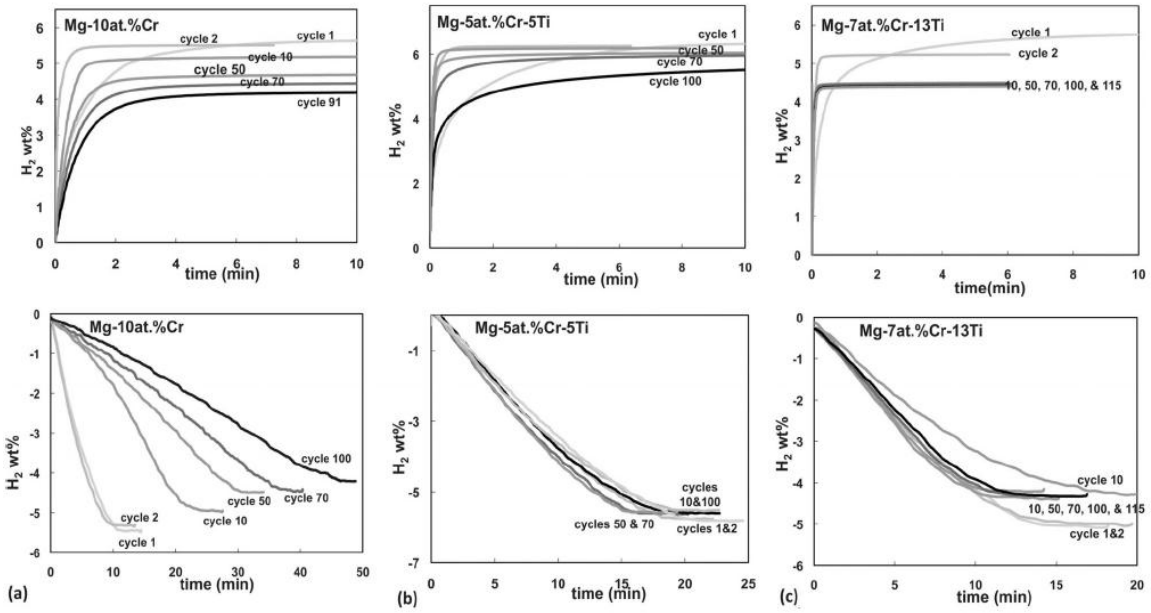

Figure 5.1: Absorption and desorption behavior of binary Mg-Cr and Mg-Cr-Ti at 200 ˚C. (a) Sorption curves for Mg-10 at. % Cr over cycles 1-100. (b) Sorption curves for Mg-5 at. % Cr-5Ti, over cycles 1-100 (top is absorption, bottom is desorption). (c) Sorption curves for Mg-7 at. % Cr-13Ti, over cycles1-115.

The Mg-Cr-Ti, with comparable levels of secondary additions in terms of atomic percent, display much more rapid and stable desorption kinetics. Figure 5.1(b) illustrates this for the Mg-5at. % Cr-5Ti alloy. The absorption kinetics is comparable to that of the binary Mg-Cr alloy. However, the de-sorption kinetics are markedly different, with little degradation occurring even by cycle 100. Here it consistently takes 15-20 min to achieve desorption. With increasing Cr-Ti additions, the hydrogen capacity is expectedly reduced. However, the sorption kinetics is improved even further. Even at cycle 115, Mg-7 at. % Cr-13Ti takes only several seconds to absorb, and approximately 10 min to desorb.

Figure 5.2 compares the Mg-Cr-Ti and the Mg-Cr alloys, showing the time to absorb and the time to desorb 80% of the mean maximum hydrogen gravimetric capacity for each composition. These results highlight two fundamentally attractive features of the Mg-Cr-Ti system: First, the higher alloy content (systems with above 5 at. % of each element) show either none or very minor kinetic degradation throughout the sorption cycling. Even the alloy Mg-13 at. % Cr-7Ti, which seems to show some cycling degradation, still outperforms the baseline Mg-Cr systems both in the absorption and even more so in the desorption times. Second, and equally importantly, these systems display only a very minor "activation" period during the first several cycles. An activation period is usually the norm for Mg-based systems, with the first several absorption/desorption cycles being orders of magnitude slower than the subsequent ones.

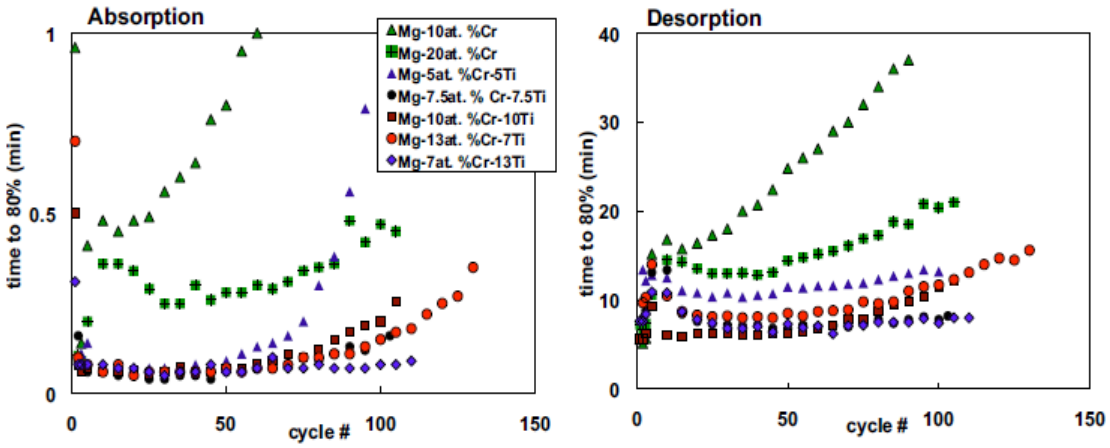

Figure 5.2: A comparison of the time to sorb 80% of the average maximum hydrogen gravimetric capacity for each composition, as a function of sorption cycle number.

Figure 5.3 shows the pressure-composition-isotherm plots for the Mg-7 at. % Cr-13Ti alloy. As expected there is a quantifiable hysteresis between the hydride formation plateau and the hydride decomposition plateau. The calculated enthalpy for hydride formation is -73 kJ/mol H_2 while the enthalpy for hydride decomposition is 79 kJ/mol H_2. These enthalpies agree with the well-known formation/ decomposition ΔH values for α-MgH_2. From these results we can conclude that Cr-Ti does not alter the $Mg(MgH_2)$ thermodynamics and the sorption enhancement is purely kinetic. The entropy for hydride formation and decomposition is -134 and 144 J/K mol H_2, respectively, though more data points would be desirable to increase the accuracy of this calculation.

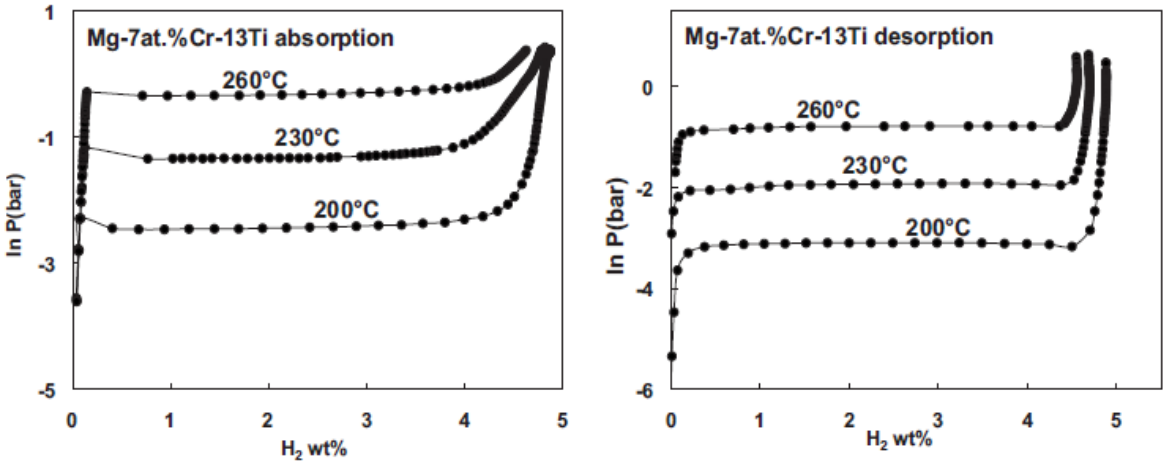

Figure 5.3: Pressure-composition isotherms from absorption and desorption data for Mg-7 at. % Cr-13Ti.

Figure 5.4(a) shows indexed X-ray diffraction patterns of Mg-Cr-Ti films, in the absorbed state. The samples, which were in loose flake form, were analyzed after undergoing over 100 sorption cycles. The most prominent peaks are unambiguously indexed to belong to α-MgH_2 phase, with no detectable variation of the lattice parameter from the literature-reported values. A simulation was run to predict the peaks belonging to the various equilibrium phases of Cr-Ti intermetallics reported in literature [14,15]. The results clearly showed those structures not being present. We also simulated the equilibrium α-$TiCr_2$, α-Cr, α-Ti phases, and β-Ti, all of which were unambiguously absent. We did not detect the three strongest TiH_2 peaks (111) at 20=34.9˚, (002) at 20 =40.6˚, and (022) at 58.7˚. However the first two peaks would be quite near the α-MgH_2 peaks, making the two experimental patterns diffcult to separate. Thus we are leaving the presence of a minor amount of TiH_2 as a possibility. Neither CrH, with a ΔH of -6 kJ/mol, nor $CrH_{0.5}$ with ΔH of -4 kJ/mol would be present at these testing conditions. We were able to confirm the presence of the Mg_6Pd intermetallic, with its more intense peaks being relatively prominent. There is limited evidence of an "amorphous X-ray hump" being

present at 2θ=42˚-43˚, in particular for the Mg-7Cr-13Ti sample. However even in that composition, the hump's intensity is not far from that of the background.

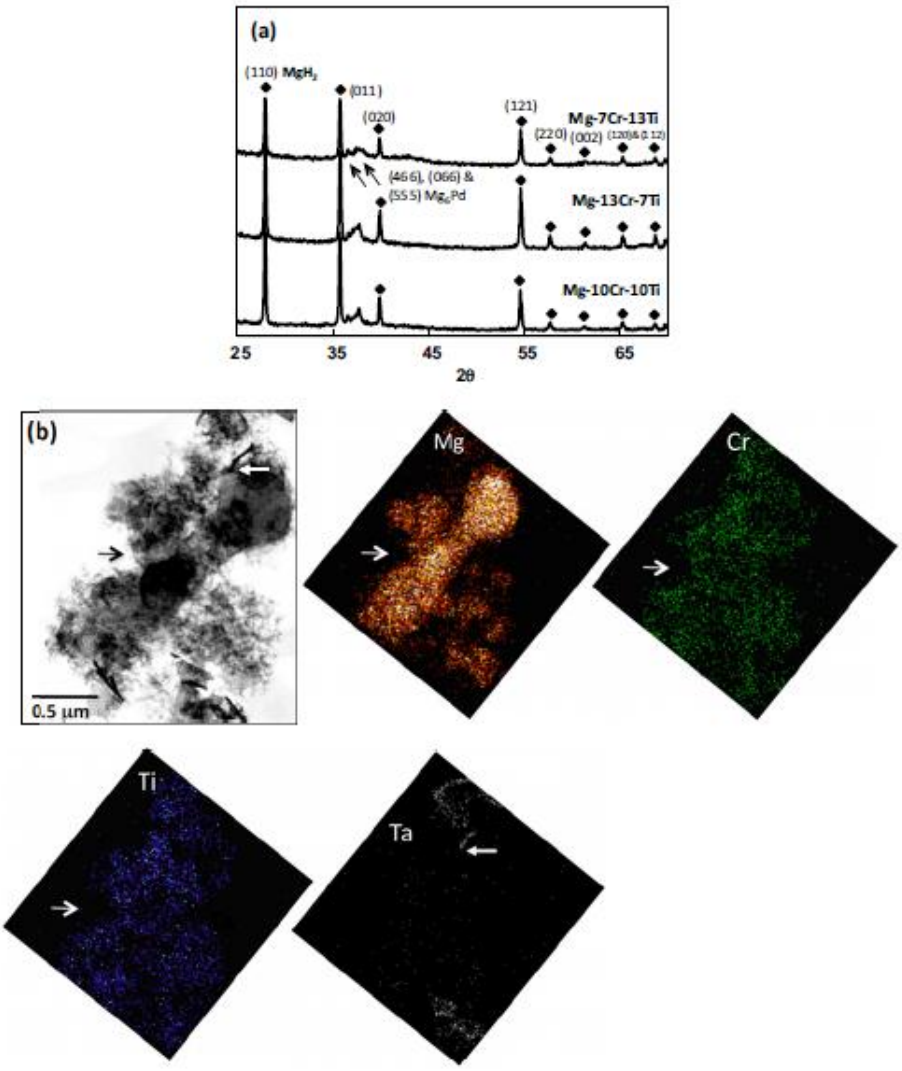

Figure 5.4: (Color online) (a) Indexed X-ray diffraction pattern of the postcycled Mg-Cr-Ti alloys in the absorbed state. (b) Bright field STEM micrograph and EDXS elemental maps of Mg, Cr, Ti, and Ta in the Mg-10 at. % Cr-10 at. %Ti postcycled (absorbed) samples. An arrow points to the same region in the micrographs, an asterisk marks a Ta flake.

Scanning transmission electron microscopy/energydispersive X-ray spectroscopy (STEM/EDXS) mode TEM analysis was used to examine the postcycled Mg-10 at. % Cr-

10 at. %Ti samples in their absorbed state. This is shown in Fig. 5.4(b), which confirms that Cr and Ti are densely distributed throughout the microstructure even after 100 sorption cycles. The remnant Ta surface cap, marked by a secondary arrow, is easily resolved from the underlying MgH_2. Relatively large chunks of Mg_6Pd were also present, but are not shown in this image. The Cr and Ti, whose signals are far above the background noise in the EDXS spectrum, appear to be continuously distributed throughout the MgH_2 matrix. This is most likely due to a nanoscale second phase distribution that is below the spatial resolution limit of this microscope. It is highly unlikely that either element is in solid solution of α-MgH_2.

It is generally recognized that for enhancing hydride sorption kinetics a secondary phase must of course be catalytic toward hydrogen dissociation, must allow for hydrogen diffusion through it, and must be microstructurally stable during sorption cycling. However the secondary phase's role as a heterogeneous nucleation site is often neglected. Because of the signifcant volume and chemical interfacial energy mismatch between hexagonal close-packed metallic magnesium and rutile-type α-MgH_2, there is a large nucleation barrier for bulk formation of either one in the other. This is another fundamental kinetic impediment, which manifests as relatively large but sparsely spaced nucleated grains observed during partial sorption,[16] and the acceleration of sorption kinetics by the introduction of other heterogeneous nucleation sites such as dislocations [17]. Nanodispersed Cr-Ti should serve as an ideal heterogeneous nucleation template. With many more nucleation sites available, the diffusion distances are subsequently reduced and so are the times for full absorption/desorption.

5.4 References

[1] D. M. Borsa, R. Gremaud, A. Baldi, H. Schreuders, J. H. Rector, B. Kooi, P. Vermeulen, P. H. L. Notten, B. Dam, and R. Griessen, Phys. Rev. B 75, 205408 (2007).

[2] M. Rogers, S. Barcelo, X. B. Chen, T. J. Richardson, V. Berube, G. Chen, M. S. Dresselhaus, C. P. Grigoropoulos, and S. S. Mao, Appl. Phys. A: Mater. Sci. Process. 96, 349 (2009).

[3] B. Zahiri, C. T. Harrower, B. S. Amirkhiz, and D. Mitlin, Appl. Phys. Lett. 95, 103114 (2009).

[4] W. P. Kalisvaart, C. T. Harrower, J. Haagsma, B. Zahiri, E. J. Luber, C. Ophus, E. Poirier, H. Fritzsche, and D. Mitlin, Int. J. Hydrogen Energy 35, 2091 (2010).

[5] B. Zahiri, B. S. Amirkhiz, M. Danaie, and D. Mitlin, Appl. Phys. Lett. 96, 013108 (2010).

[6] A. Baldi, V. Palmisano, M. Gonzalez-Silveira, Y. Pivak, M. Slaman, H. Schreuders, B. Dam, and R. Griessen, Appl. Phys. Lett. 95, 071903 (2009).

[7] X.-H. Tan, C. T. Harrower, B. S. Amirkhiz, and D. Mitlin, Int. J. Hydro¬gen Energy 34, 7741 (2009).

[8] R. A. H. Niessen and P. H. L. Notten, Electrochem. Solid-State Lett. 8, A534 (2005).

[9] G. Liang, J. Huot, S. Boily, A. Van Neste, and R. Schulz, J. Alloys Compd. 292, 247 (1999).

[10] B. S. Amirkhiz, M. Danaie, and D. Mitlin, Nanotechnology 20, 204016 (2009).

[11] B. S. Amirkhiz, M. Danaie, M. Barnes, B. Simard, and D. Mitlin, J. Phys. Chem. C 114,3265 (2010).

[12] H. Fritzsche, C. Ophus, C. T. Harrower, E. Luber, and D. Mitlin, Appl. Phys. Lett. 94, 241901 (2009).

[13] H. Fritzsche, M. Saoudi, J. Haagsma, C. Ophus, E. Luber, C. T. Harrower, and D. Mitlin, Appl. Phys. Lett. 92, 121917 (2008).

[14] M. Bououdina, H. Enoki, and E. Akiba, J. Alloys Compd. 281,290 (1998).

[15] D. S. dos Santos, M. Bououdina, and D. Fruchart, J. Alloys Compd. 340, 101 (2002).

[16] M. Danaie, S. X. Tao, P. Kalisvaart, and D. Mitlin, Acta Mater. 58, 3162 (2010).

[17] M. Danaie and D. Mitlin, J. Alloys Compd. 476, 590 (2009).

6 Stable Hydrogen Storage Cycling in Magnesium Hydride, in the Range of Room Temperature to 300˚C, Achieved Using a New Bimetallic Cr-V Nanoscale Catalyst

Material in this chapter has been published in:

Beniamin Zahiri, Mohsen Danaie, XuHai Tan, Babak Shalchi Amirkhiz, Gianluigi Botton, and David Mitlin, J. Phys. Chem. C 116(4), 3188-3199 (2012)

6.1 Introduction

Hydrogen storage for fuel-cell based power generation is an active area of research. Because of its high gravimetric capacity of 7.6 wt.% and low cost, magnesium hydride (MgH_2) has attracted significant attention as a potential solid-state storage medium. While being less attractive for automotive applications because of its high thermodynamic stability (ΔH^0 MgH_2 formation ~ -77 kJ/mol), MgH_2 is a candidate for stationary backup power sources where the absorption heat management concerns and desorption temperatures are less stringent. Magnesium-based alloys, in powder and thin film form, also attract interest for model studies of hydrogen in metals, optical hydrogen sensing, switchable mirrors and solar absorber applications, e.g. [1-13].

To improve the sorption cycling kinetics of magnesium, transition metals are often used as catalyst additions. Researchers have reported significantly accelerated kinetics in binary Mg-V systems relative to other Mg-based alloys [14,15]. In fact, these Mg-V powder composites displayed some of the fastest hydrogen sorption kinetics of any magnesium-based system. The most commonly reported form of vanadium hydride is $VH_{0.5}$. The

reported enthalpy of formation for this hydride ranges from -70 to -83 kJ/mol H_2 [16,17]. Thus, the formation of $VH_{0.5}$ hydride is expected at temperatures/pressures conditions utilized for magnesium. The formation of hydrides with higher concentrations of hydrogen, e.g. $VH_{0.9}$ has also been reported by X-ray measurements [18]. The presence of $VH_{0.81}$ phase in the V-catalyzed magnesium powders has also been reported based on the X-ray analysis [14]. However as the plateau pressure - composition - temperature (PCT) data showed, the thermodynamics of MgH_2 formation was not altered by the presence of vanadium hydride.

While the sorption behavior and structure of Mg-V system has been widely investigated, Mg-Cr has received much less attention. Similar to other transition metals, Cr is expected to improve the sorption behavior of Mg by lowering the dissociation energy barrier of hydrogen molecules. This has been proved by theoretical calculations on transition metal-doped Mg surfaces [19]. CrH possesses an enthalpy of formation as low as -6 kJ/mol H [20], and is not stable at elevated temperatures under usual testing pressures. The electrochemical sorption behavior of Mg-Cr thin film has also shown an improved kinetics as compared to pure Mg with a reversible capacity of 4.9 wt. % for Mg-20Cr [21]. However the known relatively slow absorption cycling performance of this binary system along with the theoretical calculations suggest that other alloying elements must be added to gain better catalytic performance [22,23].

While the kinetic performance of binary Mg-based alloys is clearly improved with respect to pure Mg, even faster sorption rates combined with retained kinetic stability throughout prolonged cycling would be highly desirable. Generally, for a material to act as catalyst and maintain its catalytic activity throughout hydrogen sorption cycling the initially nanodispersed catalyst must be stable against coarsening and agglomeration. However even at temperatures as low as 200 ˚C, it has been found that the catalyst coarsening accompanied by kinetics degradation occurred over extended sorption cycles [22,24]. It has been shown that combining two or more transition metals would promote cycling stability presumably due to improved coarsening resistance of the alloy catalyst [24-28]. Improved catalytic performance would therefore be expected from the Cr-V

bimetallic catalyst. A recent neutron reflectometry study performed by our group on 50nm thick Mg-Cr-V alloy films indeed pointed to markedly improved kinetics and a fundamentally different hydride growth geometric front compared to the baseline Pd-catalyzed Mg films [29]. To our knowledge this is the only existing hydrogen sorption study on this promising ternary system. In the case of the alloy film, at room temperature the formation of hydride phase occurred uniformly throughout the film, rather than at the film-gas interface. Though these results were intriguing, it's not known whether similar behavior would be observed in materials with much larger geometries and hence longer diffusion distances. Furthermore due to the nature of neutron reflectometry analysis the microstructural observations were both indirect and non-site specific in the plane of the film.

This study has two primary goals: We tested a number of ternary Mg-Cr-V compositions, in the form of 1.5 μm thick alloy films, at temperatures ranging from ambient to 300˚C, and observed remarkable kinetics. Thus our first goal was to explain the microstructural origin of this performance by employing detailed site-specific transmission electron microscopy (TEM) analysis of the sorbed and partially sorbed microstructures. Our second goal was to correlate these microstructural factors to the calculated activation energies and hence hypothesize about the rate limiting steps. In the process of doing this through the well-established Johnson Mehl Avrami (JMA) analysis we found that the activation energy for hydrogenation actually varied with the driving force. Though this result is not entirely unexpected, it has been largely overlooked in literature and serves to explain the frustrating lack of correlation in the reported activation energies from various studies.

6.2 Experimental

6.2.1 Synthesis and analysis methods

We synthesized the Mg-Cr-V alloys through physical vapor co-deposition (magnetron sputtering). The as-synthesized films were 4 inches in diameter with a thickness of 1.5 micrometers. This minimum dimension was in fact much larger than what is typically used for "bulk" powder studies, where for example the particle diameters are in the 200-300 nanometer range [28]. Thin films were magnetron co-sputtered deposited (AJA International Inc. ATC ORION 5) onto a 4 inch Si (100) substrate that was coated with a hardened (so as not to outgas in the chamber) photoresist at room temperature. We used Ar gas with a purity of grade 5 at a sputtering pressure of $5x10^{-3}$ mbar, with a maximum base pressure of $5x10^{-8}$ mbar.

Depositions were done in a sputter-up configuration with continuous substrate rotation. Film thickness and deposition rates were obtained through the use of crystal deposition rate monitor held at the substrate plane. A Pd surface cap was coated onto both sides of the as-synthesized film so as to prevent the oxidation of the magnesium surfaces. A nano-scale layer of Ta was utilized as an intermediate between the Mg-Cr-V and the Pd. This was done because Ta was demonstrated to be effective in reducing the rate of elevated temperature Mg-Pd intermetallic formation during the initial hydrogen absorption step [30,31]. Inside the sputter system the thin films stack had following geometry: vacuum/ 7.5 nm Pd/ 7.5 nm Ta/ 1.5 μm Mg-Cr-V/ 7.5 nm Ta/ 7.5 nm Pd/ photoresist/ Si wafer. The deposition rates were the following: Mg 0.3; Pd 0.17; Ta 0.03 nm/sec; Cr and V varied to adjust for different film stoichiometries. The films had compositions (all in atomic percent) Mg-5Cr-5V, Mg-7.5Cr-7.5V, Mg-10Cr-10V, Mg-7Cr-13V, and Mg-13Cr-7V, Mg-10V, Mg-20V. Depositions of the catalysts and of the bulk Mg were performed sequentially without any interruption. After deposition the photoresist was washed away using acetone allowing the films to be fully released from the Si wafer.

Release from the substrate allowed the films to be treated as free flakes several tens to about one hundred micrometers in diameter each.

Volumetric absorption and desorption measurements were performed using a Sieverts hydrogen sorption analysis system (Hy-Energy LLC. PCTPro 2000). The cycling measurements were carried out at 25, 200 and 300˚C. Hydrogen was absorbed at a starting pressure of 3 and 4.5 bar during 200 and 300˚C cycling, respectively. For desorption, the samples were put under 15 mbar at 200˚C and 1 bar 300 ˚C. The system automatically switched from absorption to desorption, and vice versa, once the sorption rate fell below 0.004 wt. %/min. Room temperature absorption was performed on samples that first underwent 50 absorption/desorption cycles at 200˚C. This "activated" the samples, achieving the steady state microstructure required for fast kinetics. After the 50^{th} desorption, the sample was cooled down to room temperature and absorbed at different pressures in the range of 2-5 bar. After each absorption step the sample was heated up to 200˚C as to be able to desorb under 10-15 mbar.

A partially absorbed sample was prepared for the purpose of microstructural analysis during the absorption reaction. A sample was firstly cycled 150 times at 200˚C / 3 bar. The absorption pressure and temperature were then reduced to 1.5 bar and 185˚C. This temperature-pressure combination resulted in a similar driving force (i.e. deviation from the equilibrium partial pressure plateau). However the reduced temperature lowered the absorption kinetics sufficiently as so to allow for controlled process interruption. After reaching about 70% (by weight) of the reacted fraction, the sample was quenched down to room temperature. For the JMA kinetics analysis and the activation energy measurements, the samples were initially cycled for 50 cycles. The kinetics tests were then performed in the temperature range of 200-240˚C.

Conventional transmission electron microscopy (TEM) analysis was performed using the JEOL-JEM 2100 microscope, operating at 200 kV accelerating voltage. High

resolution TEM (HRTEM) analysis was performed on an FEI Titan 80-300 microscope equipped with an aberration corrector for the image-forming lens. The accelerating voltage was set at 300 kV and the spherical aberration coefficient was close to 1 μm during HRTEM experiments. After prolonged hydrogen cycling, the samples still resembled small flakes of thin films combined with agglomerated particles. Thus, additional thinning process was required to achieve electron transparency. This was performed via mortar and pestle grinding. The samples then were spread onto a copper grid that was supported by a thin layer amorphous carbon. TEM analysis of the MgH_2 was performed using a liquid nitrogen cooled cryo-stage so as to minimize beam damage and in-situ desorption during analysis [32].

X-ray diffraction (XRD) analysis was done using a Rigaku Ultima III X-ray diffractometer with Cu-K_α radiation source (λ=1.5406 Å). In order to determine the crystallite size of hydride phase, both integral breadth analysis (IBA) and Scherrer methods were utilized [33]. For the IBA, the following formula was used:

$$\frac{(\delta 2\theta)^2}{(\tan\theta_0)^2} = \frac{k\lambda}{D}\frac{\delta 2\theta}{\sin\theta_0 \tan\theta_0} + 16e^2 \qquad 6.1$$

Where $\delta 2\theta$ is the integral breadth of the peak in radians θ_0 is the position of the peak maximum. By plotting the $\frac{(\delta 2\theta)^2}{(tan\theta_0)^2}$ vs. $\frac{\delta 2\theta}{sin\theta_0 tan\theta_0}$, both values of crystallite size D and microstrain e can be determined. For the Scherrer method, the following equation was used.

$$D = \frac{k\lambda}{\beta cos\theta_0} \qquad 6.2$$

where β is the line broadening at half maximum intensity (FWHM) in radians. In both cases, the values for integral breadth and FWHM were corrected for instrumental effects using a LaB_6 standard obtained from NIST Standard Reference Materials®.

6.2.2 Kinetics measurements (theoretical background)

The well-known Johnson Mehl Avrami (JMA) model can be used to describe magnesium – magnesium hydride phase transformation kinetics [34,35]. The JMA model assumes the nucleation and growth occurs randomly in the bulk and at the surface. It also assumes that the sample volume is infinite and takes the impingement of growing grains into account. It has been shown that homogeneous and heterogeneous nucleation conditions could be well described by JMA model [35]. This model is also applied to transformations in which the growth rate is diffusion limited and interface controlled. This model is also valid in the cases of nucleation site saturation and constant nucleation rate with constant growth rates. The equation used in JMA model is as follows:

$$f = 1\text{-}\exp[-(kt)^n] \qquad 6.3$$

where k is the rate constant and n is a constant so-called Avrami exponent. The Avrami exponent is related to the dimensionality of the growth process and gives information about the rate-limiting step of the reaction. However, such information is not conclusive especially when n values are small, i.e. n<1.5 [35]. For example, $n = 1$ describes both a diffusion-limited reaction where particles grow along 1-D defects and also an interface controlled growth with grain boundary nucleation after saturation [35]. The Avrami exponent n can be expressed in the general form of $d/m + a$. Here d is the dimensionality of the growth ($d = 1$, 2 and 3) and m indicates interface-controlled ($m = 1$) or diffusion-limited ($m = 2$) growth. The constant a is related to nucleation rate where $a = 0$ for site saturation (constant number of nuclei), $0 < a < 1$ for decreasing nucleation rate, $a = 1$ for constant nucleation rate and $a > 1$ for increasing nucleation rate.

Generally, the rate constant k is a function of temperature and pressure. Thus, it can be written in the following form [36].

$$k = k(P) \times k(T) = k(P) \times k_0 \exp(-Q/RT) \quad (6.4)$$

where $k(P)$ is the pressure-dependent term. This term is also referred to as the driving force function. In the pressure-independent term $k(T)$, k_0 is the pre-exponential factor, Q is the overall activation energy and R is the gas constant. Therefore, to obtain the activation energy of the reaction, one should account for the influence of the pressure during the measurements. The selection of the driving force function is mostly depending on the rate-limiting step of the reaction. For the metal/hydride transformation, a thermodynamic driving force can be used [36]. This function is obtained directly from the chemical potential for a reaction at non-standard conditions ($\mu = \mu^0 + RT\ln Q$, where Q is the reaction quotient). At a constant temperature, this function has the following form for the case of absorption:

$$k(P) = ln(P/P_{eq}) \quad (6.5)$$

where, P_{eq} is the equilibrium hydrogen partial pressure for a given temperature.

Rudman showed that in a process where the diffusion is the rate-limiting step, another type of driving force expression could be employed [37]. In the derivation the thermodynamic terms and the diffusivity of the hydrogen atoms were taken into account. The following equation was introduced for the driving force of a diffusion-limited absorption reaction:

$$k(P) = 1 - (P_{eq}/P)^{0.5} \quad (6.6)$$

In the subsequent kinetic analysis, we will utilize both expressions and demonstrate that they provide similar trends in the activation energy values as a function of pressure.

6.3 Results

6.3.1 Hydrogen Sorption

A desorption pressure of 1 bar or higher is required for practical hydrogen storage applications. Based on the thermodynamics of Mg/MgH_2 transformation, a temperature of around 300 ˚C is needed to reach this plateau pressure. In view of this, we examined the cycling performance of Mg-Cr-V ternary system at this temperature. The cycling results of the Mg-7Cr-13V film at 300 ˚C are shown in Figures 6.1(a) and (b). The absorption behavior of this material shows negligible deterioration over 250 cycles, as indicated by Fig. 6.1(a). The time to reach 80% of the reaction completion increases from 10 to 25 seconds. The desorption kinetics (Fig. 6.1(b)) similarly show minimal degradation, with desorption times being in the range of 25 seconds over the 250 cycles. Other alloy compositions displayed a similar cycling behavior, with very low levels of kinetics degradation.

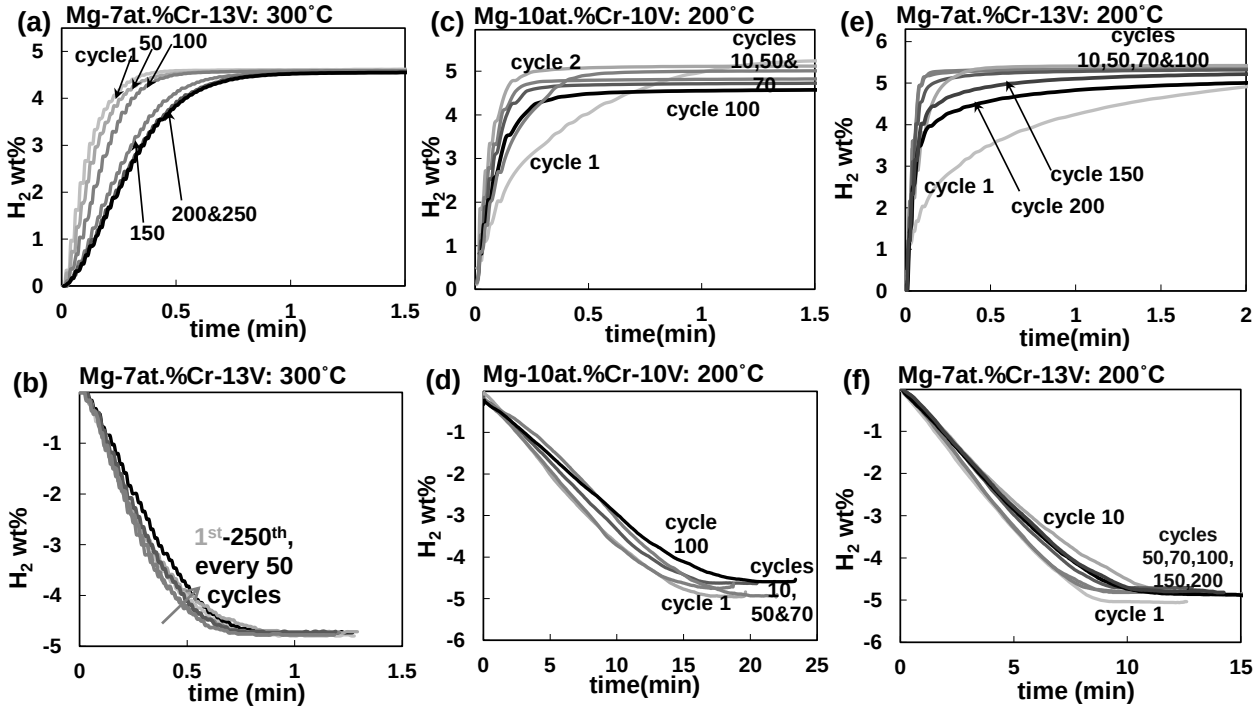

Figure 6.1: Absorption and desorption hydrogenation cycling data for (a) and (b) Mg-

7at.%Cr-13V at 300 ˚C, (c) and (d) Mg-7at.%Cr-13V at 200 ˚C and (e) and (f) Mg-7at.%Cr-13V at 200 ˚C.

Figures 6.1(c) and 6.1(d) shows the absorption and desorption hydrogenation cycling behavior of the Mg-10Cr-10V alloy. Figures 6.1(e) and 6.1(f) show the sorption performance of Mg-7Cr-13V. The graphs show the sorption data for cycles 1, 2, 10, 50, 70 and 100. The system with the V-rich catalyst possesses faster and more stable sorption kinetics. This is going to be highlighted in Figure 6.2. We are currently investigating the origin of this difference though it is likely related to the efficacy of V versus that of Cr for dissociating/recombining hydrogen. The Mg-10Cr-10V alloy was cycled to 115 absorption/desorption cycles before the test was interrupted. Due to its high stability, Mg-7Cr-13V was cycled to 225 cycles. Even after 225 cycles the hydrogen absorption and desorption kinetics remain remarkably rapid.

A composite plot for the time to absorb and the time to desorb 80% of the mean maximum hydrogen gravimetric capacity at 200˚C is shown in Figure 6.2. All the ternary compositions that were tested are shown, along with the binary Mg-10V and Mg-20V alloys. We performed extended cycling on the Mg-13Cr-7V and Mg-7Cr-13V systems. Even towards the end of the 225 absorption/desorption cycles, these systems are able to maintain their high sorption rates. The Figure again illustrates that the more V-rich catalyst gives the optimum performance, especially for the hydrogen desorption. Since Mg-7Cr-13V possessed the most interesting hydrogenation properties we chose that system for extended microstructural characterization via TEM.

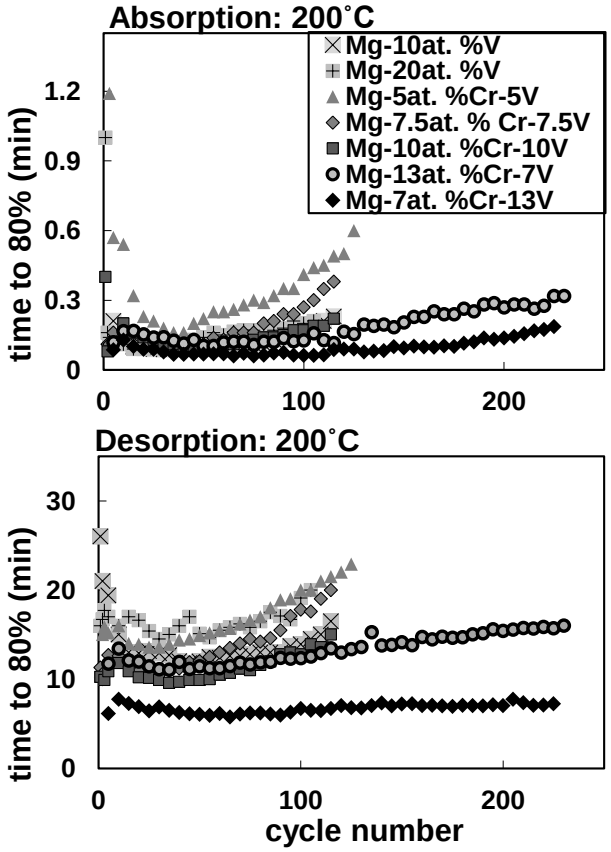

Figure 6.2: A comparison of the time to sorb 80% of the average maximum hydrogen gravimetric capacity for each composition, as a function of sorption cycle number at 200 ˚C.

We tested the hydrogen uptake of the ternary alloys at room temperature. Figure 6.3(a) shows the room temperature absorption curves of activated Mg-7Cr-13V sample for three different pressures. Increasing the pressure, although resulting in faster hydrogen uptake initially, leaves the sample with more unreacted Mg. This is inferred from the lower maximum capacity after a certain absorption time. The cycling performance of this composition at room temperature was also tested. Since the material shows a reasonable performance using the pressure of 2 bar, this pressure was chosen for cycling measurements. Due to the enthalpy of magnesium hydride formation, in order to desorb at rough vacuum (10-15 mbar) the temperature had to be raised to 200˚C. Figure 6.3(b) demonstrates the results for Mg-7Cr-13V for 10 absorptions/desorptions. Despite

experiencing some degradation in the kinetics, the overall performance of the ternary composite at room temperature is remarkable. To our knowledge there are no reports of "bulk" magnesium being absorbed at room temperature many times over at such low pressures. For example, Mg-V binary system has been shown to absorb 2 wt.% H_2 in 15

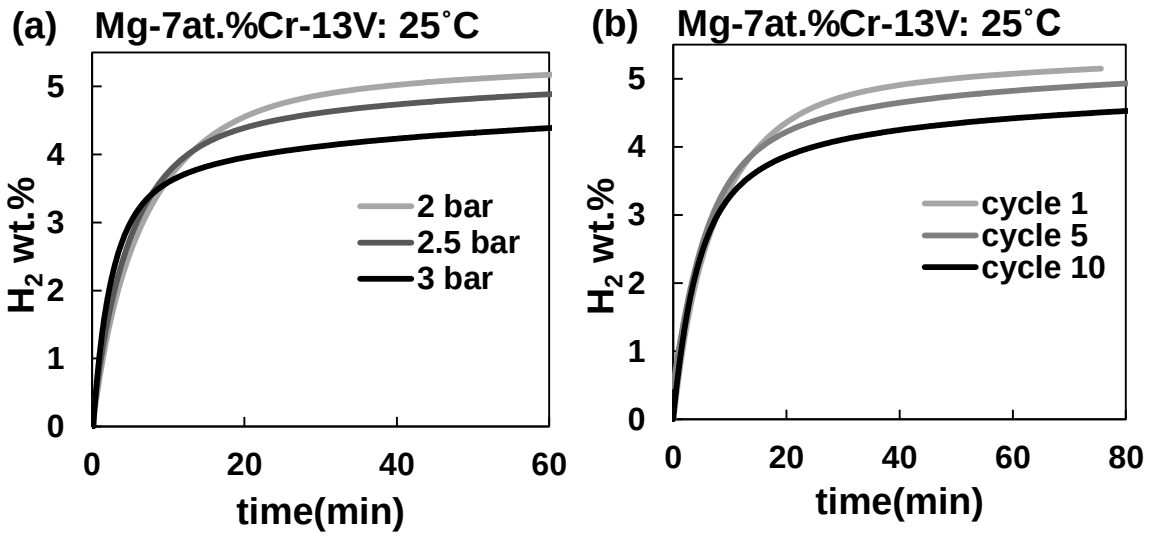

Figure 6.3: Room temperature absorption cycling of Mg-7at.%Cr-13V alloy desorbed at 200 ˚C): (a) the effect of charging pressure on the absorption behavior at cycle 1; (b) cycling performance of the sample at 2 bar absorption pressure.

min at room temperature with a hydrogen pressure of 10 bar [14]. In different study Mg-TiH_2 nanocomposite absorbed about 3.5 wt.% H_2 within 4 hours and under the hydrogen pressure of 40 bar [38].

The pressure - composition - temperature (PCT) plots for the Mg-7Cr-13V system are shown in Figure 5.4. There is a quantifiable hysteresis between the hydride formation plateau and the hydride decomposition plateau. Such hysteresis is well known for de/hydrogenation of magnesium alloys and has been attributed to the difference in the irreversible work associated with the nucleation of the hydride in the metal versus the nucleation of the metal in the hydride [20]. From the three testing temperatures, based on van't Hoff equation, the enthalpy for hydride formation is -74 kJ/mol H_2, while the

enthalpy for hydride decomposition is 80 kJ/mol H_2. The hydride decomposition enthalpy is on par with what is commonly reported in literature, e.g. [4,22,27]. For van't Hoff equation several additional temperatures would result in a more accurate enthalpy value. Nevertheless one can conclusively state that the Cr-V additions do not thermodynamically destabilize MgH_2, and the reported extremely rapid sorption rates are due to enhanced

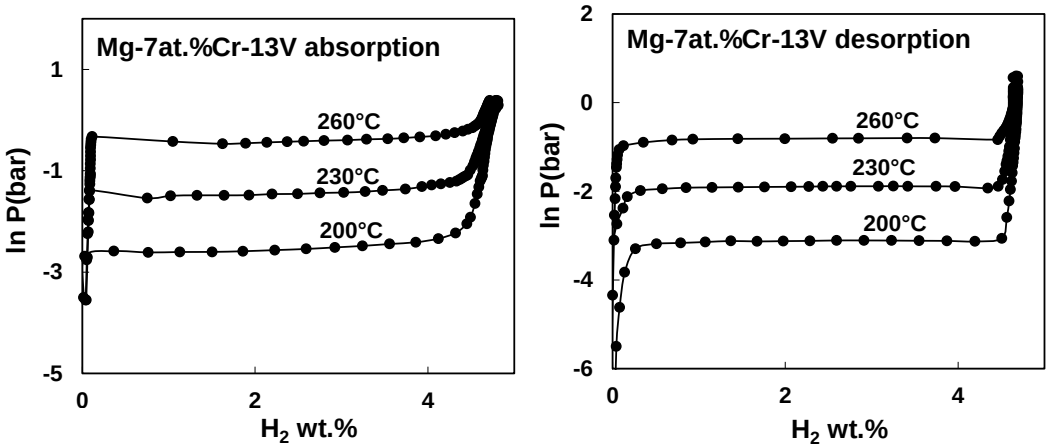

Figure 6.4: Pressure-composition-temperature (PCT) absorption and desorption results for Mg-7at.%Cr-13V.

kinetics. The entropy for hydride formation and decomposition is calculated as -134 and 145 J/K mol H_2, respectively.

6.3.2 Microstructural Analysis

Figure 6.5(a) shows the indexed X-ray diffraction (XRD) curves for four ternary alloys and Mg-10 and 20 V binary alloys, after they were sorption cycled. The samples are shown in the absorbed state. As is indicated in the data, the primary hydrogen-storing phase is tetragonal α-MgH_2. There is no detectable variation of the α-MgH_2 lattice parameters from the literature-reported values. Despite the Ta underlayer, the Mg_6Pd intermetallic was still formed. The experimentally overlapping (446), (066) and (555)

Mg_6Pd peaks are labeled in the figure. The detected (224) Mg_6Pd peak present at $2\theta = 21.6^\circ$ is not shown, while (111) Mg_6Pd at $2\theta = 7.59^\circ$ was outside the range of the detector.

In the absorbed binary Mg-20 V, a vanadium reflection centered at $2\theta = 40.9^\circ$ is detected. Assuming its (110) type reflection gives a lattice parameter of 3.117 Å. From the known lattice parameter for hydrogen-free body centered cubic (bcc) vanadium (a = 3.038 Å), the position of (110) reflection should be at $2\theta = 42.02^\circ$. The lattice expansion indicates the presence of interstitial hydrogen atoms. Using the results from Maeland's work [18] the composition of such an interstitial hydride is $VH_{0.45}$. However, based on the suggested V-H phase diagram [18], such a bcc hydride is only stable at elevated temperatures. At room temperature, where the X-ray measurements were performed, a body centered tetragonal (bct) interstitial vanadium hydride (VH_x) is expected with $x \sim 0.5$. The bct vanadium hydride has the lattice parameters of a = 3.302 and c = 3.002 Å. The position of the strongest reflection for this hydride is centered at $2\theta = 40.5^\circ$. The reported values for enthalpy of $VH_{0.5}$ range between -70 to -83 kJ/mol H_2 kJ/mole H_2 [16], indicating that they would form both at low temperatures and at 200°C. Because of the significant peak broadening associated reflection in question, it is difficult to conclusively identify the exact structure/stoichiometry of this hydride, and we have therefore leave open the possibility that one or both phases may be present.

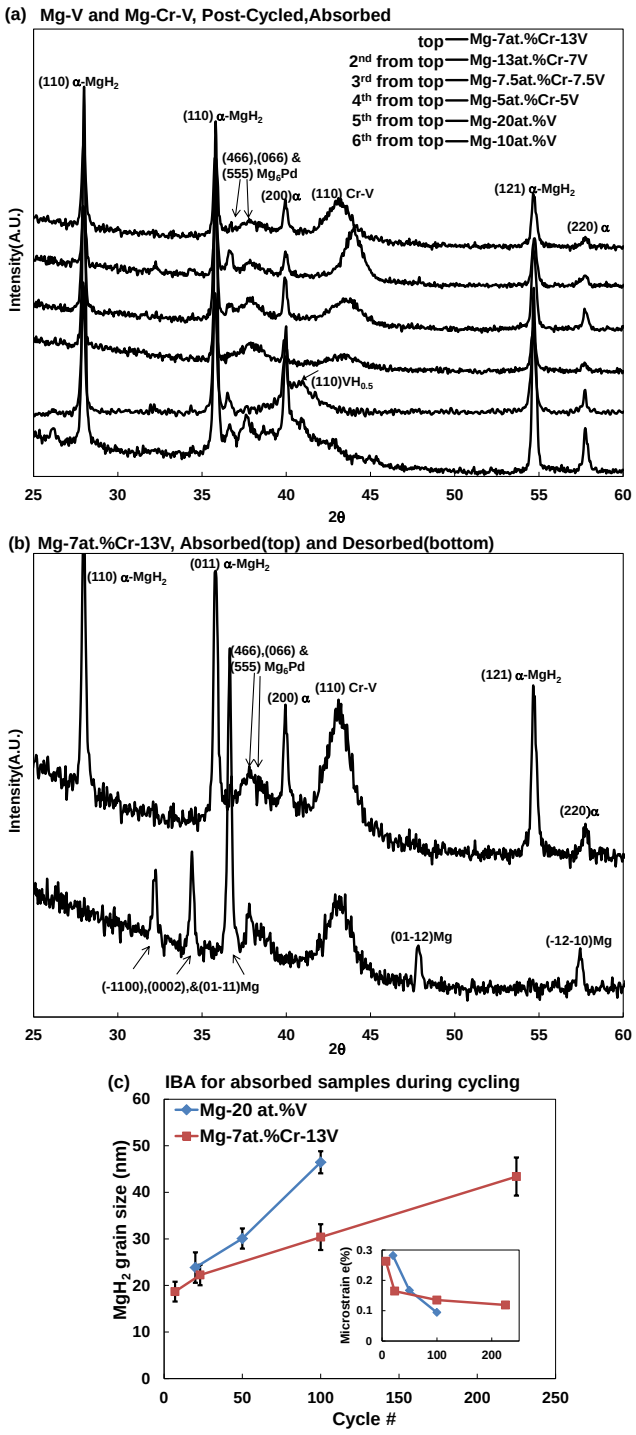

Figure 6.5: Indexed X-ray diffraction patterns of the (a) post-cycled (at 200 ˚C) binary and ternary samples, all in absorbed state and (b) post-cycled Mg-7at.%Cr-13V in the absorbed and desorbed states. Figure (c) Integral breadth analysis (IBA) for the cycled binary and ternary alloys.

The XRD patterns of ternary alloys contained characteristic bcc solid solution Cr-V (011) reflection. The next reflection of this bcc structure, i.e. (002) is much weaker than (110). The formation of a binary solid solution with bcc structure is expected based on the binary phase diagram. The position of the observed peak depends on the Cr:V atomic ratio, roughly obeying Vegard's law. The lattice parameter of Cr (a = 2.884 Å) is smaller than that of V (a = 3.038 Å). Hence the Cr-rich composition shows a peak shift towards larger 2θ values, while the V-rich composition shows vice versa. The (110) reflection of all ternary alloys is quite broad which indicates a nano-crystalline Cr-V phase. The decreasing relative intensity at lower Cr-V contents is due to a decreasing mass fraction of that phase. Figure 6.5(b) compares the absorbed and the desorbed Mg-7Cr-13V. In the desorbed state, α-MgH_2 is replaced by equilibrium magnesium with no variation from the literature reported lattice parameters. Moreover, the position of the (110) reflection of the bcc phase does not change between the absorbed and desorbed states. This indicates that the interstitial hydride either does not form during testing, that it forms at elevated temperature but rapidly desorbs during the cool down, or that it forms and remains completely stable during desorption of magnesium. Elevated temperature in-situ XRD studies would have to be performed to conclusively identify the correct scenario.

Figure 6.5(c) shows the IBA results used to determine the MgH_2 grain size during different stages of cycling at 200 ˚C, for a ternary and a binary alloy. For the binary Mg-20V, MgH_2 grain size starts from 23 nm at the early stages of cycling (cycle 20). This value increases to 30 and 46 nm after 50 and 100 cycles, respectively. As the inset in Fig. 6.5(c) shows, the microstrain values are in the range of 0.10 to 0.28% for binary samples. For the ternary alloy, an increasing trend in hydride grain size is also observed, however the rate of increase is relatively smaller than that of the binary alloy. After 7 cycles, the MgH_2 grain size is 18 nm. The hydride grain size increases to values of 22 and 30 nm after 23 and 100 cycles, respectively Eventually after 225 cycles, the hydride grain size for

ternary alloy reaches to 43 nm which is similar to that of the binary alloy after 100 cycles. The values for microstrain decrease from 0.24% in the early cycles to 0.11% towards the end of cycling. To determine the crystallite size of Cr-V phase, the Scherrer analysis was performed on the Cr-V (110) reflection, which is the only well-resolved Cr-V peak. In all ternary compositions, the Cr-V crystallite size varies between 5-6 nm after extended cycling at 200 ˚C. During the early stages of cycling, this value is in the order of 3-4 nm.

Figure 6.6 shows the SEM results of Mg-7Cr-13V samples after 45, 120 and 225 cycles at 200 ˚C. Figure 6.6(a) shows that after 45 cycles, the material consists of large flakes with high density of surface cracks. As the cross-section view in Figure 6.6(b) depicts, these cracks do not extend all the way through the bulk material. After 120 cycles, the material still resembles a film, though with a much higher density of coarse surface cracks. The plan view image in Figure 6.6(c) highlights this progressive film disintegration. As seen in Figure 6.6(d), the cracks propagate deeper into the bulk of the film. The original film is entirely pulverized after 225 cycles. This is highlighted in Figures 6.6(e) and 6.6(f). At this stage, original film is effectively a powder, consisting of what appears to be a bimodal distribution of agglomerated particles.

Figure 6.7 shows the results of TEM analysis performed on the Mg-7Cr-13V sample in its desorbed state after 220 cycles. Figure 6.7(a) shows the bright field (BF) image of the “powder agglomerate”. As this image indicates, the agglomerate consists of a coarse single grain along with numerous ultra-fine crystallites. The selected area diffraction (SAD) pattern of this agglomerate is shown in Figure 6.7(b). The spots observed in the SAD pattern are due to the relatively large magnesium grain, which shown in the dark field (DF) image in Figure 6.7(c). The DF image is taken near the $[1\text{-}211]_{Mg}$ zone axis. Apart from the spot pattern in the SAD pattern a series of rings is also evident. The simulation of the SAD ring pattern indicates that the observed rings are associated with the bcc Cr-V phase. Recent TEM studies on the ball-milled MgH_2 powders also showed the presence of MgO on the surface [39,40]. In order to rule out the possibility of the MgO

as the corresponding phase, the MgO simulated pattern was also produced (results not shown).

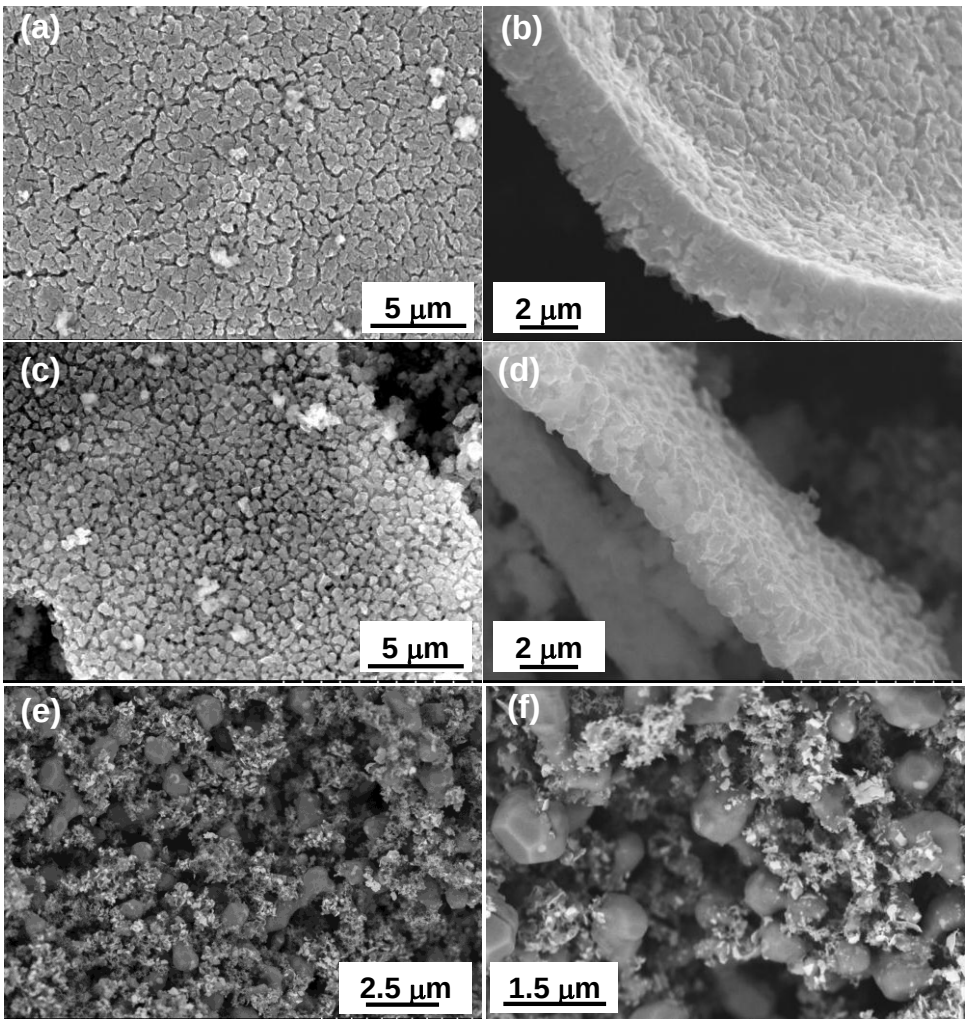

Figure 6.6: SEM micrographs of Mg-7at.%Cr-13V during the course of cycling at 200 ˚C. Figures (a) and (b) show the top and cross-section views after 45 cycles. Figures (c) and (d) show the material after 120 cycles. Figure (e) and (f) show the material after 225 cycles, highlighting its transformation to an agglomerated powder.

The present ring pattern did not match the MgO simulated pattern at all. Figure 6.7(d) shows a dark field image of the Cr-V nanocrystallites obtained by using a portion of the $110_{Cr\text{-}V}$ reflection. As this micrograph indicates, the distribution of the catalyst phase is not entirely uniform though only a fraction of the total Cr-V crystallites show up in a single

dark field micrograph. The scale of the nanoparticle distribution is much finer than the dimensions of the Mg crystallite. Both the bright filed and dark field images of the metallic magnesium particle show contrast associated with planar defects such as twins or stacking faults. However there is no evidence of Ashby-Brown type strain contrast that would be expected if the Cr-V particles were embedded into the bulk of the metallic matrix e.g. [41,42,43]. A general hypothesis could therefore be put forward regarding the microstructural evolution in these materials: After co-deposition, but before hydrogentation, the catalytic elements have been demonstrated to remain in supersaturated solid solution [29]. During the early stages of absorption a nanodispersed Cr-V phase forms at the Mg/MgH_2 grain boundaries. As the sample is progressively cycled

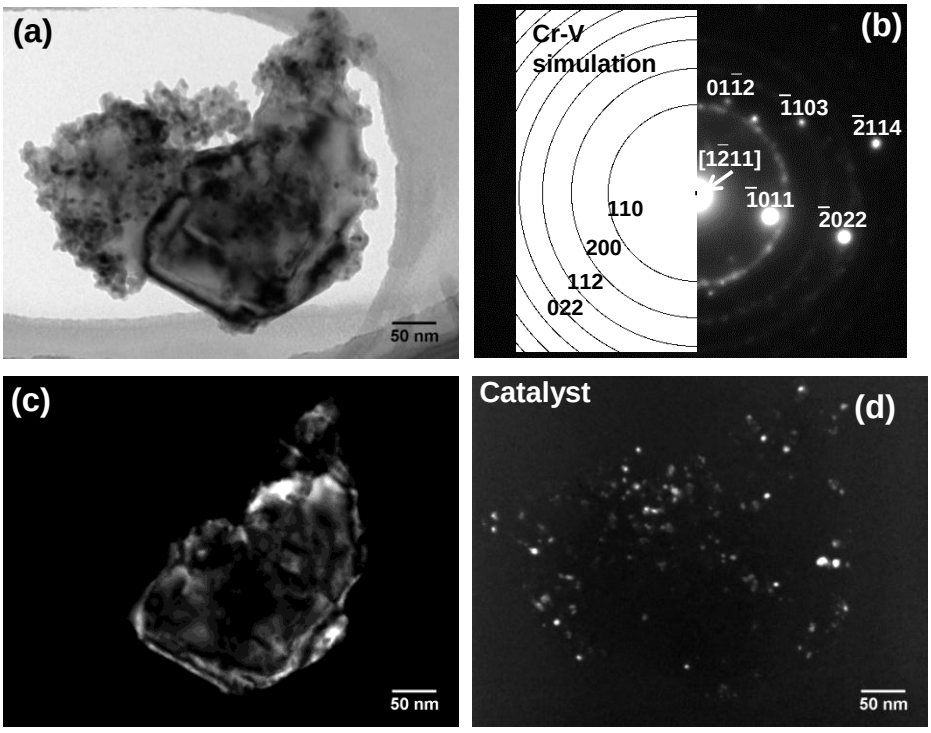

Figure 6.7: TEM micrographs of desorbed Mg-7at.%Cr-13V after 220 cycles at 200 ˚C. (a) Bright field micrograph of an agglomerate; (b) Corresponding SAD pattern with the simulated ring pattern of the Cr-V phase and single crystal Mg; (c) Dark field micrograph obtained using g = -1011Mg reflection; (d) Dark field micrograph, obtained using the portion of $110_{Cr\text{-}V}$ ring, highlighting the Cr-V nanocrystallites.

the films crack intergranularly forming loose agglomerates. As a result the catalyst nanocrystallites wind up decorating the metal/hydride particle surfaces.

The TEM analysis of a partially absorbed Mg-7Cr-13V sample, after 150 cycles, is shown in Figure 6.8. The imaged region contains a metallic magnesium crystallite, and magnesium hydride crystallite, and large number of catalyst particles. In the observed agglomerate there may be additional Mg and/or MgH_2 grains. However they are not in strong Bragg contrast. Figure 6.8(a) shows a bright filed micrograph of the imaged area. Figure 6.8(b) shows am indexed two-beam SAD pattern from the metallic magnesium, which Figure 6.8(c) shows the corresponding dark field image. Upon slight tilting of the specimen we were able to obtain the SAD pattern of the α-MgH_2, also oriented in a strong Bragg orientation with a systematic row of $g = 011\alpha$ reflections excited. The ring pattern from the Cr-V nanocrystallites, which also show up in the SAD, is included in the simulation overlay. The hydride possesses characteristic mottled contrast characteristic of ionic materials and previously reported for MgH_2 [44]. As Figure 6.8(f) indicates the Cr-V nanocrystallites retain their dense, albeit non-uniform distribution, even after 150 cycles. These images indicate that during absorption the formation and growth of the hydride phase does not take place in the way described by the contracting volume, aka contracting envelope or core shell, model [45]. While previously we have demonstrated that during hydrogen desorption there is no evidence for contracting volume in magnesium hydride, [46], to our knowledge this is the first direct TEM-based observation for the absorption. The driving force for absorption in our experiments was relatively high, while the sorption temperature was quite low, as compared to typical MgH_2 studies, e.g. [14,15]. Thus our results should rule out most possibilities of contracting volume type phase transformations in magnesium/magnesium hydride, with very large polycrystalline specimens and near-room temperature absorption being the two possible exceptions.

Another feature observed the partially absorbed microstructure is the presence of growth twins. Though deformation twins have been reported previously for high energy

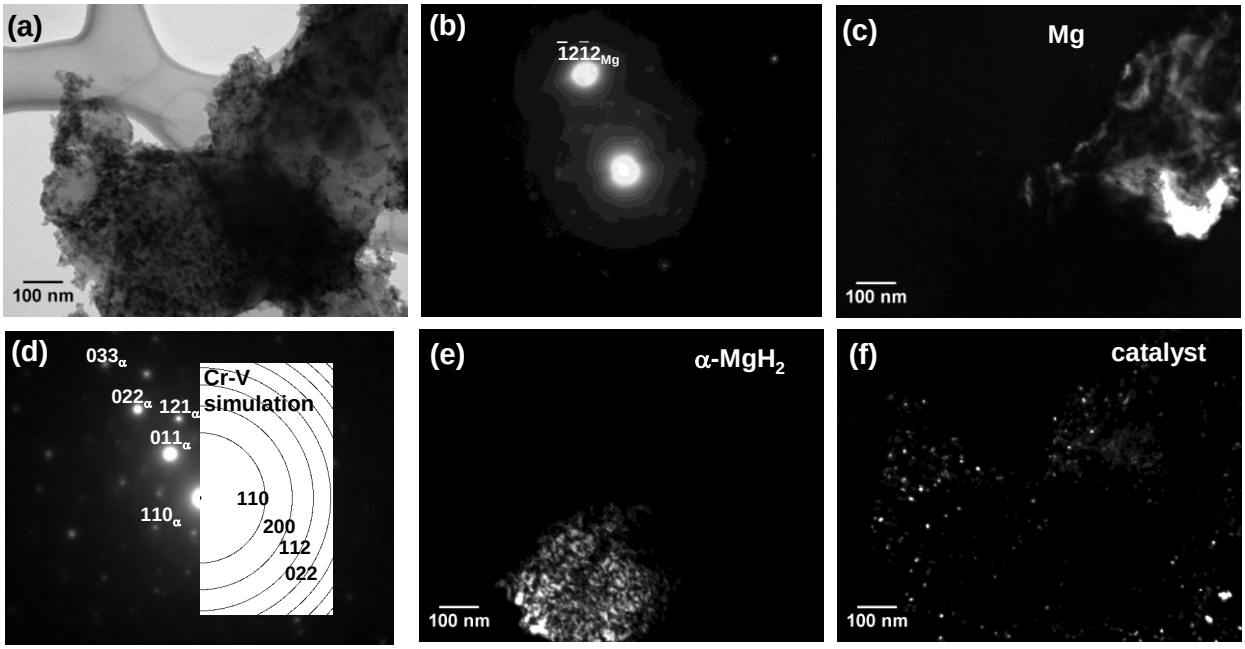

Figure 6.8: TEM micrographs of Mg-7at.%Cr-13V after 150 cycles at 200 ˚C and partially absorbed. (a) The bright field micrograph; (b) Corresponding SAD pattern of the metal phase; (c) Dark field micrograph obtained from g= -12-12reflection; (d) Corresponding SAD pattern of the area near the a-hydride phase; (e) Dark field micrograph, obtained using the g=011_{MgH2} reflection; (f) Dark field micrograph obtained using $110_{Cr\text{-}V}$ reflection.

milled MgH_2 powders [39,46], growth twins are a new finding. Figure 6.9 shows an example of such twins, which formed during the fast absorption process. As the SAD pattern in Figure 6.9(b) shows, the hydride matrix and twin are close to [131] and [1-31] zone axes, respectively. The twins shown in the dark field micrograph (Figure 6.9(c)) are imaged using the g = 211α reflection. Without tilting the sample, the MgH_2 matrix could be imaged using the g = 2-11α reflection, as shown in Figure 6.9(d).

For further characterization of the cycled microstructure we performed high resolution TEM on the desorbed Mg-7Cr-13V powder sample that was cycled for 270

times. Figure 6.10(a) shows the area used for HRTEM in low magnification. The diffraction pattern presented in Figure 6.10(b) is from this area, showing the presence of large magnesium single crystals along with a ring pattern of the fine-grained Cr-V bcc phase.

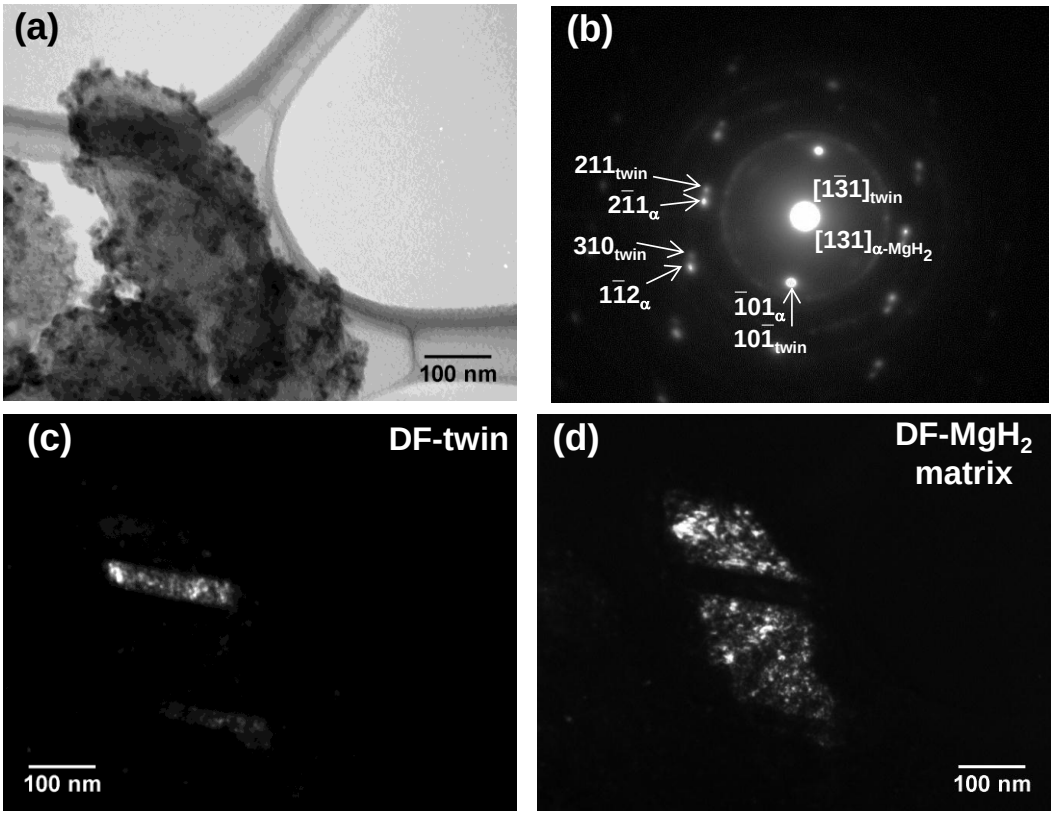

Figure 6.9: TEM micrographs of partially absorbed Mg-7at.%Cr-13V after 150 cycles at 200 ˚C. (a) The bright field micrograph; (b) corresponding SAD pattern; (c) Dark field micrograph of the twinned MgH_2 obtained using the g = 211_{twin}; (d) Dark field micrograph obtained from g = $2\text{-}11_{MgH2}$ reflection.

The two labeled diffraction spots correspond to the 01-11 and 01-12 magnesium d-spacings. Since the angle between these two g-vectors is not 49.8 ˚ (the corresponding angle in [01-11] zone axis), these spots are from two separate magnesium grains. Micrographs shown in Figures 6.10(c) to (f) are HRTEM data from this region. It can be observed that the secondary bcc phase is crystalline with average grain diameter around 5

to 10 nm. Due to overlapping of these grains we occasionally encounter Moiré fringes (two cases of these fringes are marked with white arrows in Fig. 6.10(c) and (d)). This observation is common in microstructures that contain large density of grain boundaries, e.g. nano-structured alloys processed via severe plastic deformation [47].

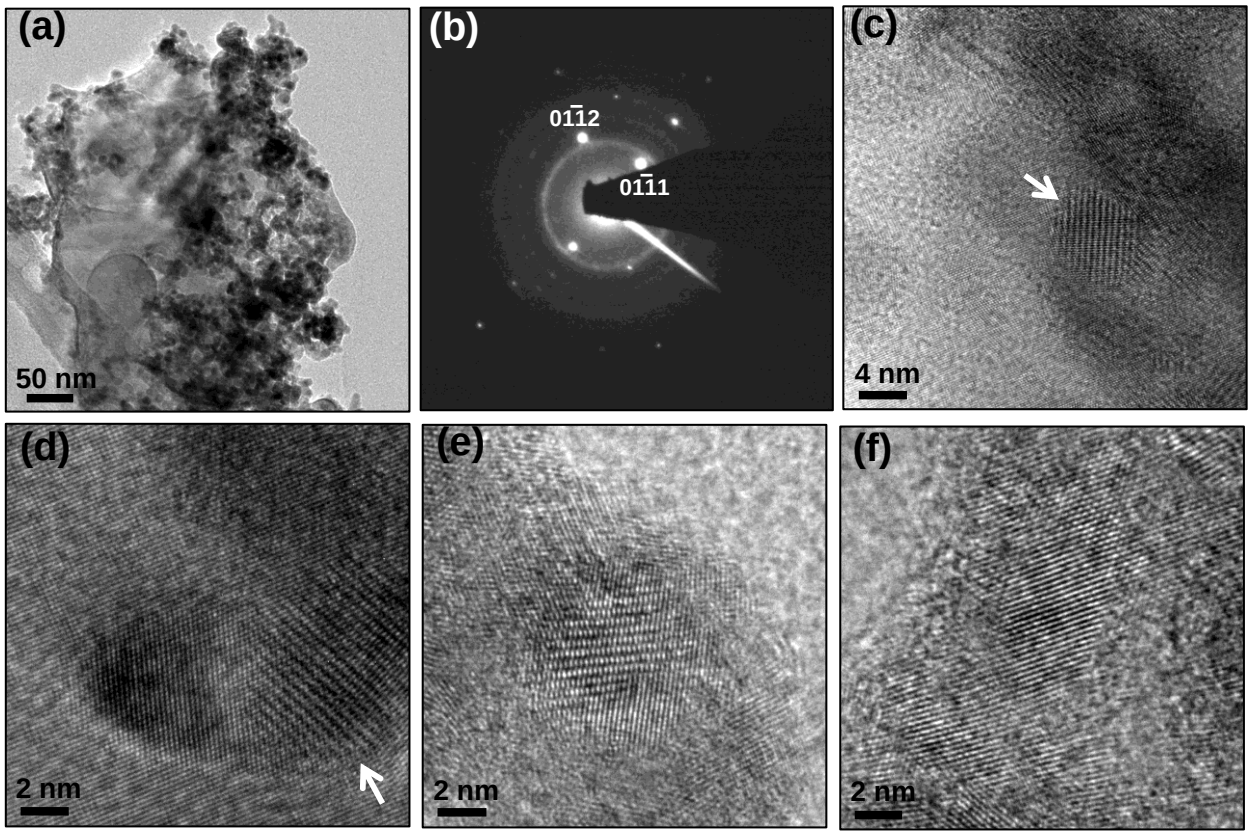

Figure 6.10: Mg-7at.%Cr-13V sample cycled 270 times in desorbed state: (a) Low magnification micrograph showing the general area used for HRTEM analysis, (b) Diffraction pattern from area in (a) showing large magnesium single crystals and a fine-grained bcc phase, (c) to (f) HRTEM micrographs from the area containing the bcc phase.

6.3.3 Kinetics analysis

The value of the activation energy provides an important insight regarding the sorption mechanism. The Avrami exponent, n is also an important factor in understanding the phase transformation. By fitting the sorption data with the JMA equation, the kinetics

parameters k and n are extracted. The two driving force equations (eq. (6.5) and (6.6)) introduced in the Experimental section are used for the kinetics analysis. To investigate

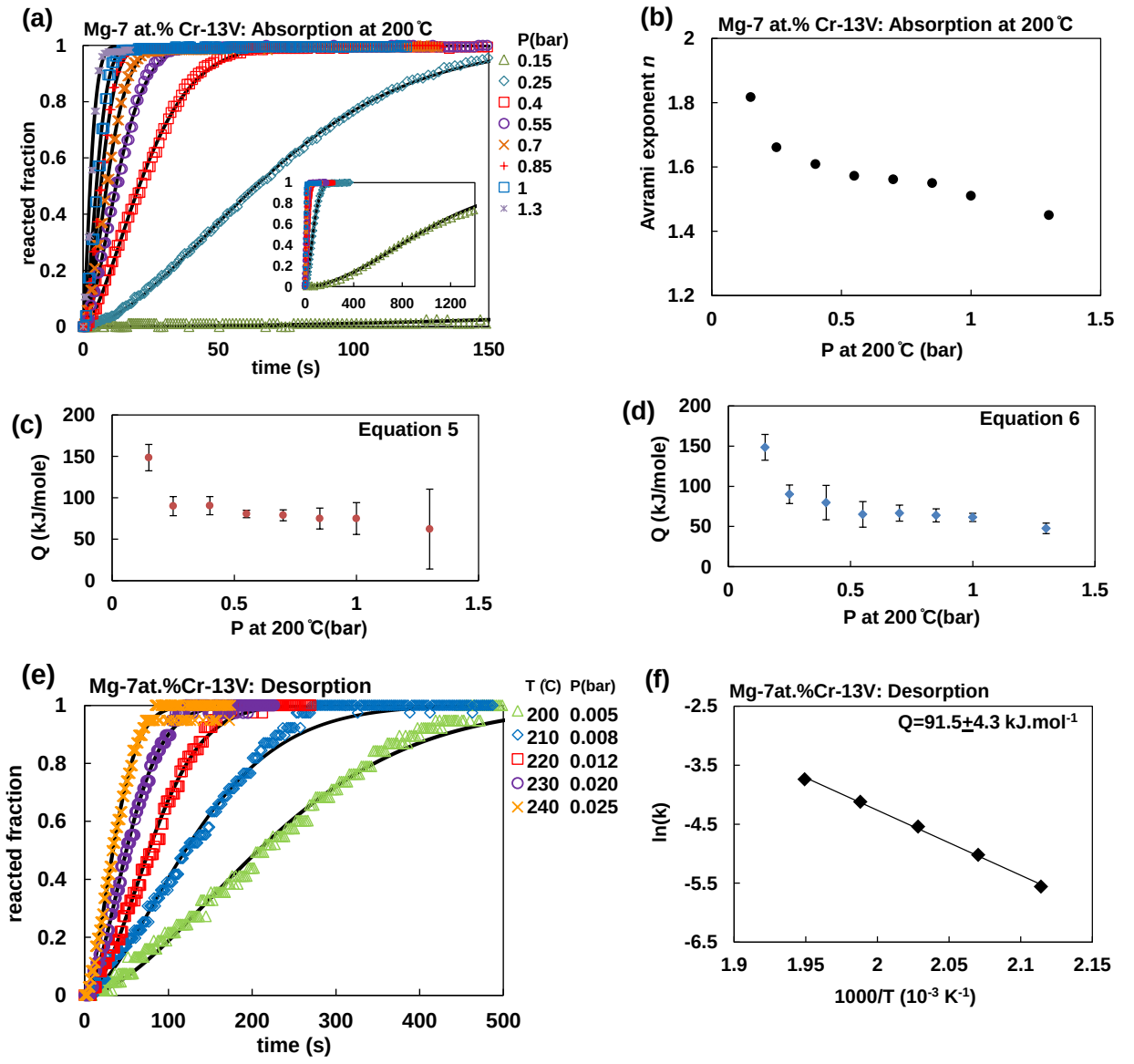

Figure 6.11(a) shows absorption curves at 200 ˚C as a function of pressure. The solid lines indicate the fitted curves based on JMA model. Figure 6.11(b) shows the variation of the Avrami exponent, n as a function of pressure at 200 ˚C. Figures 6.11(c) and (d) show calculated activation energies based on Equation 5 and 6, respectively. Figure 6.11(e) shows the desorption data at various pressures so as to maintain a constant driving force. Figure 6.11(f) shows the resultant desorption activation energy.

the influence of applied driving force on the activation energy we tested at 8 different driving forces. Every driving force value corresponds to a unique pressure-temperature combination. The pressures vary between the values very close to the equilibrium plateau (~ 0.1 bar at 200˚C) to 1.3 bar. The effect of pressure on the absorption kinetics is shown in Figure 6.11(a). The solid lines in the plot represent the fitted curves. As it is shown in Figure 5.11(b), the Avrami exponent, n varies between 1.85 at the lowest pressure to 1.45 at the highest pressure.

The rate constants, k, obtained from these fits were used to calculate the activation energies using the standard $\ln(k)$ vs. $1/T$ formulation. A weighted least square method was used to obtain the activation energy and the corresponding error bars. In this method a specified weight is defined for each k value. These weights are inversely proportional to the fitting error. The values of activation energies, obtained using the two different driving force equations, are presented in Figures 6.11(c) and (d). It is worth noting that at a low absorption pressure both equations produce a driving force of a similar magnitude with hence similar activation energies. The thermodynamic driving force shows lower error at lower pressures compared to that of the diffusion-limited reaction. However this trend is reversed at higher pressures. In both cases activation energies generally decrease with increasing pressure.

Similar to absorption curves a sigmoidal characteristic is also observed in the desorption kinetics. This is illustrated at Figures 6.11(e) and (f). In contrast to the absorption activation energy measurements, the activation energy for desorption was only tested in single driving force. At the low desorption pressures tested, Equations (6.5) and (6.6) gave nearly identical values. An activation energy of 91.5 kJ/mole is obtained for the desorption process.

6.4 Discussion

The variation in the sorption properties for the differing Cr-V compositions is likely related to their interaction with hydrogen; that is their efficacy for hydrogen dissociation/ recombination. The superior sorption performance of Cr-V with an atomic ratio of 1:2 over the 1:1 and 2:1 systems may be rationalized by the catalytic superiority of V over Cr. However, there does exist a unique synergy for the bimetallic system over the elemental catalyst. This warrants further investigation via *ab initio* modeling methods. In the case of low Cr-V contents, i.e. 5-5 and 7.5-7.5, the amount of the catalyst materials seems to be insufficient to achieve the desired kinetic performance.

The TEM observations of the partially absorbed sample revealed some important aspects of the hydrogenation process. Absorption at high pressures – low temperatures did not give rise to the formation of numerous MgH_2 nuclei on the surface of a relatively large particle. Thus there is no evidence of a contracting volume structure that would result in such a scenario (see reference [48] and associated citations for a discussion of this mechanism). Rather, the formation of isolated MgH_2 nuclei and their subsequent growth into the magnesium crystallites is the hydriding mechanism. Another important feature of partially absorbed microstructure is the presence of twins. It is known that internal stresses occurring during phase transformations promote twinning in non-ductile materials. For example the formation of internally twinned hydride precipitates upon hydrogenation of zirconium has been reported [49]. The formation of such structure was attributed to the compensation of the internal stress buildup. A similar scenario is envisioned during the hydrogenation of magnesium. During the sorption process not all grains hydride simultaneously. As a hydride grain formed in the proximity of the untransformed magnesium crystallites the large volumetric mismatch between the two phases (24.6% with respect to the hydride phase) would create significant stresses around it. This internal stress, along with a presence trace levels Cr and V impurities in the hydride, would

promote twinning. Since sorption occurs quite rapidly there is insufficient time to anneal the twins out.

The meaning of the activation energy associated with the magnesium to magnesium hydride phase transformation is still debated in literature. Moreover recent modeling work also indicates that because of the interdependence of hydrogen diffusion and dissociation mechanisms a single rate-limiting step may not exist at all [50]. Our analysis highlights the difficulty of ascribing an exact mechanism to the measured activation energy. The activation energy has contributions from both nucleation and growth steps [35]. As was demonstrated in Figure 6.11, the activation energy in fact changes with the driving force almost monotonically. The activation energies are better described by Equation 5.5 at low driving forces. However, as the driving force increases, Equation 6.6 results in more accurate activation energies. The Avrami exponents also showed a decreasing trend with increasing the driving force for absorption. It can be argued that the observed decreasing trend in the Avrami exponent along with the variation of the activation energy with driving force suggest a probable trend in the contribution of nucleation and growth mechanisms to the overall activation energy. Such a trend can be explained by considering the effect of the absorption pressure i.e. the driving force on the rate of the nucleation process. As the absorption pressure increases, the rate of nucleation also rises towards a situation where at a very high driving force the saturation of nucleation sites occurs at the initial stage of absorption. The decreasing trend in the Avrami exponents corresponds to the variation in the rate of nucleation from decreasing to almost instantaneous. The latter can be expressed using the $d/m+a$ interpretation of the Avrami exponent where a decreases to zero. Therefore, the drop in the activation energy can be attributed to the diminishing contribution of the activation energy of nucleation. The diffusion controlled growth with decreasing nucleation rate we suggested here is also described by Christian [35] for $1.5<n<2.5$.

Perhaps one can argue that at high pressures the measured values of activation energy agree with diffusion of hydrogen in magnesium. For example based on the work by

Rener and Grabke [51], the activation energy for diffusion of hydrogen in magnesium would be 40 kJ/mole. For the ionic diffusion of hydrogen in the hydride phase a variety of experimental and theoretical studies yielded values ranging from 98 to 166 kJ/mole [52-54]. Therefore, it seems unlikely that diffusion of hydrogen in the hydride layer could be correlated with the measured activation energies at high pressure.

Based on the above mentioned arguments and the microstructural analysis a general picture of the absorption mechanism can be visualized as shown in the schematic given in Figure 6.12. Upon the nucleation of the hydride, which is rich in hydrogen atoms, a hydrogen depleted area is formed around the nucleus. Further growth of hydride is limited by the hydrogen diffusion rate in the Mg matrix. Therefore, it is suggested that the absorption kinetics is governed by nucleation of the new hydride phase along with hydrogen diffusion through the metal matrix. However, we argue that the situation is fairly difficult to resolve based on Avrami analysis, that one should interpret the measured *n* and Q values with caution, and that it is not surprising that the literature reported activation energies for nominally identical materials system seldom agree with each other.

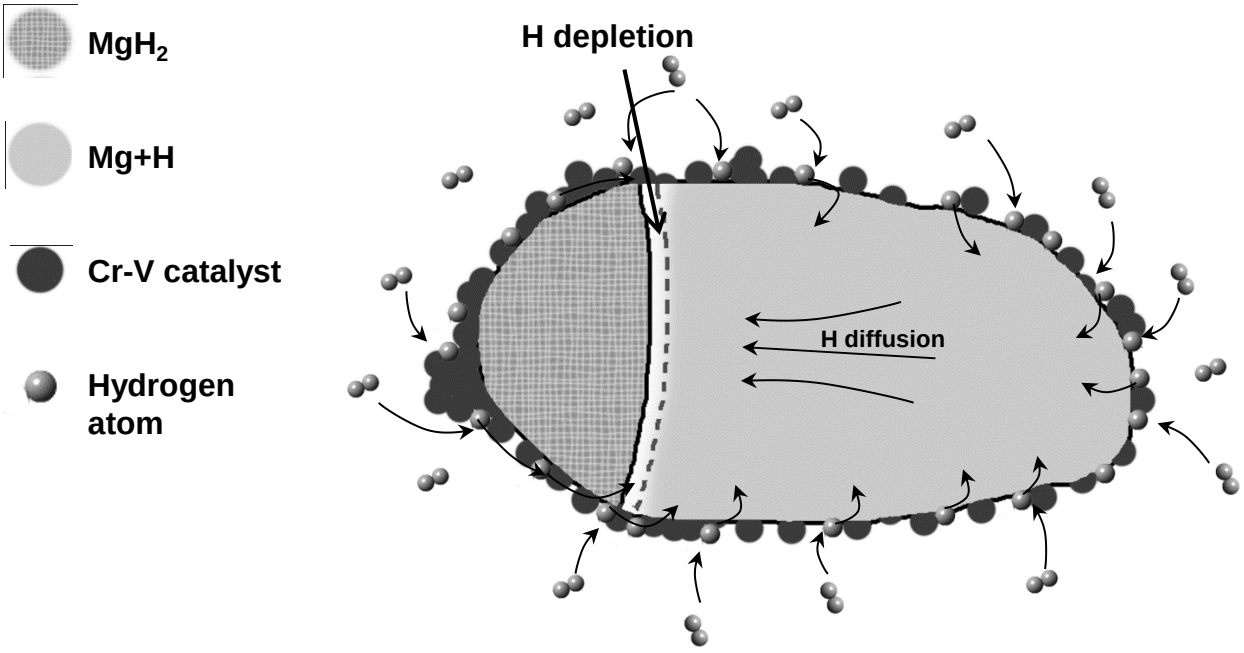

Figure 6.12: Schematic representation of the proposed hydride growth mechanism.

6.5 Conclusions

A bimetallic chromium vanadium hydrogen sorption catalyst for magnesium hydride (MgH_2) allowed for rapid hydrogen sorption in the temperature range of 25˚C to 300˚C. The catalyst was sufficiently potent that room temperature absorption of 5 wt.% hydrogen was achieved at 2 bar in about an hour. At 200˚C and at 300˚C the Cr-V catalyzed system could be repeatedly sorbed for 225 plus cycles with minimal degradation in the kinetics.

We performed detailed TEM analysis on partially absorbed Mg-7at.%Cr-13V sample and HRTEM analysis on the Cr-V catalyst. Analysis demonstrates that the catalyst is both nano-scale and nano-dispersed. Early in the absorption cycling the Cr-V nanocrystallites were most likely situated at the Mg/MgH_2 grain boundaries. With progressive cycling the films decrepitated into powder agglomerates with the Cr-V particles wounding up decorating the Mg/MgH_2 crystallite surfaces. The isolated nucleated hydride grains were much larger in scale and coarser in distribution that the catalyst particles and there was no core shell structure present. We employed HRTEM to show the crystallinity of the Cr-V phase.

Kinetic analysis, performed at 200˚C on the Mg-7at.%Cr-13V samples, showed almost a monotonic change in the absorption activation energy with hydrogen pressure. This finding better helps to explain the almost wide discrepancy in the literature reported values of activation energy. This novel observation, combined with measured Avrami exponents that could correlate to a number of growth scenarios, creates a situation where it is difficult to speculate about the rate limiting mechanisms for the absorption process.

Acknowledgements This research was supported by NSERC Hydrogen Canada (H2CAN) Strategic Research Network and by NINT NRC. The authors are grateful to Dr. Peter Kalisvaart for the valuable discussions and comments.

6.6 References

[1] Srinivasan, S.; Magusin, P. C. M. M.; van Santen, R. A.; Notten, P. H. L.; Schreuders, H.; Dam, B. J. Phys. Chem. C 2011, 115, 288.

[2] Yu, X. B.; Guo, Y. H.; Yang, H.; Wu, Z.; Grant, D. M.; Walker, G. S. J. Phys. Chem. C 2009, 113, 5324.

[3] Dai, J. H.; Song, Y.; Yang, R. J. Phys. Chem. C 2010, 114, 11328.

[4] Kalisvaart, W.P.; Kubis A.; Danaie, M.; Amirkhiz, B.S.; Mitlin, D. Acta Mater. 2011, 59, 2083.

[5] Jeon, K.-J. ; Moon, H. R.; Ruminski, A. M.; Jiang, B.; Kisielowski, C.; Bardhan, R.; Urban, J. J. Nat. Mater. 2011, 10, 286.

[6] Palmisano, V.; Filippi, M.; Baldi, A.; Slaman, M.; Schreuders, H.; Dam, B. Int. J. Hydrogen Energy, 2010, 35, 12574.

[7] Tao, S. X.; Notten, P. H. L.; van Santen, R. A.; Jansen, A. P. J. Phys. Rev. B 2011, 83, 195403.

[8] Tan, Z.P.; Chiu, C.; Heilweil, E.J.; Bendersky, L.A. Int. J. Hydrogen Energy, 2011, 36, 9702.

[9] Bendersky, L.A.; Chiu, C.; Skripnyuk, V.M.; Rabkin, E. Int. J. Hydrogen Energy, 2011, 36, 5388.

[10] Barcelo, S.; Rogers, M.; Grigoropoulos, C. P.; Mao, S. S. Int. J. Hydrogen Energy, 2010, 35, 7232.

[11] Lang, J.; Huot, J. J. Alloys Compd. 2011, 509, L18.

[12] Dura, J. A.; Kelly, S. T.; Kienzle, P. A.; Her, J.-H.; Udovic, T. J.; Majkrzak, C. F.; Chung, C.-J.; Clemens, B. M. J. Appl. Phys. 2011, 109, 093501.

[13] Nielsen, T. K.; Besenbacher, F.; Jensen T. R. Nanoscale 2011, 3, 2086.

[14] Liang, G.; Huot, J.; Boily, S.; Van Neste A.; Schulz, R. J. Alloys Compd. 1999, 291, 295.

[15] Liang, G.; Huot, J.; Boily, S.; Schulz, R. J. Alloys Compd. 2000, 305, 239.

[16] Schlapbach, L. In Hydrogen in Intermetallics I; Schlapbach, L. Ed.; Springer-Verlag: 1999.

[17] Silveira, M. G; Gremaud, R.; Baldi, A.; Schreuders, .; Damd, B.; Griessen R. Int. J. Hydrogen Energy, 2010, 35, 6959.

[18] Maeland, A.J. J. Phys. Chem. 1964, 68, 2197.

[19] Kecik, D.; Aydinol, M.K. Surf. Sci. 2009, 603, 304.

[20] Griessen , R.; Riesterer, T.; Flanagan, T.B.; Oates, W.A. In Hydrogen in Intermetallics I; Schlapbach, L. Ed.; Springer-Verlag: 1988.

[21] Niessen, R.A.H.; Notten, P.H.L. Electrochem. Solid-State Lett. 2005, 8, A534.

[22] Zahiri, B.; Amirkhiz B.S.; Mitlin, D. Appl. Phys. Lett. 2010, 97,083106.

[23] Tao, S. X.; Notten, P. H. L.; van Santen, R. A.; Jansen, A. P. J. Phys. Rev. B 2010, 82, 125448.

[24] Zahiri, B.; Amirkhiz, B.S.; Danaie, M.; Mitlin, D. Appl. Phys. Lett. 2010, 96, 013108.

[25] Kalisvaart, W.P.; Harrower, C.T.; Haagsma, J.; Zahiri, B.; Luber, E.J.; Ophus, C.; Poirier, E.; Fritzsche, H.; Mitlin, D. Int. J. Hydrogen Energy 2010, 35, 2091.

[26] Kale, A.; Bazzanella, N.; Checchetto, R.; Miotello, A. Appl. Phys. Lett. 2009, 94, 204103.

[27] Zahiri, B.; Harrower, C.T.; Amirkhiz, B.S.; Mitlin, D. Appl. Phys. Lett. 2009, 95, 103114.

[28] Amirkhiz, B.S.; Zahiri, B.; Kalisvaart, W.P.; Mitlin, D. Int. J. Hydrogen Energy, 2011, 36, 6711.

[29] Kalisvaart, W.P; Luber, E; Fritzsche, H.; Mitlin, D. Chem. Commun. 2011, 47, 4294.

[30] Fritzsche, H.; Ophus, C.; Harrower, C.T.; Luber, E.; Mitlin, D.; Appl. Phys. Lett., 2009, 94, 241901.

[31] Fritzsche, H.; Saoudi, M.; Haagsma, J.; Ophus, C.; Luber, E.; Harrower, C.T.; Mitlin, D. Appl. Phys. Lett. 2008, 92, 121917.

[32] Danaie M.; Mitlin, D. J. Alloys Compd. 2009, 476, 590.

[33] Klug H.P.; Alexander L.E.; X-ray Diffraction Procedures, John Wiley and Sons, New York, 1974, 643.

[34] Avrami, M. J. Chem. Phys. 1940, 8, 212.

[35] Christian, W. The Theory of Transformations in Metals and Alloys, Pergamon, Oxford, 1975.

[36] Forde, T.; Maehlen, J.P.; Yartys, V.A.; Lototsky, M.V.; Uchidab, H. Int. J. Hydrogen Energy 2007, 32, 1041.

[37] Rudman, P. S. J. Appl. Phys. 1979, 50, 7195.

[38] Lu, J.; Choi, Y.; Fang, Z. Z.; Sohn, H. Y.; Rönnebro, E. J. Am. Chem. Soc. 2010, 132, 6616.

[39] Amirkhiz, B.S.; Danaie, M.; Mitlin, D. Nanotechnol. 2009, 20, 204016.

[40] Beattie, S. D.; Setthanan, U.; McGrady, G. S. Int. J. Hydrogen Energy 2011, 36, 6014.

[41] Mitlin, D.; Radmilovic V.; Dahmen U.; Morris, J.W. Metal. Mater. Trans. A., 2001, 32A, 197.

[42] Mitlin D.; Radmilovic V.; Morris J.W. Metal. Mater. Trans. A., 2000, 31A, 2697.

[43] Mitlin D.; Radmilovic V.; Morris J.W. Mat. Sci. Eng. A., 2001, 301, 231.

[44] Amirkhiz, B.S.; Danaie, M.; Barnes, M.; Simard, B.; Mitlin, D. J. Phys. Chem. C 2010, 114, 3265.

[45] Rudman, P. S. J. Less-common Met. 1983, 89, 93.

[46] Danaie, M.; Tao, S.X.; Kalisvaart, W.P.; Mitlin, D. Acta Mater. 2010, 58, 3162.

[47] Rentenberger, C.; Waitz, T.; Karnthaler, HP. Scripta Materialia 2004, 51, 789.

[48] Bloch, J.; Mintz, M.H.; J. Alloys Comp., 1997, 253, 529.

[49] Bradbrook, J. S.; Lorimer, G. W.; Ridley, N. J. Nucl. Mater. 1972, 42, 142.

[50] Borgschulte A.; Gremaud R.; and Griessen R., Phys. Rev. B., 2008, 78, 094106.

[51] Renner, J.; Grabke, H.J. Z. Metallkd. 1978,67, 639.

[52] Conradi, M; Mendenhall, M.; Ivancic, T.; Carl, E.; Browning, C.; Notten, P.; et al. J Alloy Compd. 2007, 446,499–503.

[53] Hao, S.; Sholl, D. Appl. Phys. Lett. 2008, 93, 251901.

[54] Cermak, J.; Kral, L. Acta Mater. 2008, 56, 2677.

7 Concluding remarks

7.1 Conclusions

In this thesis, the influence of addition of a new series of binary metallic alloy on the hydrogen sorption kinetics of magnesium hydride was investigated. Chapters 2, 3 and 4 were mainly focused on finding different bi-metallic compounds to catalyze the absorption/desorption reactions. In Chapter 5, a detailed study on the microstructural origins of the catalyzed Mg was presented.

In order to design a catalyst for the sorption reaction of magnesium, several criteria must be met. The catalyst must possess high ability to dissociate hydrogen molecules and also act as high diffusivity path for hydrogen atoms. In order to maintain its effectiveness, the catalyst must be strongly resistant to coarsening during the course of hydrogen sorption cycling. We hypothesized that the use of a bi-metallic alloys has superior effect over individual metal elements in this respect. In Chapter 2, we successfully proved the validity of our hypothesis in the case Mg-Fe-Ti ternary system. This ternary system showed superb stability in absorption/desorption kinetics over 100 cycles at 200˚C. The optimum amount of addition was found to be 10 at.%Fe and 10 at.% Ti while extra additions resulted in similar kinetics with less reversible capacities. Through PCT measurements, we also showed that the allying does not alter the thermodynamics of the Mg to MgH_2 reaction. The X-ray diffraction analysis suggested that the Fe-Ti catalyst is in the form a nanocrysalline/X-ray amorphous alloy.

Chapter 2 and 3 present the sorption kinetics for two more ternary alloys, Mg-Fe-V and Mg-Cr-Ti. In both cases the sorption behavior of the ternary alloys was compared to that of their binary counterparts and an evident superiority was observed for the ternary systems. The binary alloys showed a gradual degradation in the reversible capacity over extended cycles. However, the ternary systems with the sufficient amount of allying

elements showed stable kinetics behavior up to 120 cycles at 200˚C. The distribution of the catalyst phase was also observed using the HAADF microscopy technique.

In Chapter 5, we performed detailed microstructural and kinetics analysis on the Mg-Cr-V system. The use of Cr-V catalyst allowed for absorption of this ternary system at room temperature and low pressure of 2 bar. We also performed cycling test at two temperatures of 200 and 300˚C. We were able to achieve fast desorption rate (<2 min to fully desorb) at 300˚C and 1 bar hydrogen pressure. Using conventional TEM analysis, we demonstrated that the bi-metallic catalyst maintains its fine distribution even after 200 cycles. This was further corroborated from the X-ray diffraction results where we calculated the grain size of MgH_2 via IBA method and at different stages of cycling for a ternary and a binary alloy with the same amount of catalyst loading. The hydride grain size showed a faster growth rate in the binary alloy compared to that for the ternary alloy.

The results from our cryo-stage TEM analysis on the partially absorbed ternary sample also revealed some new aspects of the hydrogenation mechanism of magnesium. Our results indicated that during absorption the formation and growth of the hydride phase does not take place in the way described by the contracting volume, aka contracting envelope or core shell, model. To our knowledge, this was the first direct TEM-based observation of the absorption mechanism.

We also performed a thorough kinetics analysis based on the known JMA model. The activation energy values were obtained at different levels of driving force. We observed that the activation energy is strongly depending on the applied driving force. This finding along with the Avrami exponent values suggested that by increasing the driving force, rate limiting step evolves. We posited that both nucleation and growth processes are contributing to the activation energy value at low driving force. However, at high driving force, the contribution of the nucleation diminishes as an instantaneous nucleation occurs.

Through combining our microstructural observation with the kinetics analysis we proposed a new mechanism for the hydrogenation of magnesium. In this mechanism, the nucleation of hydride occurs at the surface of the particle and most likely at the interface of catalyst particles and magnesium. Upon the formation of the hydride nuclei, which is rich in hydrogen, a hydrogen depleted area forms in the surrounding region. The growth of this nuclei is then controlled by the diffusion of the hydrogen atoms though the lattice of surrounding magnesium matrix.

7.2 Future work

A catalyst design methodology for the sorption kinetics of metal hydrides is an important step toward practical application of these materials. Although metal hydrides do not meet the temperature/pressure and gravimetric capacity criteria for mobile and on-board applications, there is an even increasing demand of metal hydride on stationary power back-up and portable energy storage applications. The fast charging rates and high capacities are important requirements for these applications with thermodynamic stability being less crucial of a prerequisite. High temperature stability of these materials plays a crucial role in concentrating solar power systems coupled with metals hydride-based thermal energy storage. A key solution is to use a potent catalyst with high stability at high temperature over prolonged cycling. In this thesis, we showed the significant influence of bi-metallic catalyst on the sorption kinetics of MgH_2 over single elemental additions. We applied various criteria in our bi-metallic alloy selection which are the following: strong efficiency toward hydrogen dissociation/recombination and diffusivity, positive enthalpy intermixing with Mg, and also negative heat of intermixing between the adding elements. The tested bi-metallic catalyzed materials based on these criteria showed enhanced kinetics and stability up to 250 cycles at high temperatures up to 300˚C. However, a quick comparison between the sorption behavior of different bi-metallic catalyst shows a distinct

variation in their sorption properties. For instance, Cr-V catalyzed systems showed the fastest kinetics amongst all tested systems. The reason behind such difference may lie in a variety of possible factors. Factors such as melting point of the two alloying elements, their enthalpy of sublimation, the difference between the atomic size of the adding elements and Mg and the two adding elements size difference, etc., could play important role in this respect. Moreover, the nature of most of these differences might lie in the electronic structure of the bi-metallic phase. Hence, a detailed study on the electronic structure of different bi-metallic systems on a broad composition range could shed more light on the distinctive behavior of these catalysts. This could be achieved by a systematic DFT study on the sorption activity of these materials.

Another important factor to design a proper catalyst is the enthalpy of solution of hydrogen atoms in the catalyst phase. This becomes even more important when using strong hydride forming or non-hydride forming elements. For instance, Ti has strong ability to dissociate hydrogen molecules at its surface; however it forms a stable hydride (TiH_2) which hinders further catalytic activity of this element. A similar scenario may occur for Ti-rich catalyst phases where the enthalpy of solution is higher than formation enthalpy of MgH_2. The work done in this thesis could also be expanded by investigation different combinations and concentrations of hydride forming and non-hydride forming elements to reach a conclusive knowledge of the proper use of these elements.

As mentioned above, the negative enthalpy of intermixing seems to be an essential criterion toward the high stability of these catalysts over extended cycling tests. The next logical step would be to investigate more bi-metallic systems in order to draw a decisive correlation between the stability of sorption behavior and the heat of intermixing.